AN INVESTIGATION OF THE ACCURACY OF EMPIRICAL AIRCRAFT DESIGN FOR THE DEVELOPMENT OF AN UNMANNED AERIAL VEHICLE INTENDED FOR LIQUID HYDROGEN FUEL

By

CHRISTOPHER SCOTT CHANEY

A dissertation submitted in partial fulfillment of
the requirements for the degree of

DOCTOR OF PHILOSOPHY

WASHINGTON STATE UNIVERSITY
School of Mechanical and Materials Engineering

DECEMBER 2014

ProQuest LLC.
789 East Eisenhower Parkway
P.O. Box 1346
Ann Arbor, MI 48106 - 1346

To the Faculty of Washington State University:

The members of the Committee appointed to examine the dissertation of CHRISTOPHER SCOTT CHANEY find it satisfactory and recommend that it be accepted.

_____

Konstantin I. Matveev, Ph.D.,Chair

_____

Jacob W. Leachman, Ph.D.

_____

Lloyd V. Smith, Ph.D.

ACKNOWLEDGMENT

The work to be presented herein is expressed under my name, but in reality is the culmination of the tireless (although not without continuously being tired) efforts of such a fantastic cast of characters that, in hindsight, it seemed more fun than a research project should allow. Certainly all the players deserve credit in this work and I am humbled by their effort and support, both for the project, each other, and me. It has been my utmost honor to work with you all.

My sincere thanks extend to Dr. Matveev, not only for his help and guidance, as is intrinsic with the role of the advisor, but for going beyond that role with his genuine interest in supporting me throughout my schooling and for his understanding and flexibility with both my direction and timeline. I also wish to acknowledge the efforts of Dr. Leachman in establishing both an exciting and pertinent project and for developing the team dynamic required to undertake it. With the rag-tag group that comprised Genii, direction must have been very similar to herding a group of manic-depressive cats. His efforts, however, prevailed and what the team has to show for it is one of our proudest achievements.

And to my coworkers and friends, Eric, Patrick(s), Eli, Justin, Alex, Nic, Ryan(s), Frida, Kurt, and all the others. Working alongside you was one of the defining experiences in my academic career and my life. Other groups may have done it better, but nobody could have done it with more character. My accomplishment here is in no small part yours and I owe the team a debt I can only hope to someday repay. Through the long nights, the crashes, the rebuilds, and the successes, you were there to lend both a physical and emotional hand. Thanks to all of you, I wish you happiness in all your endeavors and I hope to see you again at Minh's sometime soon.

AN INVESTIGATION OF THE ACCURACY OF EMPIRICAL AIRCRAFT DESIGN FOR THE DEVELOPMENT OF AN UNMANNED AERIAL VEHICLE INTENDED FOR LIQUID HYDROGEN FUEL

Abstract

by Christopher Scott Chaney, Ph.D.
Washington State University
December 2014

Chair: Konstantin I. Matveev

A study was conducted to assess the accuracy of empirical techniques used for the calculation of flight performance for unmanned aerial vehicles. This was achieved by quantifying the error between a mathematical model developed with these techniques and experimental test data taken using an unmanned aircraft. The vehicle utilized for this study was developed at Washington State University for the purpose of flying using power derived from hydrogen stored as a cryogenic liquid. The vehicle has a mass of 32.8 kg loaded and performed a total of 14 flights under battery power for 3.58 total flight hours. Over these flights, the design proved it is capable of sustaining level flight from the power available from a PEM fuel cell propulsion system.

The empirical techniques used by the model are explicitly outlined within. These yield several performance metrics that are compared to measurements taken during flight testing. Calculations of required thrust for steady flight over all airspeeds and rates of climb modeled are found to have a mean percent error of 3.2%±7.0% and a mean absolute percent error of 34.6%±5.1%. Comparison of the calculated and measured takeoff distance are made and the calculated thrust required to perform a level turn at a given rate is compared to flight test data. A section of a test flight is analyzed, over which the vehicle proves it can sustain level flight under 875 watts of electrical power.

The aircraft's design is presented including the wing and tail, propulsion system, and build technique. The software and equipment used for the collection and analysis of flight data are given. Documentation and validation is provided of a unique test rig for the characterization of propeller performance using a car. The aircraft remains operational to assist with research of alternative energy propulsion systems and novel fuel storage techniques.

The results from the comparison of the mathematical model and flight test data can be utilized to assist in the development of similar Unmanned Aerial Vehicles, express the uncertainty in calculated vehicle performance numbers, and assist in identifying error in control system design.

TABLE OF CONTENTS

LIST OF TABLES

LIST OF FIGURES

To My Family

…

Whose Love And Support Meant The World To Me

…

Even When It Was A Bit Overbearing

CHAPTER 1

1.1 Introduction

As of 2014 an exciting variety of unmanned aircraft are beginning to make significant appearances outside of the military market in both academic and commercial fields. The development of these vehicles, optimization of their design, and research into improved control systems is a major focus in applied aerodynamics and control. Despite blooming interest in this field, the accuracy of the primary methods used in the calculation of the performance of these vehicles remains uncertain. The work herein addresses this lack of knowledge in the academic community by quantifying the error between performance calculations and experimental testing through the case study of a particular vehicle. The presentation of the design of a unique vehicle, build, performance calculation, flight testing, and assessment of the performance calculations from those tests will greatly assist the recent efforts in these fields.

1.2 Background

The Unmanned Aerial Vehicle (UAV), sometimes called Unmanned Aerial System (UAS) when the term includes ancillary components, is evolving away from its military origins into commercial and research platforms with great potential. UAV's designed to perform or assist with academic research are beginning to emerge from universities across the world as hardware costs continue to drop and provisions to fly UAV's for research are made by governments and regulating agencies. These vehicles offer a low-cost way of bringing technology out of the lab and into a real-world flight environment without endangering a pilot.

To date, university teams have utilized UAV's to assist with an impressive range of topics including control algorithm development (Lundström 2012), crop monitoring (Hunt et al. 2008), atmospheric sensing (Cook et al. 2013), similitude to full-scale aircraft (Jordan et al. 2006) and investigation of alternative power and propulsion systems (Bradley et al. 2007). These vehicles range in mass from less than a kilogram to above 25 kilograms with the practical upper limit set by cost and complexity. In many cases the UAV is not the focus of the research, but rather a demonstrator, testbed, or sensor platform through which the subject of the research is explored. A representative cross section of the power and wing loading of several UAV's and five general aviation aircraft is shown in Fig. 1.1. Operational aircraft trend toward higher power loadings due to the need to operate in adverse conditions. Wing loading also trends higher with increasing size, in part due to larger flight envelopes and also scale effects.

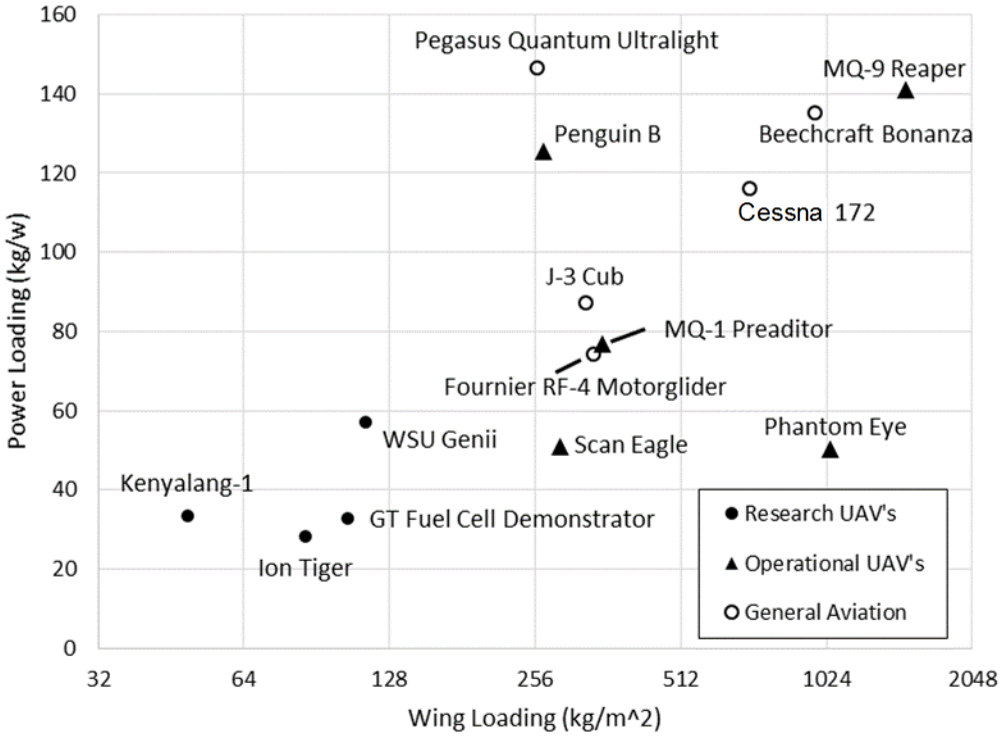

Figure 0.1: *Power loading and wing loading of several UAV's and general aviation aircraft.*

Theoretically, if access to a wind tunnel was free or if rapid prototypes could be produced, a researcher could develop an aircraft or its control system using experimental techniques alone. In reality, monetary and time limitations restrict the amount of testing that can be performed. As such, much of the design of the vehicle must be performed mathematically to reduce, or eliminate, the number of trials that must be ran. In the absence of test data, the performance of the vehicle must be calculated with sufficient accuracy to assure a design meets its requirements and to compare designs in a quantifiable way. In general, calculation methods tend toward two extremes: empirical or numerical.

For empirical techniques, past observation in the form of generic test data of comparable configurations, correlations, and principle mechanics equations are used to predict the behavior of individual aircraft components. The behavior of the whole is then approximated by the behavior of the parts, sometimes with additional formulations for interference effects. Empirical techniques are not ideal because interference effects can be large and extrapolation of test data may not follow the anticipated governing equation. Numerical approaches solve the flow pattern around the aircraft and predict aircraft behavior from the resulting forces. Numerical techniques must resign to an approximation of the flow due to imperfect mathematical models and constraints on computational resources.

These methods do not have to be used separately, and a hybrid of both techniques and experimental tests is usually applied in practice. This creates a challenge for designers who must decide not only to what extent they should rely on numerical simulation, but also to what accuracy their predictions need to be. Complete computational fluid dynamics (CFD) optimization is often prohibitive in an accelerated design environment, while the accuracy of empirical techniques for

UAV scale vehicles is not well quantified in the literature. It is therefore uncertain to what extent the design of the aircraft can be simplified while retaining acceptably accurate performance calculations and assuring the vehicle will meet specification.

Empirical design methods are well documented in books such as Torenbeek (1976), Strojnik (1983), Raymer (2006), Gundlach (2012), and Anderson (2001). These design books are geared toward practical aircraft development and the methods are mostly generic and not proprietary to the author. While useful for the design of the vehicle, these books face the fundamental problem that the methods outlined inside are not compared against actual aircraft performance and the error associated with their use is not known.

Fundamental wind tunnel tests and derivation of theoretical governing equations for aircraft aerodynamics are outlined well in Abbott and Doenhoff (1959) and Hoerner's Fluid Dynamic Drag (1965) and Fluid Dynamic Lift (1992). These works are valuable to the designer and do, in many cases, substantiate their derivations with wind tunnel testing. The problem remains, however, that these formulations are for aircraft components and validations of the flight performance of the aircraft as a whole usually remain unpublished.

More recently, flight testing of research UAV's has touched on the subject of performance validation. Bradley et al. (2007) present altitude and airspeed data over their test of a fuel cell powered research UAV. Unfortunately, documentation of additional parameters of interest such as rate of climb, takeoff distance, and glide ratio are not given. Additionally, a comparison between calculated and actual flight performance is not made. Lundström and Krus (2012) present good documentation of micro UAV flight test results for lift to drag ratio (from which many performance metrics could be extracted), however their procedure focused on testing rather than

calculation of performance. In summary, the lack of flight test data compared to empirical performance calculations leaves the designer without a good idea of the viability of their computations.

1.3 Research Objective

The primary objective of this research is to quantify the accuracy of empirical performance calculations by means of computing the error between a mathematical model and experimental flight test data for various flight regimes. This is achieved through the presentation of a development cycle of a research UAV similar to other low-power and low-speed research UAV's on the order of 30 kg. The mathematical model is developed from empirical methods for specific components taken from various sources such as Raymer (2006), Abbott and Doenhoff (1959) and Horner (1965). It is used to compute the vehicle's drag which is required to derive various performance metrics such as flight power, rate of climb, turn rate, and takeoff distance. Both these metrics and the vehicle's drag itself (as determined by its thrust) can be compared to flight test results to determine the model's error.

The accuracy of the mathematical model used herein is therefore applicable to the specific empirical methods used for each component analyses. Because most empirical techniques are similar, the accuracy does qualitatively speak to the accuracy of empirical techniques as a whole. This could be considered a good first step toward the larger assessment of the primary empirical design techniques presented by various authors.

A fundamental result of this research is that the calculated performance of a low-speed research UAV can be presented with a quantification of its accuracy, or at the very least, of the accuracy of a similar mathematical model. This work, however, has far boarder effects. The knowledge of

the error associated with the mathematical model used herein can assist in the development of similar vehicles. If the error within a performance calculation is known, the designer can leave less extra margin in the design to accommodate uncertainty in the calculation methods. This can help save weight and cost, for example if a smaller motor or propeller can be utilized. This is especially true for research into optimization of design techniques. It is impossible to reach a true optimized solution if extra performance margin is required to account for uncertainty in the computation methods. Additionally, if empirical methods are being utilized to compute the forces acting on a vehicle for the purposes of developing a control system, uncertainty in the methods must be known to assess the performance of the control system. Otherwise error in the control system, for example due to the linearization of the dynamics equations, is indistinguishable from the error resulting from the mathematical model.

The research UAV used as a case study was developed by the author and a group of students at Washington State University (WSU) and is called Genii, as an abbreviation of *Pondus Hydrogenii*,. This aircraft is designed with the specific goal to allow flight testing of alternative energy fuel systems, particularly, liquid hydrogen propulsion. Experimental fuel systems are typically of low power density because they have not yet been optimized for weight savings. As such, a novel vehicle capable of accepting low-power density propulsion was required. Genii has a power loading of 62 watts per kilogram, however the design methods are also applicable to more conventional configurations. The methods examined apply to vehicles operating down to Reynolds numbers of 60,000 based on the wing chord, below which viscous effects become much more pronounced.

A description of the vehicle's requirements, design, geometry, and construction techniques are detailed in the following chapters. The simplified methods used for the purpose of vehicle preliminary design are expressed, in contrast to the higher-fidelity mathematical model used for the calculation of vehicle performance. Aircraft design is inherently multidisciplinary, however the investigation herein will focus on analyzing the empirical methods and mathematical model used in the computation of vehicle performance. Structural optimization, system integration, and hydrogen storage in Genii will be discussed only as they pertain to the aerodynamics and propulsion of the vehicle.

1.4 Additional Contributions

As a consequence of the work performed toward the primary research objective, several other additional contributions arise. These contributions may be lacking in impact or novelty to constitute a primary program of study but do offer insight to several areas of applied aerodynamics pertaining to research UAVs.

1.4.1 Outline of design process

A detailed report of the design methods used for the development of the Genii aircraft will help facilitate similar development projects. To assist these projects, an explanation of the selection and optimization of major components including wing, empennage, fuselage, landing gear, and motor-propeller combination is given. Most methods are taken from various sources and citied. In a few cases, design decisions were based off the author's observation of prior aircraft.

1.4.2 Description of a mathematical model for performance prediction

In addition to the design outline, the mathematical model developed to predict the performance of the Genii aircraft could be used directly or modified to suit future development efforts. The model is comprised of formulations documented in design literature and test reports. The model therefore differs slightly from any particular method laid out in design literature. The techniques utilized in the analysis of particular components, for example the profile drag of the wing or the drag of the fuselage, are selected from individual sources based on their applicability to the current project. The designer might find the approach herein more useful for the development of low-speed research UAVs than other methods.

1.4.3 Development of a low-cost propeller test stand as a wind tunnel alternative.

A car-top test module is used to populate data for a model aircraft propeller not yet characterized in literature. Most research UAVs on the scale of the Genii aircraft will use propellers designed for large model aircraft. For these propellers, sufficient information on blade geometry is not given by the manufacturer to compute performance numerically. Physical testing of the propeller under flight conditions is the easiest method for obtaining reliable propeller performance estimations. Test results for propellers roughly 25 inches in diameter at powers up to 2000 watts have not been documented in the literature. The car top test module developed as an alternative to a wind tunnel was cheap to build (<$100) and gave results accurate enough for use in the aircraft's design and motor selection process. The construction of the test module is documented so that future groups may use a similar method to acquire propeller or model data when access to a wind tunnel is not feasible.

1.4.4 Development of a novel UAV suitable for future research on alternative energy fuels.

Although the focus of this research is on extracting flight data from the Genii UAV, the aircraft itself can contribute to many research projects. The Genii UAV could be reconfigured or easily duplicated (no part of the design is proprietary) to assist with academic research projects. The large internal payload, manageable size, and low wing loading make the Genii aircraft unlike any commercial UAV currently on the market. The Genii UAV is a good candidate for a structure optimization study, as the current project focused chiefly on aerodynamic optimization.

1.5 UAVs for hydrogen and alternative energy power plants.

As discussed above, the primary contributions of this work involve the investigation of the mathematical model. However, an introduction to hydrogen-powered flight is provided to explain the motivation behind the development of the UAV assessed herein.

Genii was developed as a joint research and student project at Washington State University. It is pictured shortly before a landing in Fig. 1.2. The Genii aircraft has a wingspan of 5.5 m, a wing area of 3 m^2, and has a nominal empty weight of 22 kg. The maximum takeoff weight of the aircraft is 35 kg. The development project was initiated in May 2012 and the aircraft flew for the first time under battery power on May 18th 2013.

Figure 0.2: *The Genii aircraft developed at Washington State University*

The project aimed to develop a UAV small enough to operate from model aircraft airfields and safely test alternative-energy power systems with a focus on liquid hydrogen fuel. No production vehicle of this size had sufficient low-power performance nor a large enough interior volume to accommodate the size of equipment desired for this undertaking.

The Genii project was started due to recent interest in developing alternative power plants for aircraft purposes. In 2003, Airbus initiated a Cryoplane design study to identify the feasibility of hydrogen fueled commercial aircraft (Westernberger 2003). Recently, hydrogen fueled aircraft have become viable for applications where long endurance flight is desired. Preliminary studies indicate that a properly designed aircraft could theoretically achieve 10 days of endurance using liquid hydrogen fuel (Millis et al. 2009).

The primary advantage of hydrogen fuel in aerospace applications is a high specific energy, 120 kJ/g compared to Jet-A aviation fuel at 42.8 kJ/g (Brewer 1991) and conventional gasoline at 47.5 kJ/g (Collage of the Desert, "Hydrogen Properties, Module 1" 2001). This presents a unique opportunity for designers of long endurance aircraft where the weight of conventional fuel can consume 80% of the aircraft's takeoff weight. The energy density of hydrogen in gaseous form at

200 Bar gauge is 1,825 MJ/m^3 while in liquid form its energy density is 8,491 MJ/m^3 (Collage of the Desert, "Hydrogen Properties, Module 1" 2001). This is in relation to 31,150 MJ/m^3 for conventional gasoline. Liquid hydrogen is stored at approximately 23K which presents unique technical and safety challenges.

Despite the challenges, several companies and institutions have begun investigating the technological viability of liquid hydrogen fueled aircraft and unmanned aerial vehicles (UAV). Bradley et al. (2007) presented the work of a team at Georgia Tech that had developed a UAS powered by a 500 watt fuel cell supplied with gaseous hydrogen. The design and testing of the aircraft were discussed, and the vehicle's performance over a 160-second flight circuit was presented. Ward and Jenal (2010) developed a UAS powered by a Horizon 500 watt fuel cell and compressed hydrogen. The plane was demonstrated for a short hop of 50 seconds over which throttle settings were varied and the altitude response was recorded. Fürrutter and Meyer (2009) tested a 100 watt compressed hydrogen supplied fuel cell in a stock RC airplane. Kim et al. (2011) presented their work using sodium borohydride as a hydrogen source to fuel a 100 watt PEM fuel cell. Part of their work focused on flight testing under autonomous control, and flight times of two hours are demonstrated. Additionally, the liquid hydrogen fueled UASs Phantom Eye, by Boeing, Global Observer, by Aerovironment, and Ion Tiger, by the US Navy, have made great technological breakthroughs (Lyons et. al.), but the design and testing results of these aircraft remain mostly proprietary. Examples of five recent hydrogen fueled aircraft are depicted in Fig 1.3. The Genii aircraft is versatile and not constrained to operation with hydrogen fuel. Power plants such as generator-battery hybrids, solid oxide fuel cells, and internal combustion of nonstandard fuels such as propane are all viable for testing should the demand arise.

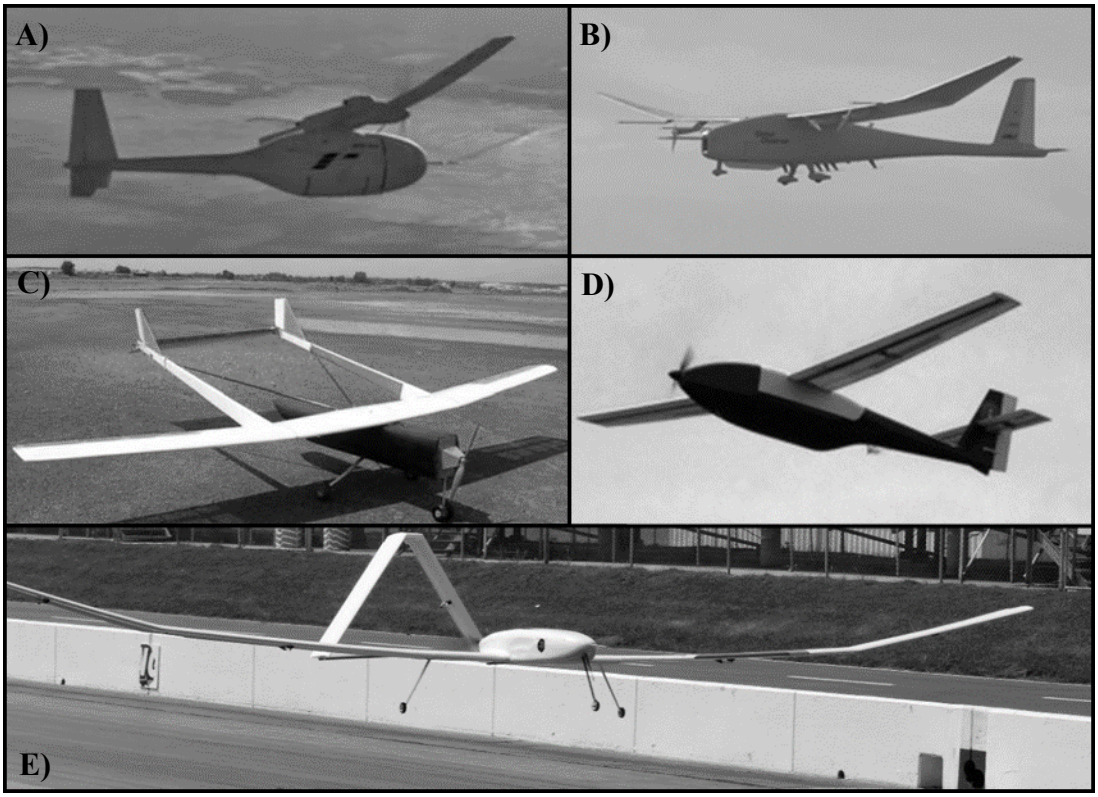

Figure 0.3: *Recent hydrogen fueled aircraft. A: Boeing's Phantom Eye (Jackson 2012), liquid hydrogen and IC engines. B: Aeroviornment's Global Observer (Boyer), liquid hydrogen and IC generator. C: Universiti Teknologi MARA's Kenyalang-1 (Ward and Jenal 2010), compressed gaseous hydrogen and fuel cell. D: Navy's Ion Tiger (NRL Public Affairs Office. "NRL Shatters Endurance Record for Small Electric UAV" 2013), liquid hydrogen and fuel cell. E: Georgia Tech's fuel cell research demonstrator, compressed gaseous hydrogen and fuel cell (Lance).*

CHAPTER 2

2.1 Aircraft Design Overview

The design, build, and instrumentation of the Genii aircraft are described in this chapter. This will include a summary of the aircraft and a description of the preliminary design of most components including wing, propulsion, tail, fuselage, and gear. For the Genii aircraft, only rudimentary structural design was performed. Structural design and capabilities will not be discussed in detail due to the aerodynamic focus of this report. The techniques expressed in this section are simplified for quick use in the preliminary design phase, and accurate computation of vehicle performance is outlined in Chapter 3. A brief description of the construction methods utilized with Genii is given as well as an overview of the instrumentation of the aircraft and data logging techniques.

2.2 Mission

The preliminary design of the Genii aircraft was performed with the intent of satisfying several mission requirements. For the case of the Genii program, it was more effective to develop a new aircraft than to purchase and modify an existing airframe to meet these requirements. The intent of Genii is to act as a demonstrational aircraft, to experiment with and showcase liquid hydrogen propulsion. As such, the aircraft's objectives are few, but hard to meet. Qualitatively, the primary objectives for the aircraft are defined as follows:

1. Capable of sustained level flight of several hours with power derived solely from liquid hydrogen fuel.
2. Forgiving flight characteristics.
3. Easy and safe to take off and land.

4. Robust.

Additional desirables are:

5. Sufficient payload capacity to assist with other university research, such as atmospheric sampling and alternative fuel technologies.
6. Easy to transport in the bed of a standard pickup truck and quickly assembled for flight.

These requirements translate to the following quantitative design parameters pertinent to the aerodynamic design of the vehicle:

1. Max level flight speed (V_{max}) greater than 20 $^{m}/_{s}$ for operation in light winds.
2. Stall speed no greater than 12 $^{m}/_{s}$ empty for ease of takeoff and landing.
3. Takeoff distance less than 100 m to allow for a fixed point-of-view takeoff by a pilot on the ground.
4. A max rate of climb faster than 1 $^{m}/_{s}$ to clear obstacles after takeoff.
5. Naturally stable in all modes except spiral with no need for artificial stabilization by flight computer.
6. At a minimum, capable of level flight from less than 875 watts electrical power. Other flight regimes such as climb may be supplemented with reserve battery power.
7. Accept a 10.2 kg propulsion system simulating the fuel cell and tank.

The endurance of the aircraft is not a rigid requirement but is desired to be over roughly 4 hours. It is unlikely the vehicle will be flown this long due to the cost and safety measures associated with procuring and handling sufficient liquid hydrogen as well as crew fatigue.

2.3 Aircraft Geometry

Genii is a high-wing monoplane of standard tractor motor configuration and tricycle landing gear. The aircraft is reconfigurable between a purely battery driven propulsion system, with loaded mass of 22.6 Kg, and a liquid hydrogen-battery hybrid system with a loaded mass of 32.8 kg. The wing area including the area superimposed over the fuselage is 3 m^2. The wing's aspect ratio is 10.3 with a taper ratio of 0.56, washout of 3°, and dihedral of 4°. The wing is not swept. No wingtip devices are applied. The wing is a full-span SD7037 airfoil, a design developed by Dr. Selig for use with model sailplanes and documented in (Selig, Donovan, and Fraser 1989). The wing is designed to be disassembled into three pieces, two outer sections 1.75 m in length and an inner section permanent to the fuselage 2.00 m in length for a total wingspan of 5.50 m. Ailerons span 63% of the wing with a relative chord of 15%.

The aircraft incorporates a conventional tail mounted on a boom extending from the fuselage. The tail is removable from the fuselage for transport. Both vertical and horizontal stabilizers are swept to create a straight trailing edge. The vertical stabilizer has an area of 0.195 m^2 with a span of 0.65 m, aspect ratio of 2.17, and taper ratio of 0.5. The aerodynamic center (AC) of the vertical is located 1.84 m aft of the center of gravity (CG) for a vertical tail volume coefficient of 0.022. The rudder spans 84% of the vertical with a chord of 14.8 cm.

The horizontal stabilizer has an area of 0.527 m^2, a span of 1.7 m, aspect ratio of 5.48, and a taper ratio of 0.47. The AC of the horizontal stabilizer is located 1.99 m aft of the CG for a horizontal tail volume of 0.624. The elevator spans 88% of the horizontal with a chord of 14 cm. Figure (2.1) shows the geometric configuration of the aircraft. Detailed geometry is provided in Table (2.1).

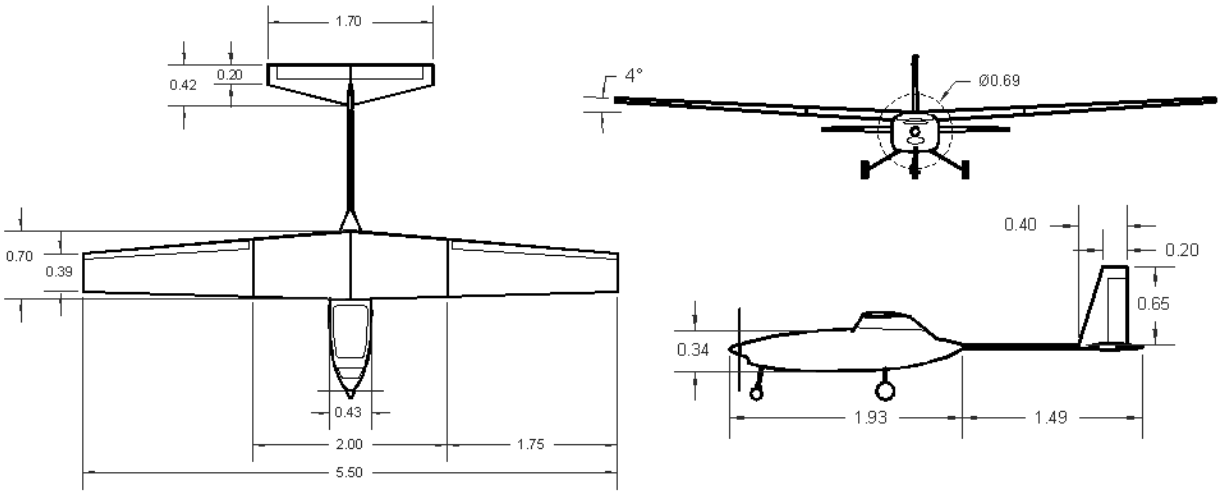

Figure 0.1: *Planforms of the Genii aircraft.*

Table 0.1: *Geometric definition of the wing and tail of the Genii aircraft.*

Wing		Horizontal Stabilizer	
SD 7037	Airfoil (root and tip)	1.99 m	Separation (from wing 1/4 chord)
3 m^2	Area	0.624	Volume Coefficient
5.5 m	Span	NACA 0012	Airfoil (root and tip)
0.56 m	Mean Aerodynamic Chord	0.527 m^2	Area
0.70 m	Root Chord	1.7 m	Span
0.39 m	Tip Chord	0.32 m	Mean Aerodynamic Chord
10.3	Aspect Ratio	0.42 m	Root Chord
0.56	Taper Ratio	0.20 m	Tip Chord
4º	Incidence	5.48	Aspect Ratio
0º	1/4 Chord Sweep Angle	0.47	Taper Ratio
4º	Dihedral	0º	Incidence
-3º	Twist	11º	1/4 Chord Sweep Angle
3 m	Aileron Span (combined)	1.50 m	Elevator Span
15%	Aileron % Chord	0.14 m	Elevator Chord

Vertical Tail		Vertical Tail Cont.	
1.84 m	Separation (from wing 1/4 chord)	0.20 m	Tip Chord
0.022	Volume Coefficient	2.17	Aspect Ratio
NACA 0012	Airfoil (root and tip)	0.50	Taper Ratio
0.195 m^2	Area	0º	Incidence
0.65 m	Span	12.68º	1/4 Chord Sweep Angle
0.31 m	Mean Aerodynamic Chord	0.65 m	Rudder Span
0.40 m	Root Chord	0.15 m	Rudder Chord

2.4 Fuel Cell Selection

The selection of fuel cell drives the design of the Genii aircraft as it sets the available power and provides an estimate of the propulsion system weight. An air breathing proton exchange membrane (PEM) fuel cell with self-humidification and automated fuel flow and power control is used for the Genii aircraft. This eliminated the need for a custom controller, humidifier, and compressor. The expedited timeframe of the project limited selection to fuel cell suppliers with off-the shelf units with little or no lead time. Of the suppliers, only Horizon Fuel Cells met all requirements. Several recently developed experimental UAS are powered with Horizon fuel cells (Ward and Jenal 2010, Fürrutter and Meyer 2009). The fuel cell model was selected based on the highest specific power. The specific power of the units considered is shown in Fig. (2.2). Specific power is defined here for just the cell and controller, and does not include fuel, tank, and line weights.

A Horizon 1000 (H-1000) unit and controller are utilized with a specific power of 227 watts/kg. The Horizon aeropack unit, with 1.87 times the specific power of the H-1000 is not within budgetary constraints for this project but could prove beneficial for the next generation of aircraft. Also included for reference in Fig. (2.2) is the BCS 500 pack utilized be the Georgia Tech Fuel cell UAS (Bradley 2007). The performance gain for this scale PEM fuel cell over the past six years is evident.

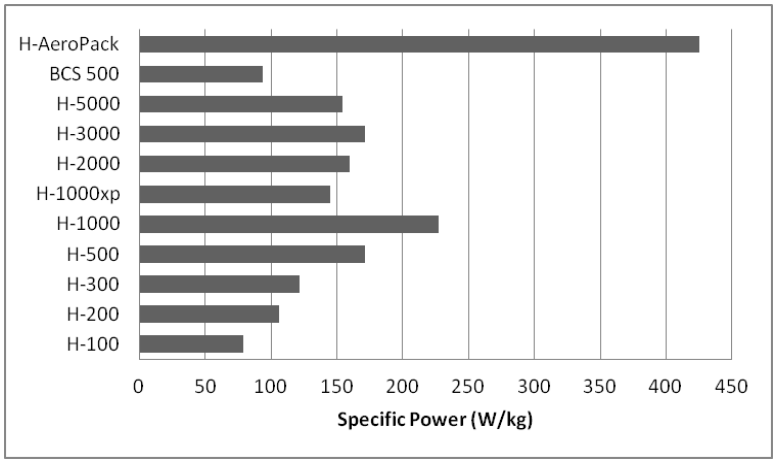

Figure 0.2: *Specific power of available fuel cells.*

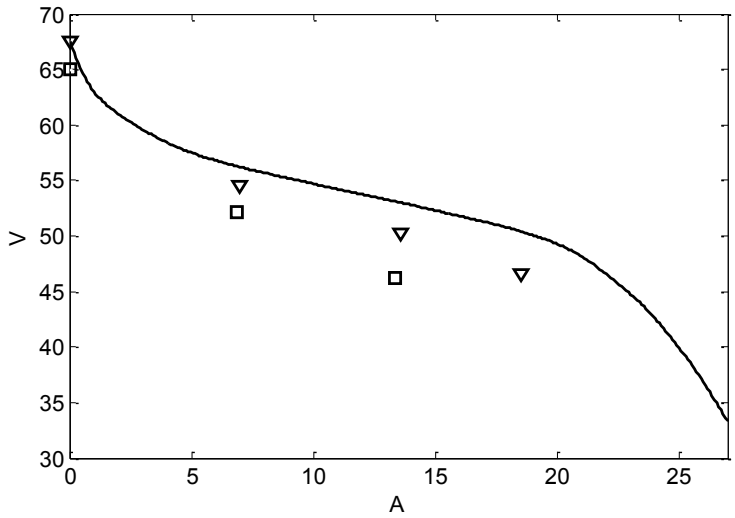

Figure 0.3: *Fuel cell polarization curve. Solid line: characteristic manufacture's curve. Triangles and Squares: preliminary fuel cell test trials.*

The H-1000 is comprised of 72 cells and characterized by a polarization curve that varies from 68 V at no load to 44 V at 23 A (Fig. 2.3). The high voltage present at less than 20 amps (A) current draw creates a problem, as the majority of remote controlled (RC) speed controller equipment is not rated above 50 volts. The fuel cell controller is responsible for preventing low voltage (< 26 V), over current (> 30 A) and over temperature (> 65°C) conditions via shutdown. The fuel cell controller adjusts the speed of four fans on the cathode to maintain the stack temperature less than 65°C. At laboratory conditions of 23°C and 16% relative humidity, exhaust is typically at 45°C and 13% relative humidity.

After parasitic power draw of ancillary systems, 875 Watts electrical power is available for propulsion. The initial aircraft was designed to perform all operations including takeoff and climb at less than this power. Creep in the aircraft's final weight necessitated the final aircraft use a battery reserve for high-power flight regimes, however the ability to cruise in level flight under 875 Watts was maintained.

2.5 Propulsion

Propulsive power for the Genii aircraft is supplied via a single brushless electric motor, however the exact motor definition has changed over the course of design and flight testing. Brushless

electric motors are now the standard for electric RC models. For simplicity, only over-the-counter motors and Electronic Speed Controllers (ESC) are used.

The brushless motors utilized are all three phase alternating current (AC) motors. The AC current is regulated by the ESC by commuting the direct current (DC) available from the batteries or fuel cell. A trapezoidal commutation scheme is employed by all ESC's utilized by the Genii aircraft. The DC supply from the batteries is switched by the ESC using a bank of metal–oxide–semiconductor field-effect transistors (MOSFETs) such that two of the three phases are energized while the back emf of the remaining phase is sampled by the ESC to determine the rotational phase of the motor. Knowledge of the motor's rotational phase is critical so that the ESC can switch electrical phases at the proper interval to maintain the phasor of the electromagnets a prescribed angle ahead of the phasor of the permanent magnets. This angle is referred to as ESC timing.

Of primary interest to the mechanical designer is that the motor's rotational speed is not controlled by the ESC timing but rather by the voltage applied to each phase of the motor. For high-revolution per minute (rpm) operation, high torque is required and the MOSFETs on the ESC are switched at full or close to full duty cycle. For reduced rpm operation, the MOSFETs are pulsed to produce a pulse width modulated (PWM) signal to each phase. The average of this PWM signal is a lower, time averaged, voltage than that of the battery supply. At reduced voltage, the electromagnetic field strength is reduced and the corresponding motor torque is lower than at full duty cycle. The efficiency of MOSFETs is quite high, approximately 93%, when saturated, however in transient operation such as the switching that occurs at each PWM pulse, the MOSFETs' efficiency can be drastically lower. This has one critical repercussion: operation at a power, rpm, or torque, less than that experienced at full duty cycle can be much less efficient. As such, a properly paired

propeller, motor and ESC should approximately develop the rated capacity (or less) of the motor or ESC at full throttle. If operating at rated capacity but reduced throttle, the reduced duty cycle will cause excessive inefficiency, heating, and potential damage to the MOSFETs. Ignorance of this phenomenon resulted in an inappropriate selection of motor and propeller for the initial Genii design and was the predominate factor in an early crash resulting from damage to an ESC.

Three propulsion strategies were analyzed for the Genii aircraft 1) constant rpm fixed pitch 2) nonconstant rpm fixed pitch, 3) constant rpm variable pitch. Methods two and three would operate at constant power, varying either the rpm of the motor or the pitch of the propeller to maintain constant propulsive power. Figure (2.4) depicts the calculated thrust performance of an Advanced Precision Composites (APC) 26X15E (Advanced Precision Composites Propeller Data List) propeller when run at a constant 3027 rpm (method 1, dashed line) and when the propeller speed is varied from 3027 rpm static to maintain constant 1000 watts shaft power, (method 2, solid line). Variable pitch (method 3) is not shown but would qualitatively have a similar trend as the constant power curve. Figure (2.4) is developed from data provided by the manufacturer from the 3D potential flow NASA TAIR program. Propeller testing discussed in Chapter 4 found that the manufacturer overestimated the degradation in thrust with airspeed, as the tested propeller

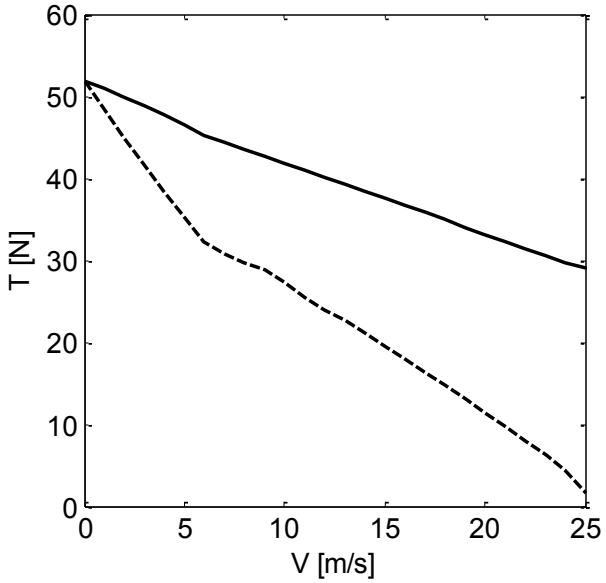

Figure 0.4: *Thrust degradation with airspeed for an APC 26X15 propeller. Dashed line: constant 3027 rpm. Solid line: constant 1000 watts shaft power.*

outperformed the predictions. Additionally, Fig. (2.4) is for demonstration purposes; in its final configuration, Genii operated at much higher rpm and thrust than shown in the figure.

It is evident that substantial gains in maximum thrust are achievable with methods 2 or 3, however method one was chosen for operation of the Genii aircraft. Method 2 was strongly considered, however it violates the maximum-power-maximum-rpm rule described above. I.E. the motor must operate at reduced throttle for all airspeeds under the maximum airspeed or excessive power would be required.

Method 3 was discounted because no commercially available variable pitch propellers in the desired power range exist on the market. Heinzen (2011) gives a description of the development of a passively actuated variable pitch propeller for UAV's, however due to time constraints, such a product was not developed and installed on Genii. While the performance loss is unfortunate, the primary mission of the Genii aircraft is not speed, and therefore the thrust difference between the schemes is not critically prohibitive. While the deficit at high speed is large and a large hit in maximum airspeed is taken, the deficit is less pronounced at low airspeed such as during climb. Additionally, a critical design case, operation at low power for cruise, is nearly identical for both schemes so long as the rpm required is less than the rpm used for full power operation in method 1.

For the design of Genii, the propeller with the most desirable performance was selected first and the motor selected to fit the requirements of the propeller. Critical cases were examined when selecting a propeller, the static thrust and the thrust when operating at 800 watts at an airspeed of 15m/s. The static thrust is a critical parameter in takeoff distance. The thrust at 800 watts 15m/s is the most important consideration as this was predicted to be the power and airspeed for cruise,

although the true values have since changed. The thrust performance of the propellers considered for Genii as predicted by the manufacturer are shown below in Fig. (2.5).

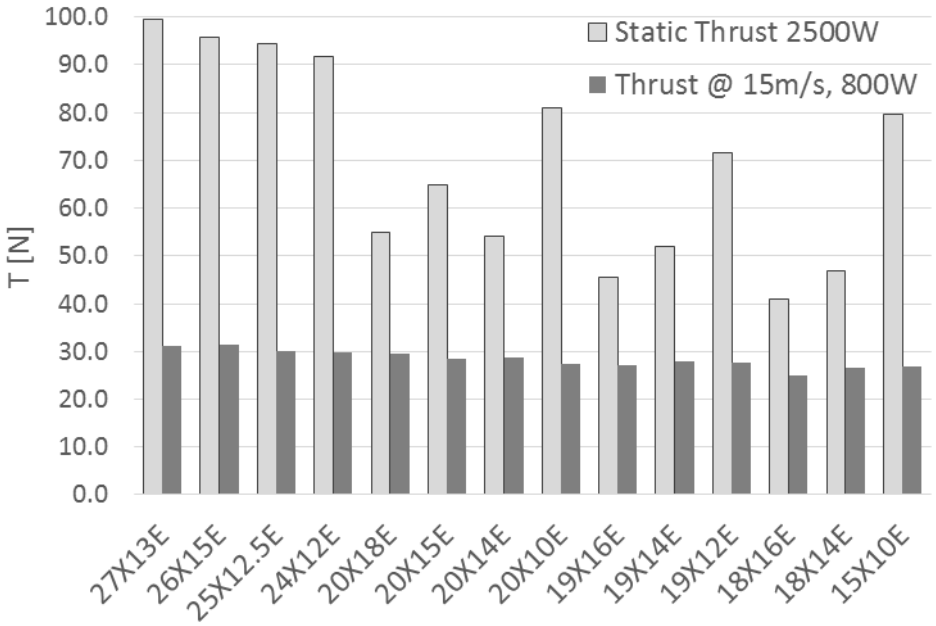

Figure 0.5: *Comparison of thrust performance of the APC line of propellers. Data taken from manufacturer (Advanced Precision Composites Propeller Data List).*

Developing actual test data for the whole range of propellers was outside the timeframe of the project. Detailed propeller testing is depicted in Chapter 4 for the 26X15E in conjunction with a spinner, as utilized in flight testing. The first number in the propeller nomenclature indicates the diameter in inches, the second number indicates the nominal inches of advance per revolution of the propeller, and the "E" indicates the propeller's structure was designed for electric motor operation (as internal combustion engines induce large torque impulses to the propeller with every ignition cycle).

Propeller static thrust trends higher with increasing diameter. The 27X13E is the largest available from the manufacturer. Propellers with high ratios of diameter to pitch are more efficient at low airspeed while propellers with low ratios of diameter to pitch are more efficient at high airspeed

and produce thrust over a greater range of airspeeds for a given rpm. The data in Fig. (2.5) was used to narrow down the propeller options, however the final propeller selection was performed after examining the propeller's performance over the entire operating envelope of the aircraft as seen in Chapter 3. The APC 26X15E propeller was used for the final Genii configuration due to its efficiency at high speed compared to the other propeller options. The crossover airspeed where the 26X15E produces more thrust than the 27X13E occurs below the stall speed of Genii, so for all regimes except takeoff, the 26X15E is superior.

The motor for the Genii aircraft was selected to produce the required torque to drive the propeller at the desired rpm. The propeller sets the relationship between torque and rpm, and therefore shaft power as well. For a given power input the propeller determines the torque and rpm required. It is therefore only necessary to choose a motor such that the required rpm is obtained at full throttle while remaining below the rated power of the motor.

2.6 Wing Design

The wing design of the Genii aircraft was performed by selecting in order: an airfoil, wing area, aspect ratio, taper ratio, twist, and dihedral. These parameters were selected using the methods outlined in this subsection. The methods used do not constitute a detailed optimization due to the vehicle's expedited development cycle.

The airfoil SD7037 is selected for the entire wing due to established performance for remote control gliders and sailplanes (Selig and Gopalarathnam 1997). The SD7037 airfoil exhibits good low Reynolds number performance, is well documented in the RC community, and reliable wind tunnel data is available from Selig et al (1995). These wind tunnel tests indicate the airfoil profile has a maximum lift coefficient, c_{lmax}, of 1.2 and a minimum drag coefficient, c_{dmin}, of 0.09 at Re

= 300,000. Polars for the SD7037 are shown in later in Fig. (3.3). The minimum Re for the final Genii configuration is 325,000 resulting at the wingtip prior to stall. The airfoil was selected very early in the design process when the anticipated flight speed of Genii was quite slow. A thicker airfoil with less stall severity and optimized for higher Re operation would have been a better selection for the final configuration had the geometry not been frozen. The wing is geometrically twisted but the airfoil remains the same along the span for both design and build simplicity.

The wing area of the Genii aircraft was selected as an optimization of stall speed (V_{stall}), $V_{max,}$ takeoff distance, and maximum rate of climb (M_{roc}). These four metrics require a selection of wing loading (W_l) and thrust to weight ratio (T_w), defined as follows respectively

$$W_l = \frac{W}{S} \tag{2.1}$$

$$T_w = \frac{T}{W} \tag{2.2}$$

where W is the aircraft's weight, S the wing area, and T the static thrust, defined as the thrust of the propeller when not advancing (in zero mean flow). This occurs when the aircraft is stationary and is most commonly how T_w is reported because thrust measurements during flight are outside the ability of most hobbyists to measure. Additionally, using static thrust results in a single T_w rating for an aircraft.

When plotted in W_l vs T_w space, requirements 1 through 4 above form a set of boundaries outside of which the aircraft will not meet the requirement. A plot of this technique for selecting wing area for the Genii aircraft is shown in Fig. (2.6). Vertical solid lines represent constant stall speeds. Finely dashed lines radiating linearly from the lower left to upper right represent constant takeoff

distances. Solid lines decreasing from left to right are lines of constant maximum airspeed, and dashed lines running left to right are lines of constant maximum rate of climb.

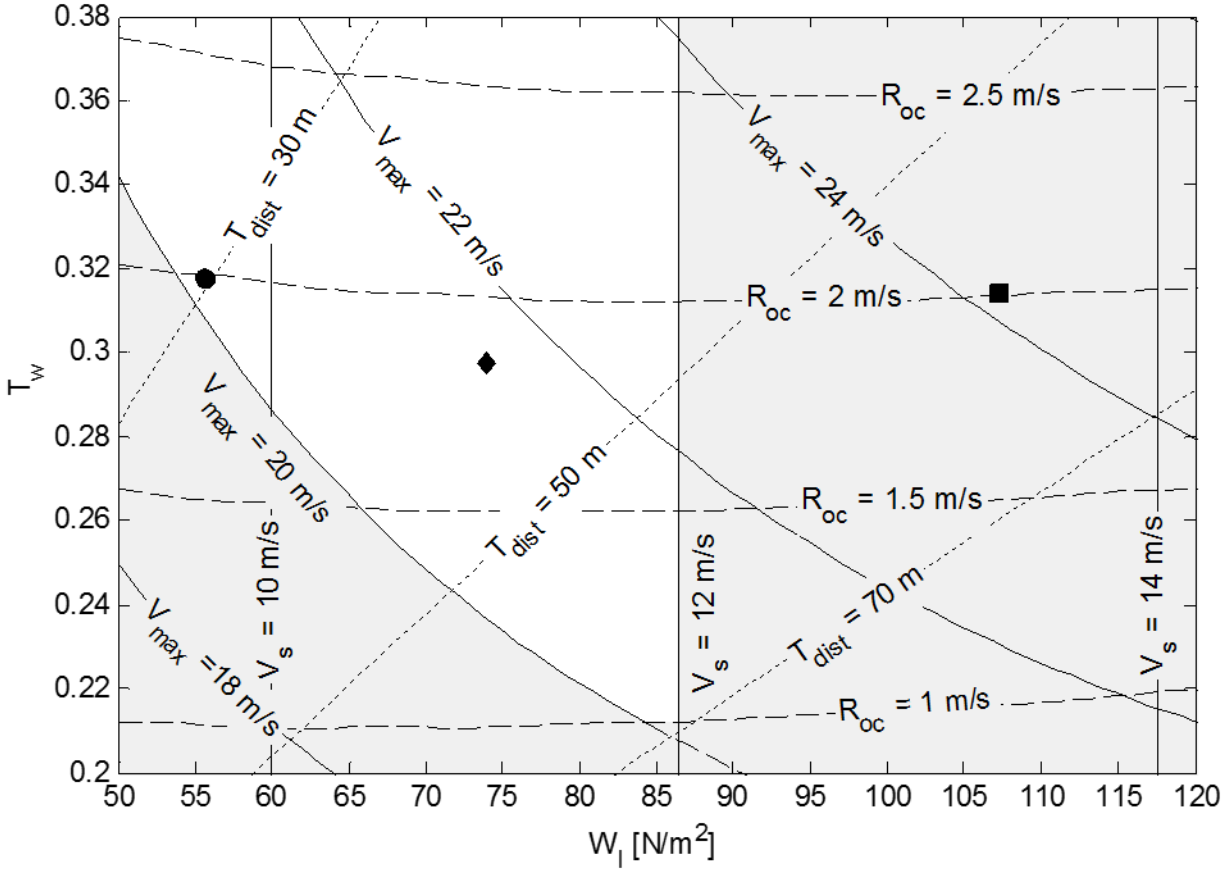

Figure 0.6: *Design region of the Genii aircraft. Grey denotes area outside design envelope. Square: full weight, diamond: flights 4-7, circle: preliminary design point. Solid vertical: stall, Solid decreasing: max level airspeed, Finely dashed: takeoff distance, Dashed: rate of climb.*

Regions outside the design space are shaded in grey; any aircraft with a wing area causing it to fall within the white space meets the design criteria. The extreme point with the highest valid W_l and lowest valid T_w represents a perfectly optimized aircraft for the design parameters; i.e. with the least thrust and least wing area for a given weight. Genii was not designed at this point because uncertainty in the final mass of the aircraft made it difficult to predict the exact optimized configuration.

The three points represented in Fig. (2.6) depict three configurations of the Genii aircraft over the design and flight history. The circle point represents the operating point initially taken during the preliminary design process. This configuration had an anticipated mass of 17kg and would utilize a Hacker A40-10L motor 6.7:1 gearbox, and an APC 27X12E propeller. This configuration was intended to operate only at the 1000W available from the fuel cell. The selection of a wing area of $3m^2$ allowed margin for the aircraft to be overweight. The $3m^2$ area is maintained for every Genii configuration. This area includes the area superimposed over the fuselage. The inclusion of this wing area in performance calculations is one of the many sources of uncertainty in the design, however its effect is partially offset by not including provisions for fuselage lift.

The diamond symbol represents the empty weight of the Genii aircraft when operating with a Hacker A60-20M motor and APC 20X15E propeller. This configuration was used for flights four through seven inclusive.

The square marker indicates the final aircraft operating point when ballasted to full weight. The final aircraft's configuration with the hydrogen system weight was 32.8 Kg, 1.93 times more than the initial design weight during the preliminary design process. The rate of climb, max airspeed, and takeoff performance were corrected by drawing an additional 1000W of power from reserve batteries. As shown later, the vehicle was still capable of operation from fuel cell power alone for level flight regimes. The excessive stall speed of 13.3 $^{m}/_{s}$ was not considered worth correcting by the added complexity of flaps, gurney strips, or wingtip extensions. As such, the aircraft in its final hydrogen configuration does not meet requirement number 2.

The development of the boundary lines in Fig. (2.6) is quite simple and can be derived from the basic lift and drag equations under the simplification of the steady flight condition

$$L = W = \frac{1}{2}\rho V^2 S C_l \tag{2.2}$$

$$D = W = \frac{1}{2}\rho V^2 S C_d \tag{2.3}$$

where L is wing lift, ρ is air density, V is the airspeed, D the total wing drag and C_l and C_d are the total wing lift and drag coefficients, respectively.

From Eqn. (2.2) if follows directly that for a given stall speed, V_{stall}

$$W_l = \frac{1}{2}\rho V^2 C_{lmax} \tag{2.4}$$

and

$$V_{stall} = \sqrt{\frac{2W_l}{\rho C_{lmax}}} \tag{2.5}$$

where C_{lmax} is the maximum lift coefficient before stall. C_{lmax} will depend on many factors including airfoil, Reynolds number, and high lift devices such as flaps. C_{lmax} was taken as 1.0 for preliminary work with the Genii aircraft. It is evident that under the simplification that lift is derived solely from the wing, the stall speed is independent of the aircraft's T_w.

The equation delimiting the takeoff requirement is derived from Newton's second law under the very simplistic assumption that the aircraft experiences no aerodynamic or friction drag and that the propeller produces constant static thrust over the duration of the takeoff run. Additionally, it is assumed that takeoff occurs exactly when the lift of the wing exceeds the weight of the aircraft when at C_{lmax}. No provision is made for time to rotate. Under these broad assumptions,

$$a = \frac{T}{m} = gT_w \tag{2.6}$$

where a is the aircraft's accleration, m its mass, and g the gravitational accleration constant. Integration in time leads to the following pair of equations

$$t = \frac{V_{stall}}{gT_w} \tag{2.7}$$

$$T_{dist} = \frac{gT_w t^2}{2} \tag{2.8}$$

where T_{dist} is the takeoff distance t is final time at takeoff. Substituting Eqn. (2.5) into Eqn. (2.7) and Eqn. (2.7) into (2.8) yields the simplified takeoff criteria

$$T_w = \frac{2W_l}{\rho g C_{lmax} T_{dist}} \tag{2.9}$$

The maximum rate of climb and maximum airspeed criteria are derived under the steady state climb assumption that

$$R_{oc} = \frac{P_p - P_d}{W} \tag{2.10}$$

where $R_{oc}$is the rate of climb, P_p is the propulsive power, and P_d is the drag power defined respectively,

$$P_p = TV \tag{2.11}$$

$$P_d = DV \tag{2.12}$$

where D is the total drag defined as

$$D = \frac{1}{2}\rho V^2 S(C_{dw} + C_{di} + C_{do}) \tag{2.13}$$

where C_{dw} is the wing parasitic drag coefficient, C_{di} is the induced drag coefficient, and C_{do} is a miscellaneous drag coefficient including any components such as fuselage, gear, empennage, ect, that are desired to be included in the preliminary design. The miscellaneous drag coefficient for

Genii is estimated at 0.02 with respect to the wing area. Further development of this number is the focus of Chapter 3.

The parasitic drag coefficient for the wing was approximated from a quadratic curve fit with respect to C_l from wind tunnel testing performed by Selig, Donovan and Fraser [1989]. In this manner the term C_{dw} becomes

$$C_{dw} = c_1\left(\frac{1}{\gamma}C_l\right)^2 + c_2\left(\frac{1}{\gamma}C_l\right) + c_3 \tag{2.14}$$

where $c_1, c_2,$ and c_3 are the quadratic term, lift slope, and zero lift drag coefficient of the airfoil respectively and γ is the ratio of the wing lift coefficient, C_l and the section coefficient c_l in the linear range. This value is a function of the wing's efficiency and is therefore affected by aspect ratio and the span efficiency factor e. Initial instigation of aspect ratio described later in this subsection predicts γ to be 0.80. The $c_1, c_2,$ and c_3 coefficients are a function of the Reynolds number of the wing, however they are assumed constant for this simplified analysis. The induced drag coefficient is easily determined as

$$C_{di} = \frac{{C_l}^2}{\pi e A_r} \tag{2.15}$$

where e is the wingspan efficiency factor and A_r is the aspect ratio, taken as 0.9 and 10.3 respectively for the preliminary Genii design. Span efficiency factor is used for this report rather than the common Oswald efficiency, because the profile drag has been related to the lift coefficient by the use of airfoil polars whereas Oswald efficiency accounts for all lift dependent drag terms combined. Substitution of appropriate drag terms into Eqn. (2.13) and substitution of Eqn. (2.13) into Eqn. (2.12) and Eqns. (2.11) and (2.12) into Eqn. (2.10) yields an expression for the required thrust to weight ratio advancing T_{wv} (as opposed to static, T_w) to obtain a desired R_{oc}

The expression must be developed for T_w rather than T_{wv} which requires some knowledge of the propeller's performance while advancing.

$$T_{wv} = \frac{1}{2}\rho V^2 S C_{dw} + \frac{2W_l}{\rho V^2 \pi e A_r} + \frac{1}{2}\rho V^2 S C_{do} + \frac{R_{oc}}{V} \tag{2.16}$$

$$T_w \delta \left(1 - \frac{V}{V_o}\right) = T_{wv} \tag{2.17}$$

A representation of a propeller's thrust vs airspeed is shown in Fig. (2.7). T_w is found from T_{wv} using a simple linear approximation such that

$$T_w = \left(\frac{1}{2}\rho V^2 S C_{dw} + \frac{2W_l}{\rho V^2 \pi e A_r} + \frac{1}{2}\rho V^2 S C_{do} + \frac{R_{oc}}{V}\right)\left(\delta - \delta \frac{V}{V_o}\right)^{-1} \tag{2.18}$$

where δ is an offset of the measured static thrust to account for propeller stall at low advance ratio and V_o is the airspeed at which the propeller stops producing thrust. δ for Genii's APC 26X15E propeller was found to be approximately 1.15 during testing and V_o to be 37 $^{m}/_{s}$.

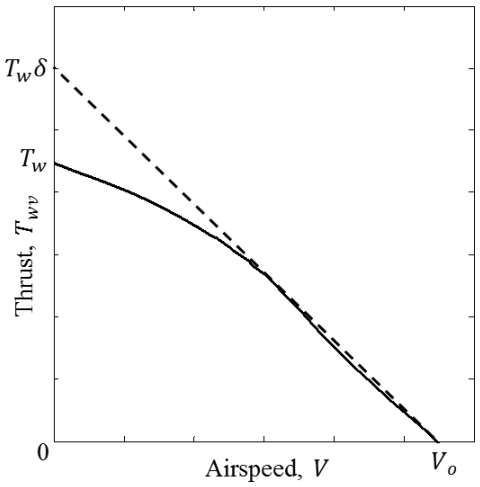

Figure 0.7: *Linear thrust assumption. Solid line: propeller performance. Dashed line: liner approximation.*

Substitution of Eqn. (2.16) into Eqn. (2.17) yields the corrected expression for static thrust to weight ratio required for a given wing loading and maximum rate of climb.

The airspeed, V for maximum rate of climb is not known at this point, however T_w can be found by solving $\frac{dR_{oc}}{dV} = 0$ or simply parameterizing over a range of airspeeds and finding the maximum R_{oc} within that range. It is a useful observation that

setting R_{oc} = 0 and substituting $V = V_{max}$ into Eqn. (2.18) yields an expression for the thrust to weight ratio required for a given maximum airspeed, V_{max} obtainable in level flight.

The constants V_o, e, and δ are not generally known to good fidelity in the initial design phases, which leads to further uncertainty. It should also be noted that the value of δ will be dependent on the propeller, and the lines in Fig. (2.6) representing R_{oc} and V_{max} are for the APC 26X15E corresponding to the final configuration represented by the square point. Slight variations in the curves will exist for the propellers used for the other two configurations.

With the wing area selected, other wing features were defined. The wing aspect ratio was selected as a qualitative optimization of induced drag vs structural weight and build complexity. Because high efficiency flight is not the goal of the current aircraft model, a lower aspect ratio than that found on many high-altitude-long-endurance (HALE) UAV's can be implemented to reduce wing stresses. Figure (2.8) shows the effect of aspect ratio on the 3D lift recovery and induced drag of the wing where C_l is the total wing lift coefficient and c_l is the section (2D) lift coefficient. For these plots, a span efficiency of 0.8 was assumed.

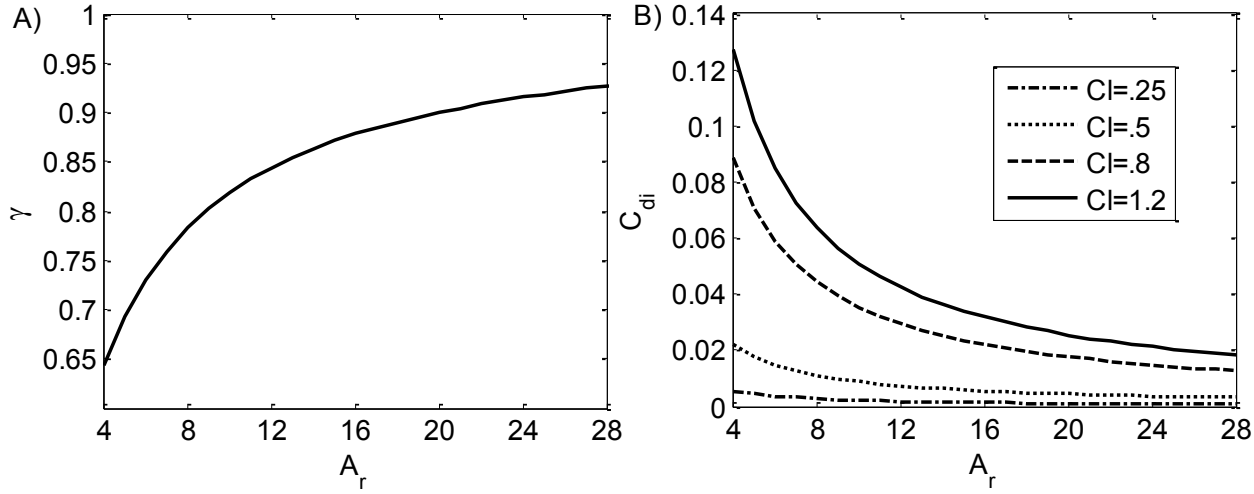

Figure 0.8: *Effect of aspect ratio. A) ratio of wing and section lift slopes in the linear range. B) Induced drag coefficient for various wing lift coefficients.*

An aspect ratio of roughly 10 was selected as this produced more than an 80% recovery of the 2D lift slope, and less than a 0.10 induced drag coefficient at large C_l. The diminishing return of higher aspect ratios did not justify their additional complexity for this aircraft. Final wing lofting modified the aspect ratio slightly to 10.3.

Wing twist was implemented to help prevent tip stall and wing-drop which can initiate a spin. Twist was set to 3º tip down in accordance with the recommendations in Raymer (2006). Proper selection of the taper ratio in conjunction with wing twist can yield a wing that displays a nearly elliptical lift distribution and high span efficiency. A complex numerical optimization of twist and taper was seen as unnecessary for the current model UAV, and the guidelines from Ramer (2006) were followed to set the taper. The wing was not swept but tapered linearly along a straight ¼ chord. For zero wing sweep and 3º of washout, this resulted in a taper of approximately 0.55. Final wing lofting resulted in the actual design taper ratio of 0.56. Vortex lattice method (VLM) analysis later proved this method produced span efficiencies of 0.96 and higher for small angles of attack.

The aircraft dihedral was set to produce the target rolling moment derivative due to sideslip of 0.05 as suggested in Raymer (2006). The effect of the wing placement on rolling stability is difficult to quantify and was estimated at this stage. Initial calculations showed a dihedral angle of 2º to be sufficient, however this was later raised to 4º after VLM simulations showed the aircraft could be spirally unstable in some flight regimes with the smaller value. Dihedral is constant off of the fuselage (rather than polyhedral) for build simplicity.

Wing incidence was set to place the fuselage at zero degrees α for an intended cruise velocity of 17 $^{m}/_{s}$. This would present the smallest cross sectional area to the wind for the cruise velocity.

Analysis showed this angle to be slightly greater than 4º. This final target value was set to 4º exactly due to manufacturing tolerances.

Ailerons were run along the span of the outer wing segments for a relative span of 0.63. From the guidelines in Raymer (2006), aileron relative chord was set to 0 .15. To keep from exceeding the 6 kg-cm torque capacity of the servos and to minimize torsion of thin surface, ailerons were broken in the center to create four surfaces, two per wing, actuated by one HS-485HB servo each. The size and deflection of the ailerons were not selected in an effort to produce a desired rolling moment, but were rather sized from experience with RC aircraft.

2.7 Empennage

The horizontal and vertical stabilizers are sized to produce the desired stability characteristics. This is performed in three steps. Initial approximation based on the suggested tail volumes as outlined in Raymer (2006), verification and modification of tail area based on the target stability margin for the horizontal and lateral derivative for the vertical, and a final eignemode analysis to check to dynamic stability. Tail length was optimized with respect to wetted surface area for the initial vertical and horizontal tail volume coefficients of C_{ht} = 0.7 and C_{vt} = 0.05 where the tail volume coefficients are defined as

$$C_{ht} = \frac{S_h L_h}{S M_{ac}} \tag{2.19}$$

$$C_{vt} = \frac{S_v L_v}{S b} \tag{2.20}$$

where S_h is the horizontal tail area, L_h is the distance from the aerodynamic center of the horizontal tail and the center of gravity of the aircraft, M_{ac} is the mean aerodynamic chord of the wing, S_v is the vertical tail area, L_v is the distance from the aerodynamic center of the vertical tail and the

center of gravity of the aircraft, and *b* is the wingspan. The surface area required for a given tail length is shown in Fig. (2.9). The wetted surface area was computed as the sum of the two stabilizer areas and the surface area of the cylindrical tail boom.

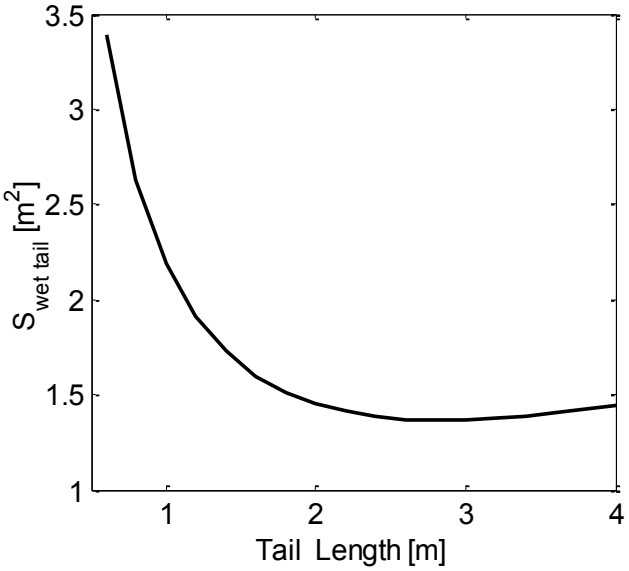

Figure 0.9: *Wetted area required for target tail volume with respect to tail length.*

Minimum wetted tail surface area occurs at 2.8 meters, however a sacrifice had to be made for transportation. Tail length was designed to 2m. Additionally, structural considerations drive the tail boom shorter as a longer tail boom requires more structural weight for a given bending and torsional stiffness. The vertical stabilizer was placed 15cm forward of the horizontal. This helped expose more rudder to clean air in the event of a spin. This approximately places ½ of the rudder area outside the region of the vertical blanketed by the stalled horizontal stabilizer.

Horizontal area was reduced from 0.552m^2 (C_{ht} = 0.7) to 0.527m^2 (C_{ht} = 0.624) to produce a desired stability margin of 20% with the CG located at the wing ¼ chord. The target yawing moment derivative with respect to yaw, C_{nb}, was 0.1 as given by Raymer. Following this target produced a vertical tail volume coefficient smaller than any of those recommended in the same text. This discrepancy may be in the scale of the aircraft. For safety the vertical tail size was chosen slightly larger than minimum with an area of 0.225m^2 (C_{vt} = 0.025). This places C_{nb} at 0.64. This volume is slightly larger than that suggested for single place light aircraft because the

decision had not yet been made if Genii should be single or multi engine. Multiple engine aircraft typically have large tails and rudder to counter adverse yaw in the event of a motor failure.

The elevator spanned 88% of the horizontal stabilizer with a depth of 43% of the mean aerodynamic chord as recommend for sailplane aircraft by Raymer (2006). This is only 2% smaller than recommended for general aviation single engine. For redundancy and to reduce the control forces on the elevator, the surface was split in two along the longitudinal axis and actuated by two servos. The rudder spanned 87% of the vertical stabilizer with a chord of 48% M_{ac}. This is 8% larger than the 40% recommend by Raymer for sailplanes and general aviation single aircraft, because at the time, the aircraft was intended to be used with a locked nosewheel. The extra rudder area was hoped to provide better lateral control during takeoff, however the nosewheel has since been replaced with a servo-steered version so the aircraft can be taxied. Servo mounting for both elevators and rudder was, in the RC experience of author, assumed to be sufficiently stiff that mass balancing of the surfaces to prevent flutter was not necessary for the current aircraft.

2.8 Fuselage

Lacking sufficient resources to perform an aerodynamic optimization of the fuselage shape considering the necessary elements such as propwash, the fuselage was lofted with a few simple guidelines. The fuselage was designed around the required internal components located such that the CG is placed at ¼ chord. The fuselage's length is 1.87m. Special attention was paid to prevent negative curvature that would facilitate flow separation. The transition aft from the propeller was made as smooth and shallow of slope as possible given the internal constraints to minimize trust degradation from the presence of the fuselage. Cross sectional area was kept as small as possible while accommodating the required payload. The maximum cross sectional area is 1.25m^2.

2.9 Landing Gear

The landing gear was sized to place the propeller's rotational axis 0.42m above the ground plane. This leaves 7.7 cm (10% the propeller diameter) of clearance when equipped with the APC 27X13E. The aircraft was designed with a tricycle configuration, which in the experience of author produces an aircraft that is easier to control and steer on the ground and during takeoff. The main gear was placed 10cm aft of the CG, placing 10.3% of the load on the front gear. The nose gear was raked forward 10º, placing the center of tire rotation 0.8cm forward of the tire contact location, to help damp wheel shimmy. No such rake was implemented on the main gear for construction purposes. The main gear were angled down at 30º for a wheel stance of 0.92m. The tipback angle is 22º,the wing-strike angle is 15º and the turnover angle is 76º.

2.10 Materials and Construction

The aircraft was constructed using wet-composite layup techniques. The fuselage is a monocoque structure with bulkheads comprised of a fiberglass laminated aeromat core. Negative molds of the fuselage were cut by a computer controlled router and prepared with a gel coat mold surface. The top and bottom fuselage laminates were vacuum bagged in separate molds and joined together after installing plywood bulkheads.

The wing is composed of a structural carbon fiber tube 2.7 cm outer diameter 2.2 cm inner diameter, expanded polystyrene core, and a fiberglass outer skin. The carbon fiber spar was designed to take the bending loads of the fully weighted aircraft with a 4 Gee envelope. The core material was cut to the airfoil shape using formica templates and a hot wire. Fiberglass was applied to the outside of the wing for torsional stiffness and protection. An aft spar bridges the break line

for the outer wing to take torsional load and carbon fiber ribs inserted into the foam distribute this load to the skin.

The empennage surfaces are constructed in the same manner as the wing, but use heaver weight fiberglass to take the bending load though the skin so that a spar is not required. The tail boom is made from a carbon fiber tube of 3.7 cm outer diameter and 3.5 cm inner diameter for bending and torsional stiffness. The torsional stiffness of the boom was found to be barely satisfactory for Genii's low speed operation, due to the small diameter and the lack of ±45º fiber orientation in the pultruded rod.

For simplicity, the front gear is a spring strut for large RC aircraft and is rotatable by means of a set of bearings and a servo in the fuselage. The aft gear are comprised of a carbon fiber tube inserted over and pinned to a steel rod held captive by internal bullheads and protruding from the exterior of the aircraft. A steel shoulder and axel are affixed in the opposite side of the rod. 10.2 cm Dubro pneumatic tire is used for the front gear and 12.7 cm plastic wheels for mobility walkers were found to work well for the rear.

The motor is held captive in the fuselage by means of an aluminum mount bolted to a composite bulkhead connected to the skin. Plywood framing inside the fuselage allows easy reconfiguration of internal payloads, fuel cell, and tank. Servos are held captive in the wing in basswood enclosures. The tail boom inserts into a titanium receptacle in the aft fuselage and is bolted in place via a stud protruding into the fuselage. It is constrained in rotation by a captive pin and mating slot. A cotter pin is also inserted through the nested tubes for security should the bolt loosen. For the servo control wires, a Glenair 10 pin bayonet style connector is utilized for quick disconnect of the tail and Glenair 6 pin screw type connectors allow easy removal of the wing sections.

2.11 Datalogging

Of critical importance to the Genii project was the determination of the vehicle's flight characteristics for comparison against steady-state performance calculations. The vehicle was instrumented with several onboard data acquisition (DAQ) systems to record parameters of interest during flights. Like the vehicle itself, several iterations of the final DAQ system were utilized over the fourteen flights. The system utilized for flights 10 through 14 will be enumerated in this subsection.

The final DAQ system utilized on the Genii aircraft was system specific, however the components are readily available, of low cost, and could prove useful for instrumented similar vehicles. The DAQ on Genii consists of several modules: a flight data recorder, a separate datalogger, an instrumented ESC, and several sensors including a pressure transducer, hall-effect current sensors, and several thermocouples. A breakdown of all the parameters measured, and the devices in which they are measuring is given in Table. (2.2).

The primary flight data recorder was an ArduPilot Mega and is shown on the right in Table (2.2) along with the parameters logged. If an external sensor or module is used rather than an integral sensor to the board, it is listed as well. An additional data acquisition unit was used to sample channels not logged by the ArduPilot. A Raspberry Pi microcomputer was utilized for this purpose. Several parameters were logged by both systems and are shown in dark grey.

Table 0.2: *Datalogging scheme for the Genii aircraft.*

Logger	Instrument (if not internal)	Parameter	Instrument (if not internal)	Logger
		GPS Status	GPS Module	Ardu Pilot Mega
		Timestamp	GPS Module	
		Number of Satellites	GPS Module	
		Dilution of Precision	GPS Module	
		Latitude	GPS Module	
		Longitude	GPS Module	
		GPS Altitude	GPS Module	
		Ground Speed	GPS Module	
		Ground Course	GPS Module	
		Magnetic Field Values x,y,z	Compass Module	
		Roll		
		Pitch		
		Yaw		
		Linear Acceleration x,y,z		
		Angular Velocity x,y,z		
		Pressure Altitude	Barometric Altimeter	
		Command Inputs		
Raspberry Pi	Pressure Transducer	Airspeed	Pressure Transducer	
	ESC	Propulsion Voltage	Voltage Divider	
	ESC	Propulsion Current	Hall-Effect Sensor	
	ESC	Motor RPM		
	ESC	ESC Temperature		
	Thermocouple	Battery Temperature		
	Thermocouple	Diode Bridge Temperature		
	Thermocouple	Ambient Temperature		
	Hall-Effect Sensor	BEC Current		
	Voltage Divider	BEC Voltage		

2.11.1 Ardupilot

The main source of flight information from Genii was an ArduPilot Mega APM2 (Arduino Pilot Mega Multplatform Autopilot, 3D Robotics). Despite its low cost, the ArduPilot unit provides a large number of features including fully-autonomous flight capabilities, data logging, and live telemetry link to the ground. The unit consists of the main board with microprocessor, a global positioning system (GPS) module, a compass module, a barometric altimeter module, a telemetry

module both on-aircraft and at the ground station, and an open source software package for programming and controlling the ArduPilot as well as viewing live data.

The ArduPilot unit installs between the receiver and servos, either passing flight input from the pilot through the board, or generating control inputs itself. Table. (2.2) shows a list of the parameters stored in the onboard flight recordings.

The GPS module is a Mediatek MT3329 mounted externally to the main board. This unit allows the ArduPilot to record the GPS status, time, number of satellites, dilution of precision, latitude, longitude, altitude, ground speed, and ground course.

A HMC5883L 3 axis magnetometer unit allows for the determination of heading. This is primarily useful for autonomous operations. Large electro-magnetic interference from the motor caused inaccuracies in heading readings despite the addition of capacitors to the propulsion power supply. For later calculation of turn rate, the rate change in ground course from the GPS was utilized rather than the rate change of heading.

The ArduPilot utilizes an MPU-6000 three dimensional accelerometer and gyroscope chip installed on the main board. This allows recording of x,y,z accelerations and x,y,z rotational rates relative to the board.

An external module consisting primary of a MS5622-01 BA03 barometric pressure sensor is utilized to record pressure altitude. The pressure altitude was found to be more reliable than GPS altitude and is utilized for all subsequent altitude reporting.

Three additional analog inputs allow for the recording of propulsion system voltage and current as well as airspeed. The software is programmed to accept these as voltage inputs, and a zero voltage

and linear calibration factor for each are all that is required for the software to record and report these parameters in their dimensional form. Although sensor modules are available from 3D robotics to measure voltage, current, and differential pressure, the Genii project utilized their own sensors. A voltage divider consisting of two resistors was used to measure propulsion system voltage while an ACS758LCB-100B hall-effect sensor was utilized to measure current. Differential pressure from an United Sensor PBB-12-F-9-KL 717 pitot tube is measured by an Ashcroft Xldp 1.5" differential water column pressure transducer and its current output converted to a voltage input to the ArduPilot with a simple resistor bridge.

The ArduPilot offers a live link function to the ground station to provide live telemetry data as well as updates to the autonomous flight plan. Nearly every parameter can be re-flashed in flight such as the autopilot's proportional-integral-derivative gains or compass bias. This functionality is provided by a 3DR Robotics 910 Mhz telemetry kit consisting of a 100 mW aircraft and ground module and antenna.

2.11.2 Raspberry Pi

Several other parameters, chiefly motor rpm and temperatures of various components were desired to be logged in addition to the base capabilities of the ArudPilot. Due to the open-source programing of the ArduPilot, the ArduPilot's code could conceivably be modified to log additional unused analog inputs on Arduino board from which the unit is derived. This was, however considered too dangerous for the Genii setup. Because the ArduPilot is a single-point failure between the receiver and controls, no modifications were performed, to help prevent the unit from hanging and the resulting loss of the aircraft. As such, a secondary data acquisition system was

developed to log the additional parameters. A Raspberry Pi B756-8308 (abbreviated RPi) microcomputer was utilized for this purpose.

A special thanks is extended from the author to Patrick Gavin and Ryan Brooks for their development of the Raspberry Pi DAQ system. The system ran a Linux based operating system and utilized three Texas Instruments ADS7828 analog to digital converters with an I2C interface to log three analog channels. These channels were airspeed from the Ashcroft pressure transducer and the voltage and current of the battery eliminator circuit (BEC), measured directly and using the voltage drop across a resistor, respectively. Three type K thermocouples were also logged by the RPi via three I2C thermocouple modules.

The motor rpm was not capable of being logged by the standard ArduPilot features. A method for the use of ground based DAQ during propeller testing is described in Chapter 5. This technique utilizes a photo-encoder to sample one of the three AC phases to the brushless motor. By filtering out the high-frequency PWM used to control motor speed, the low frequency phase switching can be extracted and converted to rpm knowing the poles of the motor and gearbox ratio. This technique was not found to work well with the RPi equipment in the air due to large amounts of electrical noise in the system that did not affect the heavy LabView setup used for ground testing. As such, for air sampling of motor rpm and other ESC parameters a different technique was utilized. The Jeti Mezon 75 15S Opto ESC that was utilized for final flights does not perform time-domain data logging but does include sensors to report motor rpm, current, voltage, and ESC temperature to a telemetry system. The serial interface to the ESC was tapped and read by the RPi. When interrogated by the RPi, the ESC's reply is read by the RPi and the appropriate

parameters are parsed from the response and stored. This technique is utilized for the logging of motor rpm, ESC temperature, and propulsion current and voltage.

Propulsion system current and voltage as well as airspeed are logged redundantly on both RPi and ArduPilot. Airspeed is taken from the RPi log because it can be displayed as a raw voltage rather than a corrected airspeed, allowing the correction to be performed later. Airspeed is recorded from the same sensor so both logs are equivalent. Current and Voltage are taken from the AruPilot log because the voltage divider and hall-effect sensor were found to be more accurate than the ESC's built in hardware. The hardware used by the ESC to measure these parameters is unknown.

CHAPTER 3

3.1 Performance Prediction and Methodology

To assure a UAV or aircraft meets its design requirements and to facilitate final configuration changes in detailed design, it is paramount that the performance of the aircraft be computed as accurately as possible. While the previous section outlined some rudimentary techniques used to help preliminarily size the Genii aircraft, this chapter will report the methods used to calculate the performance for direct comparison against flight testing presented in Chapter 5. The primary parameters to be investigated and compared to flight test results are:

1) The maximum obtainable airspeed in level flight, V_{max}

2) The rate of climb as a function of airspeed and its absolute maximum, R_{oc} and $R_{oc_{max}}$

4) The glide ratio as a function of airspeed and its absolute maximum, G_r and $G_{r_{max}}$

3) The minimum power required for level flight and the airspeed at which it occurs, P_{min} and $V_{p_{min}}$

4) The turn radius as a function of airspeed, R

5) The minimum takeoff distance, D_{min}

Additionally, descriptions of the computed stall speed V_{stall} as well as the aircraft's static and dynamic stability will be discussed, although direct measurements of these values from flight testing were not recorded.

3.2: Aircraft Drag Components

The total drag of the Genii aircraft at a given velocity is computed with a component buildup method taking into account the following drag terms.

$$D_{tot} = qS\left(C_{d_w} + \left(1 + 0.5(\eta - 1)\right)C_{d_g} + C_{d_c} + C_{d_{sp}} + \eta\left(C_{d_f} + C_{d_d} + C_{d_e}\right)\right) \quad (3.1)$$

where C_{d_w} is the total drag coefficient of the wing, C_{d_g} is the drag coefficient of the gear, C_{d_c} is the drag coefficient of attached cameras, $C_{d_{sp}}$ is the stopped propeller drag coefficient if applicable, η is the dynamic pressure ratio to account for additional drag of components in the propwash, C_{d_f} is the fuselage drag coefficient, C_{d_d} is the drag coefficient of the inlet duct, and C_{d_e} is the empennage drag coefficient comprised of components resulting from the tailboom, vertical stabilizer, horizontal stabilizer, and elevator trim. The modifying term to the landing gear's drag coefficient, $\left(1 + 0.5(\eta - 1)\right)$, simply accounts for only partial submersion in the propwash. The landing gear drag is increased by only half of the additional dynamic pressure ratio. All drag coefficients are expressed with respect to the wing's reference area, S and q is the dynamic pressure given as

$$q = \frac{1}{2}\rho V^2 \quad (3.2)$$

where ρ is the air desity at the experienced temperature and pressure and V is the airspeed. The gear, wing, and empennage all have small interference components which are included within the corresponding coefficient rather than expressed individually in Eq. (3.1).

3.2.1: Wing

The drag of the wing stems from several sources and the wing's drag coefficient can be expressed as.

$$C_{d_w} = C_{d_p} + C_{d_i} + C_{d_{mis}} \tag{3.3}$$

where C_{d_p} is the wing's profile drag coefficient, C_{d_i} is the induced drag coefficient, and $C_{d_{mis}}$ are the miscellaneous effects from interference with the fuselage and leakage around the ailerons.

Profile drag results from the pressure distribution over the wing and the wing's skin friction drag. Although some literature such as Raymer (2006) calculate profile drag using a form factor and skin friction coefficient, it is most accurate to utilize actual wind tunnel tests to determine its value. One common approach, such as that given in Anderson (2001), is to assume the profile drag is comprised of a minimum C_{d_p} offset (often called the zero lift drag coefficient), $C_{d_{p0}}$ and is quadratically related to the lift coefficient, C_l as follows

$$C_{d_p} = C_{d_{p0}} + kC_l^{\,2} \tag{3.4}$$

here k is a quadratic coefficient. Confusion can result here as some texts ignore the quadratic dependence for simplification or include it with the induced drag because of its dependence on C_l. A notional plot of the profile drag coefficient for an uncambered and cambered airfoil section is given in Fig. (3.1) by a solid and dashed line, respectively. Lower case c_l and c_d are used to express section properties as opposed to wing-averaged properties. An uncambered airfoil would be described well by Eq. (3.2), however many cambered airfoils experience their minimum profile drag at positive c_l, not at zero lift. Including only a constant and quadratic term in Eq. (3.4) is a useful approximation if empirical formulations are to be used.

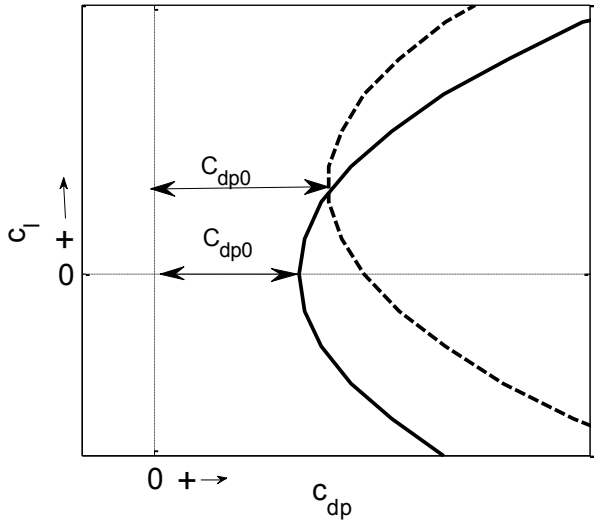

Figure 0.1: *Notional performance for an uncambered (solid line) and cambered (dashed line) airfoil.* $C_{d_{p0}}$*: point of minimum drag.*

The technique described herein, however, utilizes wind tunnel data. The ease of performing polynomial regressions to the wind tunnel data makes it desirable to add both a linear and cubic term to Eq. (3.4) to account for the bias of $C_{d_{p0}}$ and to catch more higher order effects resulting from the movement of the boundary layer transition point or the size and location of laminar separation bubbles with respect to C_l. Equation (3.5) is the profile drag equation used for this report.

$$C_{d_p} = C_{d_{p0}} + c_1 C_l + c_2 {C_l}^2 + c_3 {C_l}^3 \tag{3.5}$$

where c_1, c_2, and c_3 are the linear, quadratic, and cubic coefficients, respectively. Uncertainty arises in the use of Eq. (3.5) because the wing's total lift coefficient is utilized rather than the section properties from which the coefficients are derived. In essence, the section's profile drag properties are known from wind tunnel testing but the wing's profile drag may differ due to spanwise effects. Three techniques can be used to predict the wing's total C_{d_p}.

1) All lift dependent terms in Eq. (3.5) can be ignored, such as in Raymer (2006), leaving only $C_{d_{p0}}$, which plots of the effect of aspect ratio given by Prandtl (1923) are shown to be nearly the same for both section and wing.

2) The $C_{d_p}(c_l)$ relationship is assumed to be the same as $C_{d_p}(C_l)$, I.E. the wing's total lift coefficient is used in place of the section coefficient.
3) C_{d_p} can be computed as the integral of c_d along the span calculated from the local c_l's as given in Eq. (3.6). This technique is given in Abbot and Doenhoff (1959) and is assumed to be the most accurate of the three.

$$C_{d_p} = \frac{2}{S}\int_0^{b/2} c_d \mathrm{c}\ \mathrm{dy} \tag{3.6}$$

where b is the wingspan, S is the wing area, and c is the local chord length.

Method 2 is ideal for this report as the exact c_l distribution for every flight condition is difficult to calculate. The comparative accuracy between methods 2 and 3 is not well quantified in literature and an investigation is performed for the specific airfoil and wing used for the Genii aircraft. The absolute accuracy of method 3 remains unquantified.

Abbot and Doenhoff (1959) present a method for determining the c_l distribution for an unswept wing with linear twist and taper using Eq. (3.7).

$$c_l = \frac{\gamma a_e S}{cb} L_b + C_l \frac{S}{cb} L_a \tag{3.7}$$

where γ is the twist distribution, negative for washout, a_e is the effective lift slope, and L_b and L_a are constants determined at different spanwise stations as a function of aspect ratio and taper ratio. The effective lift slope is given as

$$a_e = \frac{a_0}{E} \tag{3.8}$$

where a_0 is the section lift slope and E is the ratio of the semipertimeter of the wing to the wingspan where the wing's semipereimter is the sum of the tip chord and the leading edge length and trailing edge length of one side of the wing.

For a given C_l, Eq. (3.7) is used to determine the lift distribution, the section's performance is used to compute the section profile drag from c_l and Eq. (3.6) is used to compute the total profile drag. Values of L_a and L_b are only provided by Abbot and Doenhoff (1959) for eight spanwise stations, therefore a quadratic interpolation is performed between these points to refine the numerical integration of Eq. (3.6).

The wing's profile drag computed in this manner (method 3) is plotted with that computed by Eq. (3.5) (method 2) in Fig. (3.2A) with solid and dotted lines, respectively. The ratio of the method 2 technique to the method 3 techniques is shown in Fig. (3.2B). A maximum error of 3% is noted, well within the tolerance of the methods applied for this work. Therefore, method 2 is applied for all further calculations of profile drag.

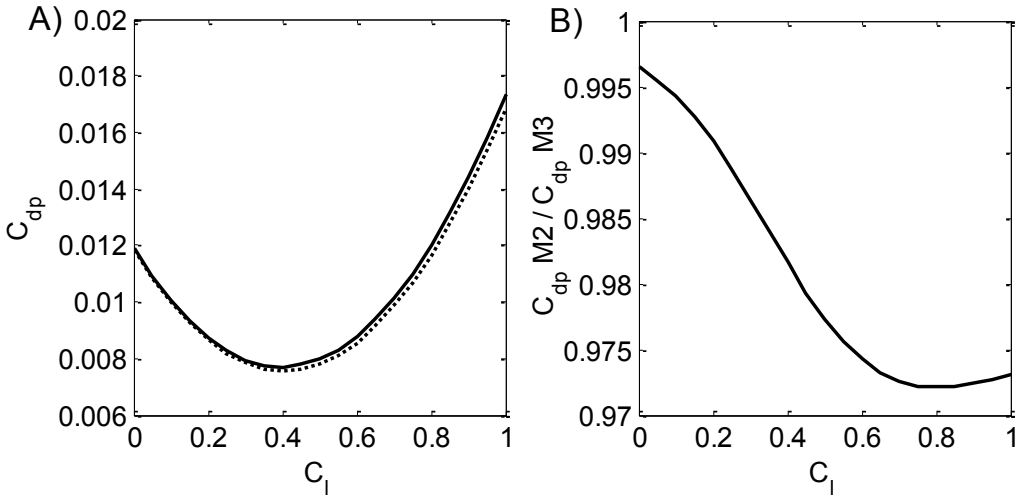

Figure 0.2: *Assessment of profile drag computation. A) Wing profile drag coefficient with respect to wing lift coefficient. Solid line: method 1. Dashed line: method 2 B) Ratio of wing profile drag coefficient from methods 1 and 2 with respect to wing lift coefficient.*

The lift-drag polar for the SD 7037 airfoil is taken from the low-speed wind tunnel testing results of Selig et al. (1995). The performance of the airfoil is dependent on Reynolds number

$$R_e = \frac{\rho V c}{\mu} \tag{3.9}$$

where μ is the dynamic viscosity of air at a given temperature and pressure. The performance from Selig's testing is shown for three different Reynolds numbers, 304300, 230600, and 102200 which are depicted in Fig. (3.3) as X's, circles, and crosses, respectively. The light dash-dot line in Fig. (3.3A) is included for reference and denotes the common $2\pi\alpha_r$ lift slope for a flat plate and a zero lift offset of 0.32, where α_r is the angle of attack in radians. The section's max lift coefficient is roughly 1.24, zero lift angle of attack -2.8 degrees, and the best lift to drag ratio is 69.7 at an angle of attack of 5 degrees. These characteristics, however, vary with Reynolds's number.

To simplify the computation of C_{d_w} , the wing is assumed to operate at a uniform Reynolds number approximated as the Reynolds number at the mean aerodynamic chord given by Eq. (3.10)

$$M_{ac} = \frac{2}{S}\int_0^{\frac{b}{2}} c^2 dy \tag{3.10}$$

The M_{ac} for Genii is 0.56. Due to project creep in both stall and maximum airspeed, the Reynolds number range of the wing for the Genii aircraft is 480000 to 1100000, which is outside the range of documented wind tunnel data for the SD7037.

The software, Xfoil by Mark Drela (Xfoil Subsonic Airfoil Development System 2013) can be utilized to good effect to calculate inviscid and viscous drag over airfoil shapes. The methodology of the Xfoil code is outlined in Drela (1989) and the boundary layer formulations are described in Drela and Giles (1987).

Xfoil was used to calculate section lift and drag values for the SD 7037 airfoil with 200 panels. The results are also depicted in Fig (3.3) as dotted, dashed, and solid lines corresponding to R_e = 304300, 203600 , and 102200, respectively.

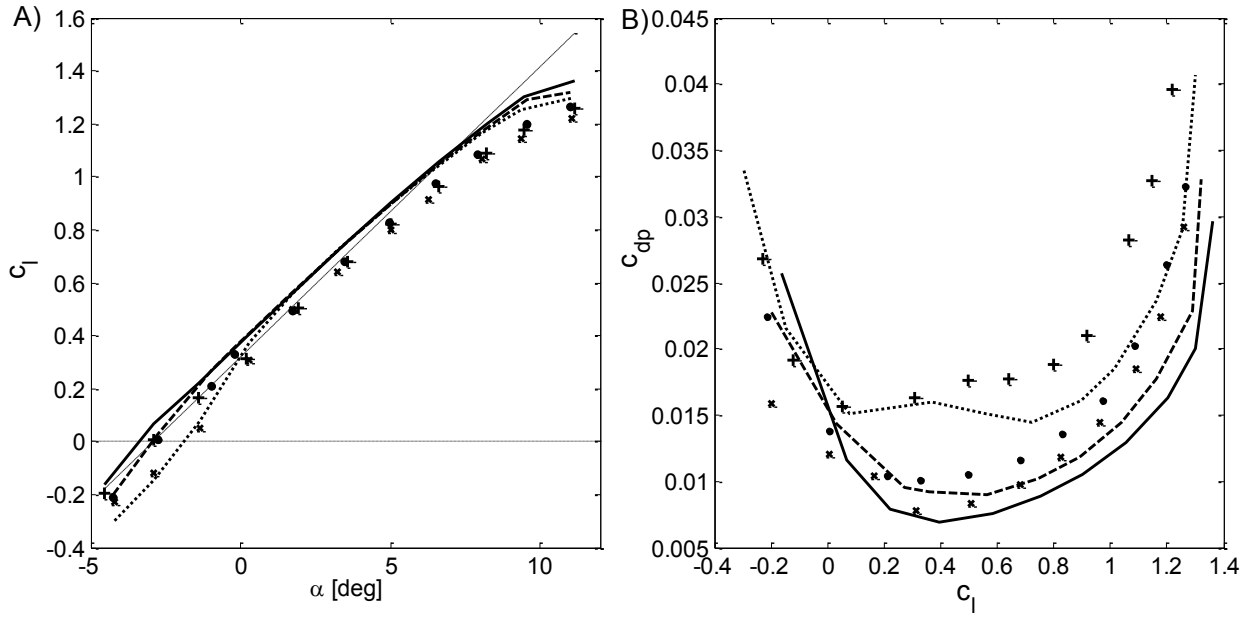

Figure 0.3: *Section performance for the SD 7037 airfoil A) lift coefficient vs angle of attack. B) profile drag coefficient vs angle of attack. Crosses: Selig et al. (1995)* R_e *= 102200, Dots:* $Selig\ et\ al.(1995)$ R_e *= 203600, "X's": Selig et al.* (1995) R_e *= 304300, Dotted Lines: Xfoil* R_e *= 102200, Dashed Lines: Xfoil* R_e *= 203600, Solid Lines: Xfoil* R_e *= 3404300, Dash-Dot line:* $c_l = 2\pi\alpha_r$.

It is evident that Xfoil over predicts lift and under predicts drag for the SD7037 in this R_e range. The difference between Selig's wind tunnel data and Xfoil's calculations for the three R_e analyzed is shown if Fig. (3.4A) as X's, circles, and crosses, corresponding to R_e = 304300, 203600, and 102200 respectively. The error can be on the order of 20 percent. As such, a more accurate scheme than utilizing unmodified Xfoil calculations is desired.

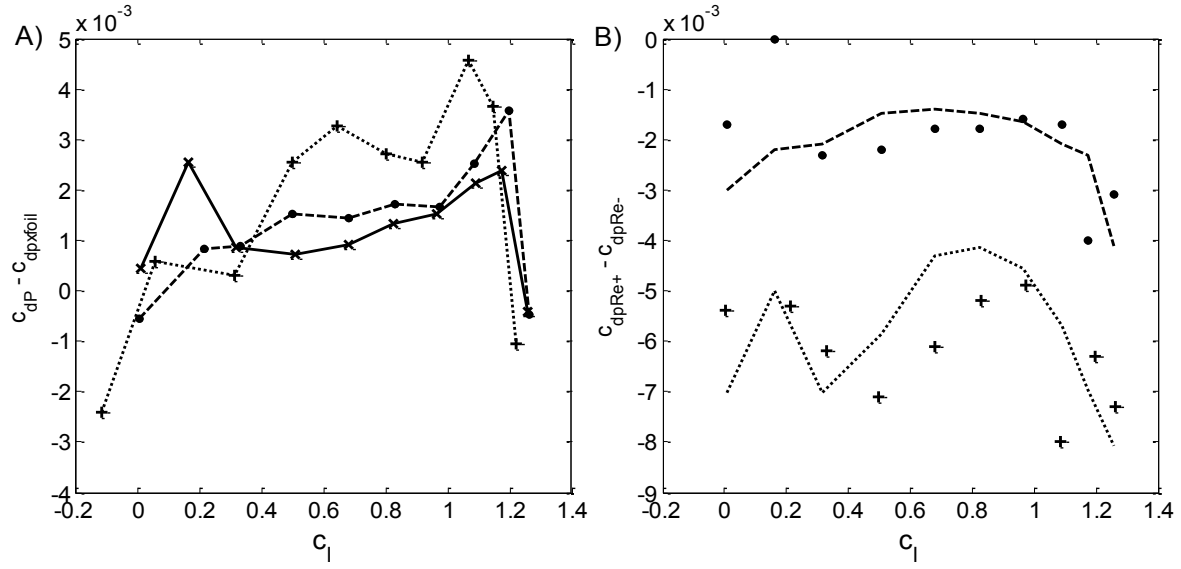

Figure 0.4: *Comparison of profile drag between VLM and wind tunnel testing. A) difference between wind tunnel data from Selig et al. (1995) and Xfoil calculations for the profile drag coefficient of the SD 7037 airfoil with respect to section lift coefficient at different Reynolds numbers. Crosses: R_e = 102200, Dots: R_e = 230600, "X's": R_e = 304300. B) Change in profile drag coefficient between R_e = 102200 to 203600 (dotted line and crosses) and R_e = 203600 to 304300 (dashed line and dots) with respect to section lift coefficient. Dots and crosses: data from Selig et al. (1995), Dashed and dotted lines: calculations from Xfoil.*

Figure (3.4B) depicts the change in drag coefficient from Selig's data between R_e= 203600 to 304300 (dots) and R_e = 102200 to 203600 (crosses). Similarly, the dashed line represents the change in drag coefficient from Xfoil from R_e = 203600 to 304300 while the dotted line represents the change in drag coefficient from R_e = 102200 to 203600.

A comparison of Figs. (3.4A) and (3.4B) indicates that the magnitude of the error between the difference in c_d between R_e = 203600 and R_e = 304300 is less than the direct error between wind tunnel and Xfoil data at R_e = 304300. This indicates that for this airfoil and R_e range, Xfoil is

more accurate at predicting $\frac{dc_d}{dR_e}$ than c_d alone. From this observation, this report calculates the performance for the SD7037 airfoil at R_e above 300000 as a linear extrapolation of the wind tunnel test data at R_e= 304300 using $\frac{dc_d}{dR_e}$ as calculated by the difference between Xfoil computations for R_e = 300000 and R_e = 1000000. This extrapolation can be expressed by Eq. (3.11)

$$c_d = c_{d_{0.3M}} + \left(c_{x_{1.0M}} - c_{x_{0.3M}}\right)\frac{R_e - 300000}{1000000 - 300000} \tag{3.11}$$

where, $c_{d_{0.3M}}$ is the drag coefficient as determined by Selig at R_e = 304300, $c_{x_{1.0M}}$ is the drag coefficient as determined by Xfoil at R_e = 1000000, and $c_{x_{0.3M}}$ is the drag coefficient as determined by Xfoil at R_e = 300000.

Use of Eq. (3.11) requires the relation between functions be continuous. As such, $c_{w_{0.3M}}$, $c_{x_{1.0M}}$, and $c_{x_{0.3M}}$ are approximated by third order polynomial regressions such that:

$$c_{d_{0.3M}} \cong 0.01248 - 0.01543c_l + 0.00696{c_l}^2 + 0.01197{c_l}^3 \tag{3.12}$$

$$c_{x1.0M} \cong 0.00809 - 0.01098c_l + 0.00832{c_l}^2 + 0.00344{c_l}^3 \tag{3.13}$$

$$c_{x_{0.3M}} \cong 0.01110 - 0.00735c_l - 0.00855{c_l}^2 + 0.01628{c_l}^3 \tag{3.14}$$

Performance post-stall is not accounted for. Figure (3.5) graphically depicts the extrapolation. Crosses indicate Selig's data for R_e = 304300 and the solid line notated R_e = 0.3E6 is $c_{w0.3M}$. $c_{x0.3M}$ and $c_{x1.0M}$ are the upper and lower dash-dot lines respectively. The solid line labeled R_e = 1E6 is the extrapolated c_d for R_e = 1000000. Under the assumption of method 2 as described above, Eq. (3.11) through (3.14) are utilized to determine the wing's parasitic drag by use of the total lift coefficient C_l rather than the section coefficient c_l from which the expressions are developed. This can be expressed as

$$C_{d_p} \cong c_d \; when \; c_l \to C_l \tag{3.15}$$

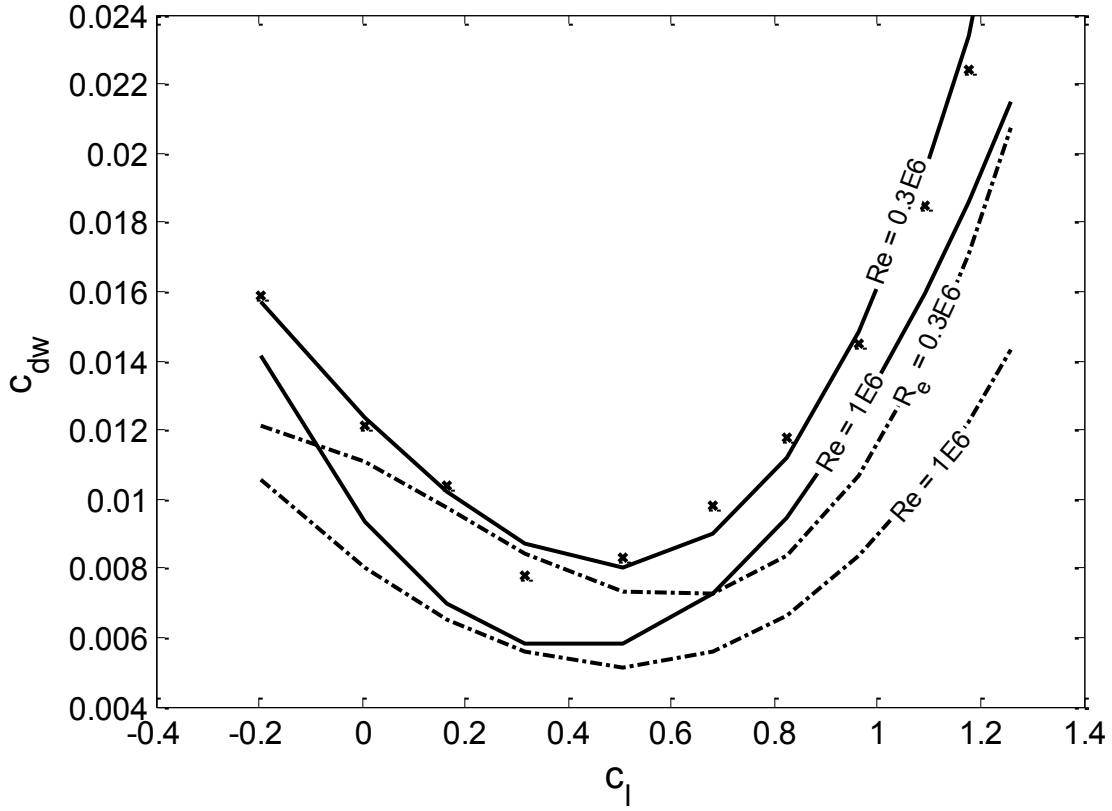

Figure 0.5: *Extrapolation of the profile drag coefficient of the SD7037 airfoil to higher R_e using data from Xfoil. "X's": data from Selig et al. (1995), R_e = 304300. Dash-dot lines: Xfoil calculations. Solid lines: extrapolated profile drag coefficient via Eq. 3.11*

The second component of wing drag in Eq. (3.3) is the induced drag resulting from 3D effects. Spanwise flow driven by the pressure difference between the top and bottom of the wing results in the development of a vortex near the tip of each wing. The effect of these vortexes can be approximated mathematically by applying a downwash at each spanwise station in accordance with the vortex equation for potential flow

$$V_{dw} = \frac{\Gamma}{2\pi y} \tag{3.16}$$

where Γ is the vortex intensity and y is the distance inboard of the tip. Eq. (3.16) demonstrates how the downwash intensity decreases in both magnitude and slope as y increases. The downwash component at each spanwise station is superimposed to the local free-stream velocity vector, decreasing the effective angle of attack and reducing lift at that section with respect to that which would be suggested by the angle of attack to the free-stream. This reduction in total lift must be taken into account, however induced drag also arises from this phenomenon. We can imagine that the downwash at a wing section has effectively rotated the local freestream velocity vector clockwise about the y axis (+out the right wingtip). Because lift and drag are defined with respect to the velocity vector, they too rotate by the same amount. The drag now assumes a downward component and the lift assumes an aftward component with respect to the initial coordinate system. The downward drag component is small and usually ignored, but the aftward lift component can be summed along the wing at each station to obtain the induced drag. From potential flow theory, this results in Eq. (3.17).

$$C_{d_i} = \frac{{C_l}^2}{\pi A_r}(1-\delta) = \frac{{C_l}^2}{\pi \epsilon A_r} \tag{3.17}$$

where A_r is the aspect ratio, δ is a correction factor for non-elliptical lift distribution, and ϵ is the span efficiency factor defined as

$$\epsilon = \frac{1}{(1-\delta)} \tag{3.18}$$

ϵ should not be confused with Oswald efficiency, e, as the Oswald efficiency factor incorporates the quadratic dependence on parasitic drag as shown in Eqs. (3.19) and (3.20) below.

$$C_{d_w} = C_{d_{p0}} + \frac{{C_l}^2}{\pi e A_r} \tag{3.19}$$

$$e = \frac{1}{(1-\delta) + k\pi A_r} \tag{3.20}$$

Eqs. (3.19) and (3.20) will not be used for calculations in this report.

Although Eq. (3.17) is mathematically correct for potential flow theory, the induced drag of the wing can also be computed empirically using Eq (3.21) presented in Abbot and Doenhoff (1949),

$$C_{d_i} = \frac{{C_l}^2}{\pi A_r \epsilon} + C_l \gamma \frac{a_e \pi}{180} \nu + \omega \left(\epsilon \frac{a_e \pi}{180}\right)^2 \tag{3.21}$$

where γ is the wing washout in radians, and ϵ, ν and ω are empirical constants determined as functions of aspect ratio and taper ratio. The values of these coefficients for the Genii aircraft are 0.98, .0012, and 0.0037, respectively. As evidenced by the low values of ν and ω, the first term in Eq. (3.21) dominates for the unswept wing of the Genii aircraft.

For wing-total properties, the section lift coefficient, c_l must be corrected for spanwise effects. The following technique is used to determine the relationship between section lift coefficient c_l, and the wing lift coefficient C_l. The lift-slope of an airfoil in the linear range is expressed using the methodology described by Abbott and Doenhoff (1949)

$$\frac{dC_L}{d\alpha_r} = f \frac{a_e}{1 + \left(53.3\left(\frac{a_e}{180 A_r}\right)\right)} \tag{3.22}$$

where f is a correction factor equal to 0.997 for Genii. The effective lift slope in radians, a_e, was expressed by Eq. (3.8). Within the linear range, the lift coefficients are then

$$C_l = \frac{dC_l}{d\alpha_r}(\alpha_r + \alpha_{r0}) \tag{3.23}$$

$$c_l = a_0(\alpha_r + \alpha_{r0}) \tag{3.24}$$

where α_{r0} is the zero lift angle, -0.064 (-3.64 º) for the Genii aircraft as described above. α_{r0} is assumed to be the same for the infinite and finite wings. The section lift coefficient required to achieve a given finite wing lift coefficient can be determined by combining Eqs. (3.23) and (3.24)

$$c_l = \frac{a_0}{\frac{dC_l}{d\alpha_r}} C_l \tag{3.25}$$

The term $\frac{a_0}{\frac{dC_l}{d\alpha_r}}$ can be defined as a correction factor for simple calculations.

$$k_{2d} = \frac{a_0}{\frac{dC_l}{d\alpha_r}} \tag{3.26}$$

This term will also appear in the calculation of trim drag but for the horizontal tail's geometry rather than the wing's.

It is useful to know the angle of attack of the wing at the root for a given C_l to determining stall or to find the angle of attack of other components. Abbott and Doenhoff (1949) report a method for determining this angle

$$\alpha_{root} = \frac{d\alpha_r}{dC_l}\alpha_r + \alpha_{r0} + \mathrm{J}\,\gamma \tag{3.27}$$

where J is a geometry dependent coefficient equal to -0.42 for the Genii aircraft. The wing's root is set at a 0.070 (4º) incidence to the aircraft fuselage and horizontal tail.

The final term in Eq. (3.3), $C_{d_{mis}}$, accounts for the miscellaneous drag components resulting from interference effects as wells as aileron gaps. It is not uncommon to include an interference factor to account for the additional drag resulting from the interaction of wing and fuselage. Jacobs and

Ward (1935) studied this effect. For geometry similar to the wing-fuselage configuration of the Genii aircraft, inappreciable drag was seen over the drag coefficient obtained by summing the fuselage and wing independently. This is perhaps caused by the additional wetted surface area resulting from the analysis of two separate bodies vis-à-vis a combined body where these areas overlap.

An additional drag component is conserved to attempt to account for the gaps and chamfer of the aileron cove. Horner (1985) presents a drag analysis of an BF-109 fighter aircraft and incudes the assumed drag coefficients and reference areas for the aileron gaps, hinges, and external mass balances (assumed to approximate the control horns of the Genii aircraft). $C_{d_{mis}}$ is then found as

$$C_{d_{mis}} = \frac{1}{S}\left(C_{d_{gap}}S_{gap} + C_{d_{hinge}}S_h + C_{d_{balance}}S_b\right) \tag{3.28}$$

where $C_{d_{gap}}$, $C_{d_{hinge}}$, and $C_{d_{balance}}$ are the drag coefficients as reported by Horner (1985), given as 0.025, 0.5, and 0.3 respectively. S_{gap}, S_h, and S_b are the reference areas for the Genii aircraft, 0.04 m^2, 0.001 m^2, and 0.003 m^2, respectively.

3.2.2: Results Obtained with Vortex-Lattice Method

Numerical simulations are performed to validate the simplified techniques for calculation of C_l and C_{d_i} using the Athena Vortex Lattice (AVL) (Athena Vortex Lattice, 2014) program developed by Drela and Youngren. AVL is a vortex lattice solver and distributes panels along the spanwise and chordwise directions of the wing and stabilizers. A horseshoe vortex is applied at the ¼ chord of each panel with trailing legs along the panel sides. A Newman boundary condition (zero normal velocity) is applied to collocation points located at the spanwise center of the ¾ chord of each panel to form a fully defined system of linear equations and unknowns. Solving yields the vortex

intensity at each panel, which by means of the Kutta-Joukowski theorem yields the lift component for each panel. AVL is an inviscid solver and can predict lift and induced drag but not parasitic drag resulting from viscous effects. Panels in the chordwise direction are distributed along the airfoil camber line to account for nonzero camber, however thickness effects are not modeled.

Wing lift distribution can be produced by summing the panel lift components in the chordwise direction to produce a total lift force at each spanwise station. The overall shape of the lift distribution is a function of wing taper, twist, sweep, and dihedral. Results for Genii's wing are shown for c_l in Fig. (3.6). For this figure, the lift coefficient has been multiplied by the local chord and normalized by the center section lift coefficient. This produces a plot more indicative of the lift distribution, because the local chord varies due to taper.

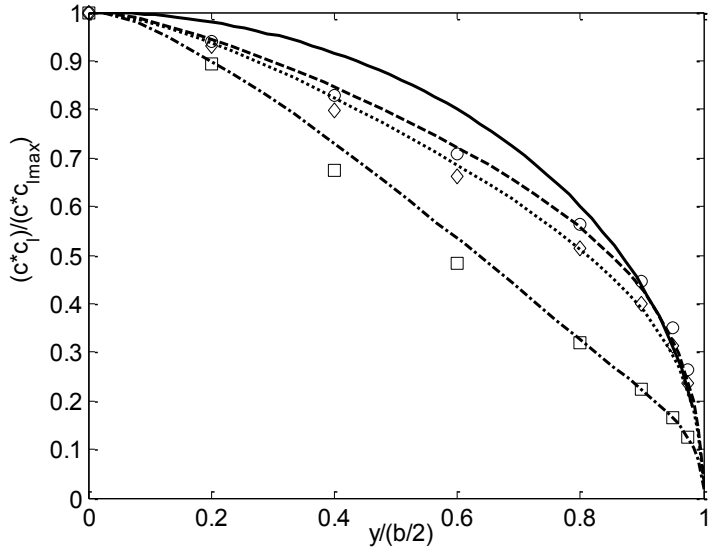

Figure 0.6: *Lift distribution for the wing of the Genii aircraft. Dashed line: AVL calculation at C_l = 1, Dotted line: AVL calculation at C_l = 0.8, Dot-dash line: AVL calculation at C_l = 0.2, Circles: Eq. (3.7) at C_l = 1.0, Dimonds: Eq. (3.7) at C_l = 0.8, Squares: Eq. (3.7) at C_l = 0.2, Solid line: elliptical distribution.*

For reference, an elliptical distribution is also shown.

Lift distribution becomes more elliptical with increasing angle of attack. Results from AVL are shown as lines while results from Abbot and Doenhoff (1959) via Eq. (3.7) are shown as points.

The C_l polar is also constructed from AVL simulations and compared with Eq. (3.25) used with the section lift polar from Selig et al. (1995) for R_e = 304300. Cases are ran in AVL from α_{mac} = -5 to 10 degrees, where α_{mac} is the angle of attack at the spanwise station of the mean aerodynamic chord; $\alpha_{mac} = \alpha_{root} - 1.38º = \alpha_{tip} + 1.62º$. The results for both approaches are shown in Fig. (3.7A). The techniques show good agreement with a difference less than 0.05 C_l for α_{mac} between -4.5º and 5.5º. For α_{mac} larger than 5.5º nonlinear effects cause the methods to diverge. A difference of C_l = 0.2 exists at α_{mac} = 9.4 º, when the root airfoil begins to stall.

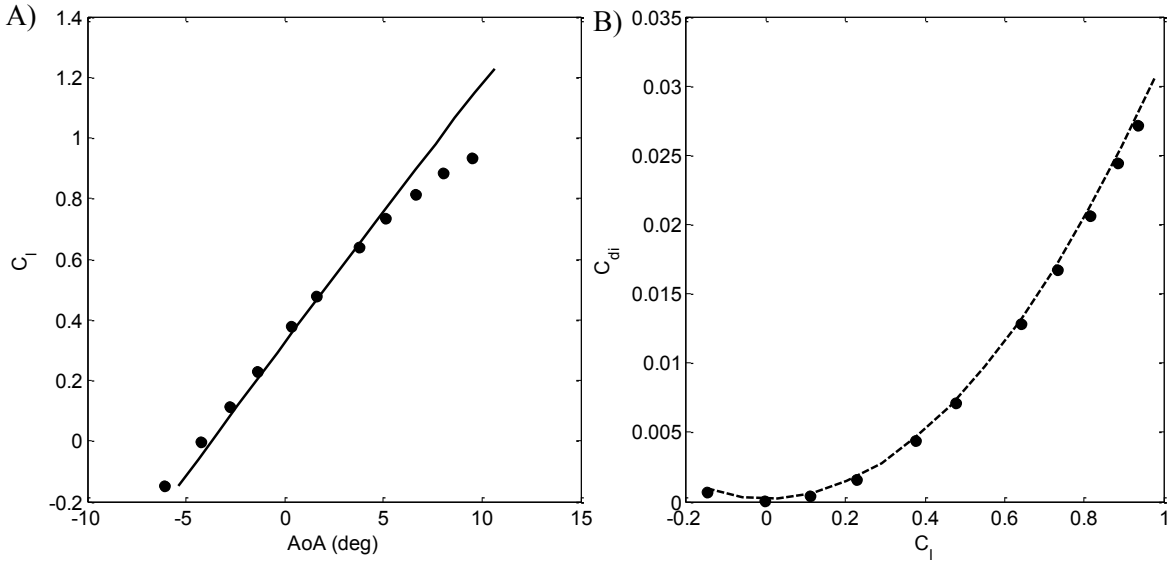

Figure 0.7: *A) Lift coefficient with respect to angle of attack for the Genii aircraft at R_e = 304300. Solid line: AVL calcuations, Circles: Eq. (3.25). B) Induced drag coefficient with respect to lift coefficient. Dashed line: AVL calcualtions, Circles: Eq. (3.21).*

A similar comparison is shown in Fig. (3.7B) for the prediction of C_{d_i}. AVL calculations are shown as a dashed line while Eq. (3.21) is shown as circles. The difference between approaches is less than $\Delta C_{d_i} = 0.001$ over a C_l range of -0.15 to 1.

3.2.3: Landing Gear

The landing gear is treated simply using drag coefficients from literature such that,

$$C_{d_g} = I_{f_g}\left(C_{d_{tire}}\frac{\sum S_{tires}}{S}\right)+C_{d_{strut}}\frac{\sum S_{struts}}{S} \tag{3.29}$$

where $C_{d_{tire}}$ is the drag coefficient of a tire, $C_{d_{strut}}$ is the drag coefficient of the struts, $\sum S_{tyres}$ is the summation of the cross sectional areas of the tires, $\sum S_{struts}$ is the summation of the cross section areas of the struts, and I_{f_g} is an interference factor to account for the tire-strut joint.

Lindsy (1937) published the drag coefficient of a cylinder perpendicular to the airstream with respect to R_e. The landing gear struts are approximated as cylinders and their drag coefficient is taken from Lindsey (1937). From Lindsey's work, $C_{d_{strut}}$ is assumed to equal a constant 1.2. The total cross sectional area of struts for the Genii aircraft is approximately 167 cm^2.

Herrnstein and Bierma (1934) report wind tunnel tests of various configurations of aircraft tire, strut, and fairing. Although the data is presented in dimensional form, the drag coefficient of an aircraft tire similar in aspect ratio to Genii's is determined to be 0.253. Additionally, the interference between an unshielded strut and tire at the joining angle of 45º is found to add an additional 36% interference drag to the tire. The total cross sectional area of tires for the Genii aircraft is approximately 0.017 m^2.

3.2.4: Cameras

Four GoPro® compact cameras of various models are utilized for in flight recording from the Genii aircraft. The cameras are typically mounted, one each, on the vertical stabilizer, bottom fuselage, right wing, and upper fuselage. These cameras help judge flight characteristics and are useful for

assessing the cause of mishaps. Surprisingly, the presence of these cameras constitutes a large portion of the aircraft's drag and uncertainty of their exact contribution is a consequential component of the total error. At this time, no literature exists reporting the drag coefficient of a Gopro® camera and its mount at different yaw angles. Measurement of these values would be surprisingly involved due to the complex interaction of the camera and the boundary layer of the object to which it is affixed. For the purposes of this report, the drag of the cameras was approximated as

$$C_{d_c} = 1.2\frac{\sum S_c}{S} \tag{3.30}$$

where S_c is the frontal area of a single camera. The drag coefficient 1.2 approximates a cube at low R_e. All cameras are not placed normal to the freestream and the actual drag coefficient of the camera alone is probably less than 1.2 due to slight fairing of the camera's housing. This over prediction is assumed to partially compensate for neglecting the effect of the camera mounts in Eq. (3.30).

3.2.5: Stopped Propeller

In the case of glide, and in the calculation of glide ratio, the drag of the stopped propeller is accounted for with the approximations in Raymer.

$$C_{d_p} = 0.8\frac{S_p}{S} \tag{3.31}$$

where S_p is the total frontal area of the propeller blades, approximately, 0.026m^2.

3.2.6: Fuselage

The fuselage was considered a non-lifting body for performance predictions. Lift performance of a streamline airship is given in Horner (1985). For $\alpha_d < 12°$ the lift slope of a streamline body described to be, at most, 0.1719 per radian, roughly 30 times smaller than the lift slope of the wing.

The profile drag coefficient of the fuselage is found using the empirical technique presented in Raymer (2006) for low Mach number turbulent flow.

$$C_{d_f} = C_f F_f \frac{S_{f_{wet}}}{S} \tag{3.32}$$

$$C_f = \frac{0.455}{\log_{10}\left(\min(R_f, R_{f_{coff}})\right)^{2.58}} \tag{3.33}$$

$$F_f = 1 + \frac{60{d_f}^3}{{l_f}^3} + \frac{l_f}{400 d_f} \tag{3.34}$$

$$d_f = \sqrt{\frac{4}{\pi} A_{cx_{max}}} \tag{3.35}$$

$$R_{f_{coff}} = 38.21\left(\frac{L_f}{k}\right)^{1.053} \tag{3.36}$$

where C_f is the flat-plate skin friction coefficient, F_f is the fuselage form factor, and $S_{f_{wet}}$ is the wetted surface area of the fuselage, 1.73 m^2. R_f is the reynolds number based off the length of the fuselage, $R_{f_{coff}}$ is a cut-off equivalent reynolds number, d_f is the fuselage effective diameter, and l_f is the ratio of fuselage length to effective diameter. L_f is the fuselage length, 1.87 m, $A_{cx_{max}}$ is

the maximum cross-sectional area of the fuselage, 1.25 m^2, and k is a skin roughness, assumed to be 1.015 x 10^{-5} m. The fuselage is assumed to be totally submersed in the propwash. The additional drag from this effect is accounted for by an increase in dynamic pressure found by multiplying q by a dynamic pressure ratio, η described in Raymer (2006)

$$\eta = 0.9\left(1 + \frac{T}{qA_p}\right) \tag{3.37}$$

where A_p is the area of the propeller disk. For some flight regimes, such as maximum climb rate, thrust, T, is known, however for many cases, like cruising flight, the thrust is implicitly related to the drag. For these cases, the thrust is initially estimated and the mathematical model is iterated, equating thrust to drag after each iteration. Convergence is obtained quickly, usually within four iterations.

3.2.7: Duct

The drag of the inlet duct for air to the fuel cell is roughly approximated from Raymer (2006) as

$$C_{d_d} \cong 1.2\frac{S_d}{S} \tag{3.38}$$

where S_d is the duct cross-sectional area, 0.01 m^2.

3.2.8: Empennage

The drag resulting from the tailboom, vertical and horizontal stabilizers, and any interference effects is the empennage drag given as

$$C_{d_e} = C_{d_{tb}}\frac{S_{tb}}{S} + I_{f_e}\left(C_{d_v}\frac{S_v}{S} + C_{d_h}\frac{S_h}{S}\right) \tag{3.39}$$

where $C_{d_{tb}}$ is the tailboom's drag coefficient, I_{f_e} is a 5% interference factor as recommended by Raymer (2006), C_{d_v} is the vertical stabilizer's drag coefficient, C_{d_h} is the horizontal stabilizer's drag coefficient, S_v is the vertical tail area and S_h is the horizontal tail area. The skin friction coefficient of the tailboom is estimated as $C_{d_{tb}}$ = 0.0043 and its surface area is S_{tb} = 0.17 meters.

The drag of the stabilizers is broken into profile drag resulting from their effective angle of attack, induced drag resulting from any upforce or downforce produced by the surface, and an additional profile drag component resulting from the displacement of the control surface required to maintain trim. The combination of the induced drag and the drag resulting from control surface displacement is often referred to as trim drag.

The vertical stabilizer experiences trim drag when balancing the adverse yaw caused by aileron trim. Aileron trim is required to counter the torque of the motor. For the Genii aircraft, this effect is sufficiently small that trim drag of the vertical stabilizer is ignored. The drag of the vertical stabilizer is therefore estimated as the profile drag of its NACA 0012 section. Sideslip of the aircraft is not considered in this report so the profile drag is approximated as the zero lift drag coefficient as computed by Xfoil at R_e = 700000, C_{d_v} = 0.00579.

The horizontal drag coefficient is comprised of the components discussed above

$$C_{d_h} = C_{d_{hp}} + \frac{{C_{l_h}}^2}{\pi 0.7 A_{r_h}} + \frac{dC_{d_h}}{d\xi}\xi \tag{3.40}$$

where $C_{d_{hp}}$ is the profile drag coefficient of the NACA 0012 section, C_{l_h} is the total lift coefficient of the horizontal stabilizer, A_{r_h} is the aspect ratio of the horizontal stabilizer, and ξ is the displacement of the elevator. The span efficiency of the horizontal is approximated as 0.7. For

Genii the induced drag component is very small, but its inclusion is simple. The profile drag of the horizontal was determined using Xfoil for R_e = 700000 and shown in Eq. (3.41). The effect of variable R_e is not accounted for.

$$C_{d_{hp}} \cong 0.00579 + 0.00008C_{l_h} + 0.00996{C_{l_h}}^2 \tag{3.41}$$

C_{l_h} and ξ are determined from the requirement that there is zero net moment about the CG of the aircraft in unacclerated flight. This is expressed by Eq. (3.42)

$$SM_{ac}\left(C_{m_w} + \frac{dC_{m_f}}{d\alpha_r}\alpha_r\right) + \left(A_{c_w} - x_{cg} - y_{cg}\alpha_r\right)SC_l = \left(A_{c_h} - x_{cg}\right)\eta S_h k_{2d}\left(c_{l_h} + \frac{dc_{l_h}}{d\xi}\xi\right) \tag{3.42}$$

where C_{m_w} is the moment coefficient of the wing, C_{m_f} is the moment coefficient of the fuselage, A_{c_w} is the location of the wing's aerodynamic center, x_{cg} is the longitudinal location of the vehicle's CG, y_{cg} is the vertical distance between the wing and the cg, and A_{c_h} is the location of the horizontal stabilizer's aerodynamic center. k_{2d} is the correction factor for the finite span horizontal tail calculated in the same manner as for the wing expressed by Eq. (3.26) and taken as 0.9 for the horizontal stabilizer. α_r in Eq. (3.42) is the angle of attack of the fuselage and horizontal tail, and its relationship to C_l is given by Eq. (3.27) with a four degree bias for the wing's incidence.

C_{m_w} is not reported by Selig et al. (1995) so its value is approximated using Xfoil calculations for R_e = 700000

$$C_{m_w} \cong -0.0818 + 0.01094C_l \tag{3.43}$$

A method of calculating $\frac{dC_{m_f}}{d\alpha}$ is reported by Raymer (2006) from the work of Gilruth and White (1940).

$$\frac{dC_{m_f}}{d\alpha_r} = \frac{K_f {W_f}^2 L_f}{S c_{mac}} \tag{3.44}$$

where K_f is an empirical coefficient equal to 2.57 for Genii if the derivative is expressed per radian, W_f is the fuselage width, and L_f is the length of the fuselage.

c_{l_h} is a function of the wing's C_l with provisions for the downwash experienced from the wing and propeller

$$c_{l_h} = \frac{dc_{l_h}}{d\alpha_r}\alpha_e \tag{3.45}$$

The value $\frac{dc_{l_h}}{d\alpha}$ was taken as 0.1175 from Xfoil calculations of an NACA 0012 at R_e = 700000.

where α_e is the effective angle of attack

$$\alpha_e = \alpha - \frac{d\varepsilon_p}{d\alpha}\alpha - \frac{d\varepsilon_w}{d\alpha}\frac{d\alpha}{dC_l}C_l \tag{3.46}$$

where ε_w is the downwash angle on the horizontal tail due to the wing and ε_p is the downwash angle on the horizontal tail due to the propeller. Raymer (2006) presents values of $\frac{d\varepsilon_w}{d\alpha}$ as a function of geometry from those originally reported by Silverstein and Katzoff, (1939). $\frac{d\varepsilon_p}{d\alpha}$ = 0.4 for the Genii aircraft. Raymer (2006) also reports values of $\frac{d\varepsilon_p}{d\alpha}$ from data presented in Seckel (1964) via Eq. (3.47).

$$\frac{d\varepsilon_p}{d\alpha} = K_1 + K_2 N_b \frac{\partial C_{n_b}}{\partial \alpha}\left(\frac{\partial \alpha_p}{\partial \alpha}\right) \tag{3.47}$$

where K_1 and K_2 are empirical constants equal to 0.20 and 0.25, respectively, for the Genii aircraft, $\frac{\partial C_{n_b}}{\partial \alpha}$ is approximately 0.04 from empirical data when the derivative is expressed per radian, and $\frac{\partial \alpha_p}{\partial \alpha}$ is assumed to be unity due to the large separation of the propeller forward of the wing.

Equations (3.45) and (3.46) can be used to determine c_h for use in Eqn. (3.44), however $\frac{dC_{d_h}}{d\xi}$ and ξ must be determined to use this equation to obtain the total empennage drag.

The lift addition to the horizontal tail due to the deflection of the elevator is approximated as constant for small elevator deflections. Xfoil computations at R_e = 700000 indicate that $\frac{dC_{l_h}}{d\xi}$ is approximately equal to -0.09 per degree. $\frac{dC_{l_h}}{d\xi}$ is shown for various angles of attack and two elevator deflections, 5 deg and 10 deg trailing edge up in Fig. (3.8).

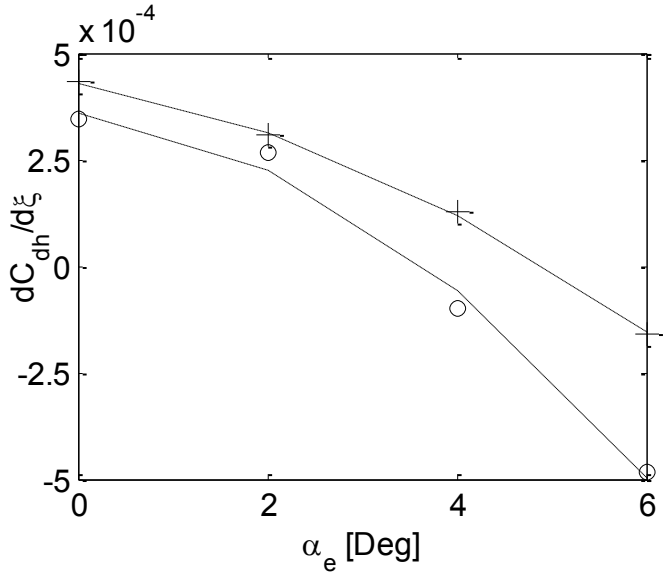

Figure 0.8: *Change in section lift coefficient with respect to elevator deflection for different effective angles of attack as computed by Xfoil. R_e = 700000, Circles: ξ = 5 º trailing edge up, Crosses: ξ = 10º trialing edge up.*

$\frac{dC_{d_h}}{d\xi}$ is dependent on both elevator deflection and angle of attack. $\frac{dC_{d_h}}{d\xi}$ is shown for several angles of attack for the 5º and 10º trailing edge up conditions in Fig. (3.9). A simple interpolation

approximation similar to that applied to the wing for R_e is applied to determine $\frac{dC_{d_h}}{d\xi}$ at a given ξ. This is shown by Eq. (3.48)

$$\frac{dC_{d_h}}{d\xi} = \frac{dC_{d_{h4}}}{d\xi} + \left(\frac{dC_{d_{h8}}}{d\xi} - \frac{dC_{d_{h4}}}{d\xi}\right)\frac{\xi - 4}{8 - 4} \tag{3.48}$$

where

$$\frac{dC_{d_{h8}}}{d\xi} \cong 0.00043030 + 0.00003835\alpha_e - 0.00000988{\alpha_e}^2 \tag{3.49}$$

$$\frac{dC_{d_{h4}}}{d\xi} \cong 0.00035950 + 0.00002925\alpha_e - 0.00001888{\alpha_e}^2 \tag{3.50}$$

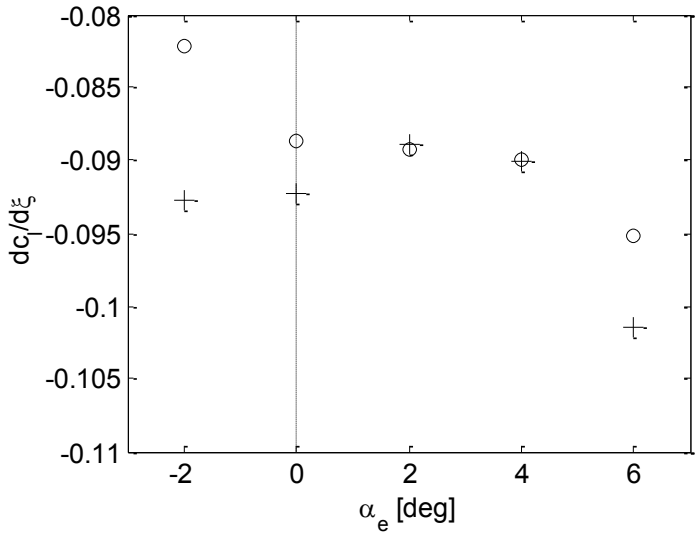

Figure 0.9: *Change in profile drag coefficient with respect to elevator deflection for different effective angles of attack for the horizontal tail. Values computed with Xfoil at R_e = 700000. Circles: ξ = 5 º trailing edge up, Crosses: ξ = 10º trialing edge up.*

The trim drag constitutes a small fraction of the total aircraft drag for Genii, however trim drag will increase if the CG is moved forward. A plot of the required trailing edge up elevator deflection for trim of the Genii aircraft is shown in Fig. (3.10).

The 3.3 degrees trailing edge up minimum deflection required for trim at approximate cruise speeds is a design fault. The horizontal stabilizer incidence should have been set to drive this value to zero. Although the trimmed deflection was never measured, this is consistent with experience in flight testing, where slight elevator up trim was required.

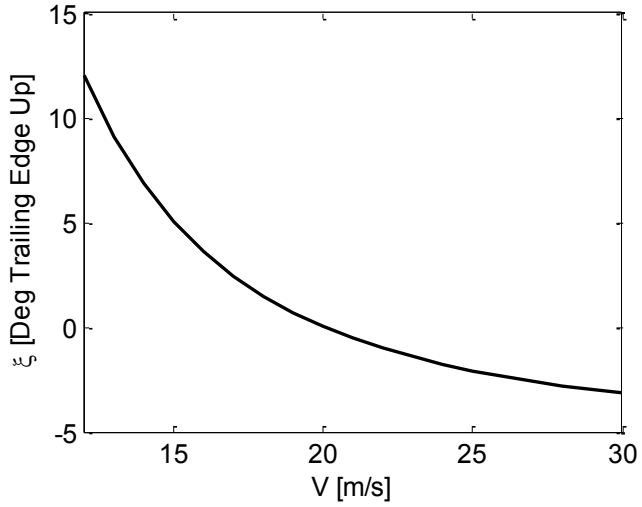

Figure 0.10: *Elevator deflection required for trim with respect to airspeed.*

3.2.9: Total Drag

The calculated drag of each component of the Genii aircraft from Eq. (3.1) is plotted against airspeed for the power-on configuration at a mass of 32.8 kg in Fig. (3.11). The wing curve represents the profile drag.

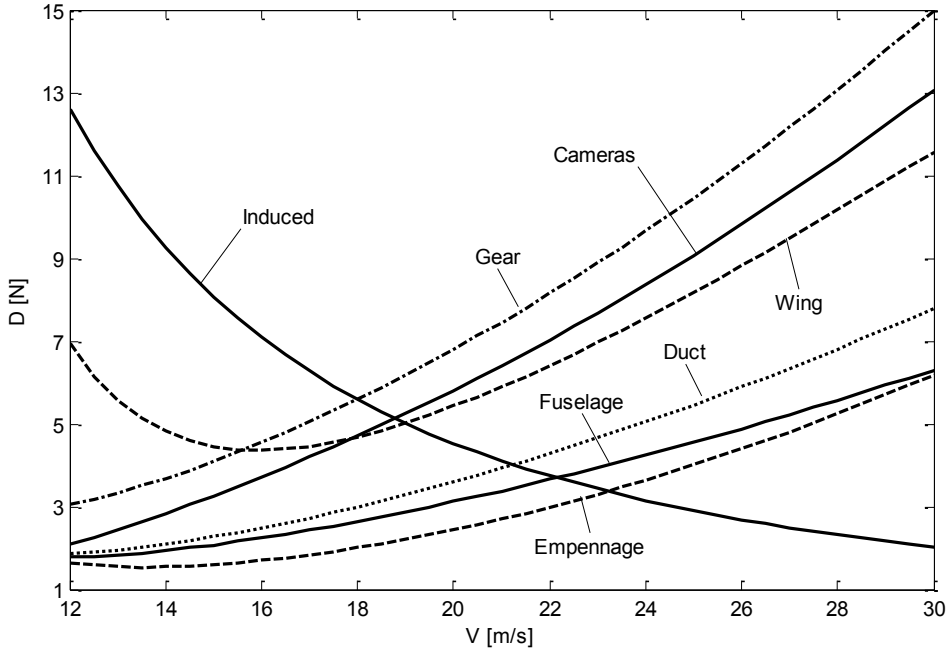

Figure 0.11: *Drag of indicated aircraft components with respect to airspeed. M = 32.8 kg "Wing" indicates all wing drag components less induced drag.*

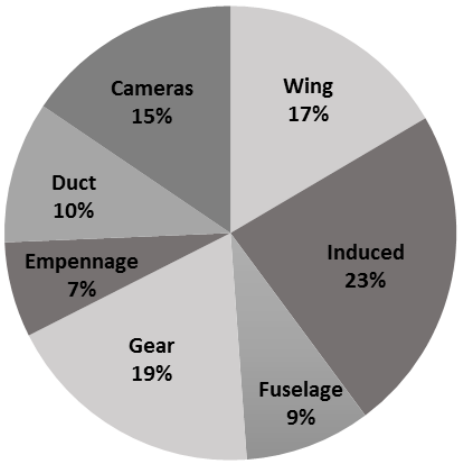

Figure 0.12 *Component drag contribution at M = 32.8 Kg, V = 17*

At airspeeds greater than 18 m/s, the landing gear is the largest contributor to the total drag, followed by the cameras and the profile drag of the wing. The duct, fuselage, and empennage contribute similarly and are each roughly half of the drag of the landing gear. A percentage breakdown of each component at V = 17.0 $^{m}/_{s}$ is shown in (Fig. 3.12).

The total drag of the 32.8 kg configuration at $\rho = 1.2\ {}^{kg}/_{m^3}$ is shown in Fig. (3.13A). The minimum drag is 27.4 N and occurs at an airspeed of 15.0 ${}^{m}/_{s}$. Fig. (3.13B) shows the total drag coefficient with respect to the wing area of the Genii aircraft as a solid line and the total drag coefficient less the induced drag coefficient as a dashed line. Also shown are two other common performance metrics, the equivalent skin friction coefficient and the flat plate area given as, respectively

$$C_{esf} = \frac{S}{S_{wet}} C_d \tag{3.51}$$

$$S_{fp} = SC_d \tag{3.52}$$

where S_{wet} is the total wetted surface area, approximatly equal to 5.82 m^2 for the Genii aircraft. The minium C_d of 0.03 is very similar to many light aircraft such as the Cesena 172.

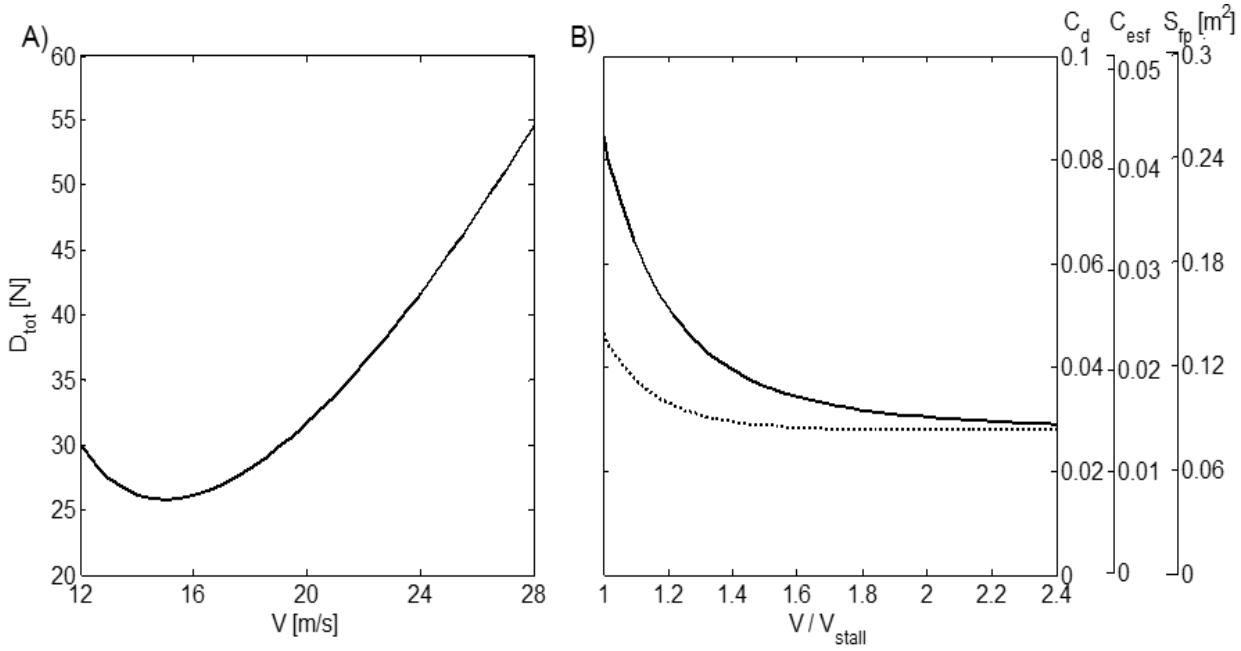

Figure 0.13: *A) Total Drag, M = 32.8 B) Total drag coefficient, equivalent skin friction coefficient, and equivalent flat plate area, with respect to normalized airspeed. Solid line: Total drag, Dotted line: Total drag less induced drag.*

3.3: Aircraft Performance

The preceding section outlined the technique used to determine the drag performance of the Genii aircraft. This drag model, when coupled with the aircraft's propeller model as discussed in Chapter 4, allows the various performance metrics mentioned at the beginning of this Chapter to be computed. Because flight tests were performed as part of the aircraft's development, the mass of the aircraft varies by several kilograms between flights. Of primary interest are flights ten through fourteen with respective aircraft masses of 22.6 kg, 25.3 kg, 26.3 kg, 30.3 kg, and 32.8 kg. While the performance of the aircraft is different for each mass, the techniques used to calculate each performance metric are the same. As such, only the 32.8 kg configuration will be displayed in this section's figures for simplicity.

3.3.1: Stall

The aircraft's stall speed is not directly compared to flight testing, however its prediction is useful for nondimensionalizing vehicle performance in Chapter 5. Stall is not a discrete event, but progresses in severity from onset to full-wing stall. In its section form, stall can be found to occur at a critical angle of attack, however for full-wing dynamic events, spanwise flow, propwash, and aircraft pitch, roll, and yaw rates all effect the onset and propagation of stall.

For the simplified use herein, Genii's stall speed is defined as the airspeed at which the root airfoil section reaches its section stall angle of attack. From the wind tunnel tests of Selig et al. (1995), the section stall angle of attack and c_l of the SD 7037 airfoil at Re = 304300 are approximately 11 degrees and 1.25, respectively. The airspeed at which the angle of attack of the root reaches 11 degrees can easily be found by substituting the lift equation into Eq. (3.27) such that

$$V_{stall} = \sqrt{\frac{2Mg}{\rho S \frac{d\alpha_r}{dC_l}\left(11\frac{\pi}{180} - \alpha r_0 - J\gamma\right)}} \tag{3.53}$$

The stall speed of the Genii aircraft is shown with respect to mass in Fig (3.14). Because V_{stall} was defined as the onset of root stall, the minimum airspeed of the aircraft will be slightly below this value. Despite a reduction in lift inboard due to the onset of stall, c_l continues to increase outboard until those stations stall as well. The absolute maximum C_l will therefore occur slightly after the onset of root stall. The difference in airspeed between the onset of stall and the airspeed of maximum C_l is small for Genii, in part due to the taper ratio which concentrates the lift inboard. Investigation of the wing's lift distribution suggests that this difference is less than 0.4 m/s.

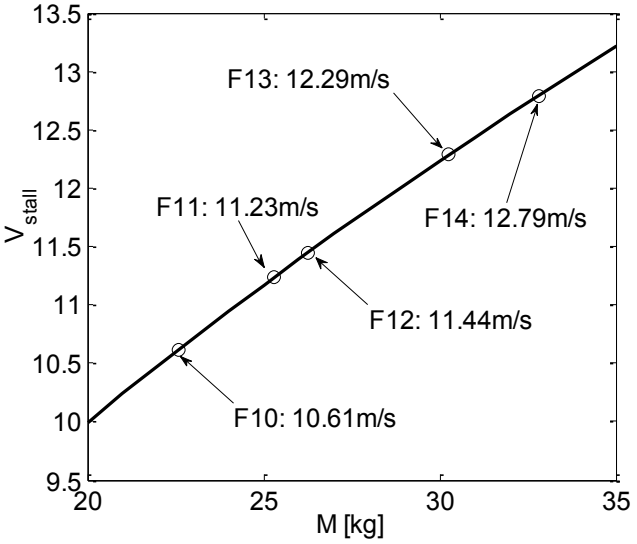

Figure 0.14: *Stall speed of the Genii aircraft with respect to mass. Points indicate the flight 10 through 14 configurations.*

3.3.2: Maximum Airspeed

The maximum airspeed in level flight can be determined as the airspeed for which the aircraft's drag and maximum thrust are identical. The propulsion system of the Genii aircraft operates such that the maximum speed of the motor is nearly the same for every flight condition with only small dependence on the applied torque. This maximum speed is roughly 4150 rpm. The propeller's performance is analyzed in Chapter 4 and the relationship between the propeller's thrust coefficient and advance ratio is determined. As such, the propeller's thrust can be computed for a given

airspeed and rpm. Figure (3.15) depicts the drag curve of the 32.8 kg aircraft and the thrust curves of the APC 26X15E propeller at various rpm. The maximum thrust obtainable occurs at the propulsion system's limit of 4150 rpm, the curve for which is included as a decreasing solid line. The point at which the aircraft's drag and maximum thrust curves intersect equates the drag and thrust equations and is the maximum airspeed. Because the drag terms resulting from the aircraft's lifting requirement are small at high speed, logically, the maximum level flight speed has only small dependence on aircraft mass. The maximum level flight speeds are 25.87 m/s, 25.89 m/s, 25.91 m/s, 25.91 m/s, and 25.91 m/s for the 32.8 kg, 30.3 kg, 26.3 kg, 25.3 kg, and 22.6 kg configurations, respectively. Formulations for post-stall drag are not included in the mathematical model so drag values shown in Fig (3.15) less than stall are unrealistically low.

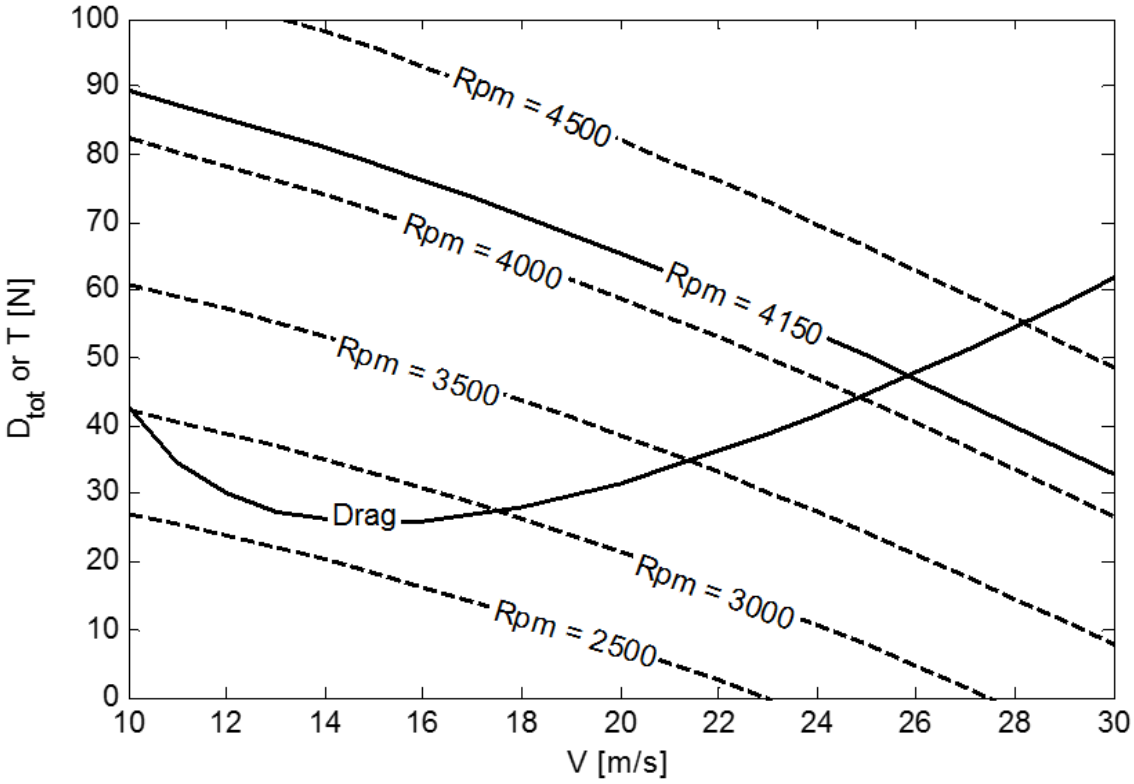

Figure 0.15: *Aircraft drag and thrust with respect to airspeed. Dashed lines: constant motor rpm. Solid decreasing line: thrust at maximum motor rpm.*

3.3.3: Minimum Power for Level Flight

Both the aircraft's drag power and propulsive power can be easily calculated as the product of the aircrafts drag or thrust with the airspeed.

$$P_{tot} = VD_{tot} \tag{3.54}$$

$$P_p = VT \tag{3.55}$$

The drag and propulsive power curves of the 32.8 kg configuration of the Genii aircraft are shown in Fig. (3.16). As with the aircraft's thrust, the maximum obtainable propulsive power occurs at the maximum motor speed of 4150 rpm. Additionally, drag power below stall is unrealistically low due to the omission of post-stall drag and limited C_l in the mathematical model.

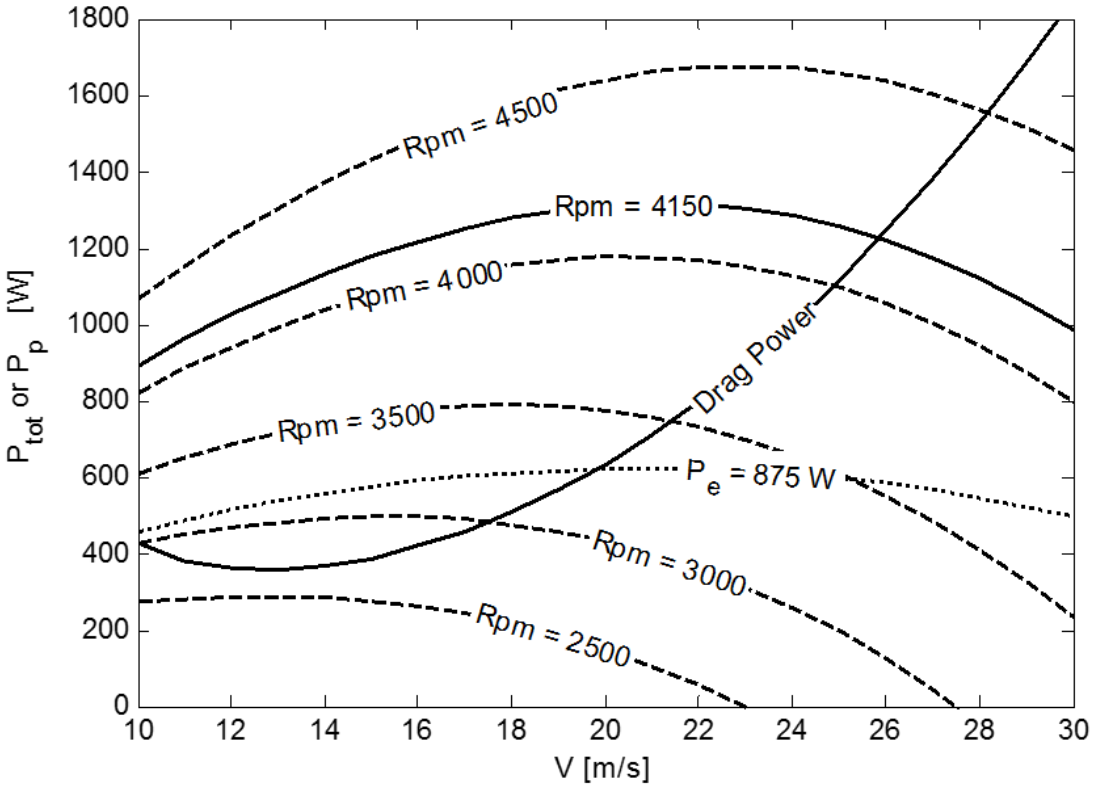

Figure 0.16: *Aircraft drag power with respect to airspeed. Dashed lines: constant motor rpm. Dotted line: constant 875 W electrical power.*

The aircraft's drag power will be used to determine several parameters of interest. The easiest is the minimum propulsive power required for level flight. The minim drag power is 351 W, 316 W, 256 W, 243 W, 205 W for the 32.8 kg, 30.3 kg, 26.3 kg, 25.3 kg, and 22.6 kg configurations, respectively. As per the aircraft requirements, Genii must be capable of flight at less than 875 Watts electrical power. Under a simplistic assumption of a constant 10% loss through motor, esc, and gearbox, the performance of the propeller is plotted as the dotted line in Fig. (3.17). This indicates that a flight envelope between stall and 18 m/s is available under fuel cell power alone. However, as seen in subsection 3.3.4, climb performance is substantially reduced.

By the definition of power, the airspeed at which minimum drag power occurs is the airspeed which should be flown to minimize energy consumption and maximize time aloft. These airspeeds are 12.7 m/s, 12.2 m/s, 11.4 m/s, 11.2 m/s and 10.6 m/s for the 32.8 kg, 30.3 kg, 26.3 kg, 25.3 kg, and 22.6 kg configurations, respectively.

The reader will notice that for Genii, these airspeeds are slightly less than the stall speeds of the aircraft! In reality, the large drag increase associated with the onset of stall will shift these speeds slightly faster than predicted by the model. Even so, for manned aircraft, it is abnormal for these airspeeds to be so close to stall. It is suspected that abnormal combination of Genii's efficient wing, with its low wing loading and sailplane airfoil designed for high L/D operation, and a comparatively dirty airframe result in driving this number toward the extremum of stall. For safety in actual flight testing, the desired cruise airspeed for the 32.8 kg aircraft was set at 17 m/s, roughly 1.3 times stall rather than the airspeed for minimum required power.

3.3.4: Rate of Climb

Due to dynamic flight conditions and pilot ability, it is difficult to hold the Genii aircraft at zero rate of climb (or sink). As such the mathematical model must be corrected for steady rate of climb, otherwise test results would be very limited. This is done by adding an apparent power to the drag power to account for the aircraft's rate change in altitude. Equation (2.10) can be rearranged to find the propulsive power required at a given rate of climb.

$$P_p = P_d + WR_{oc} \tag{3.56}$$

Equation (2.10) itself calculates the steady rate of climb given a particular excess power, $P_p - P_d$. Therefore, the maximum rate of climb is simply the difference between the drag power curve and propulsive power curve in Fig. (3.16) divided by the weight of the aircraft. The maximum rate of climb of the Genii aircraft at 32.8 kg is given in Fig. (3.17) for both battery and fuel cell operation.

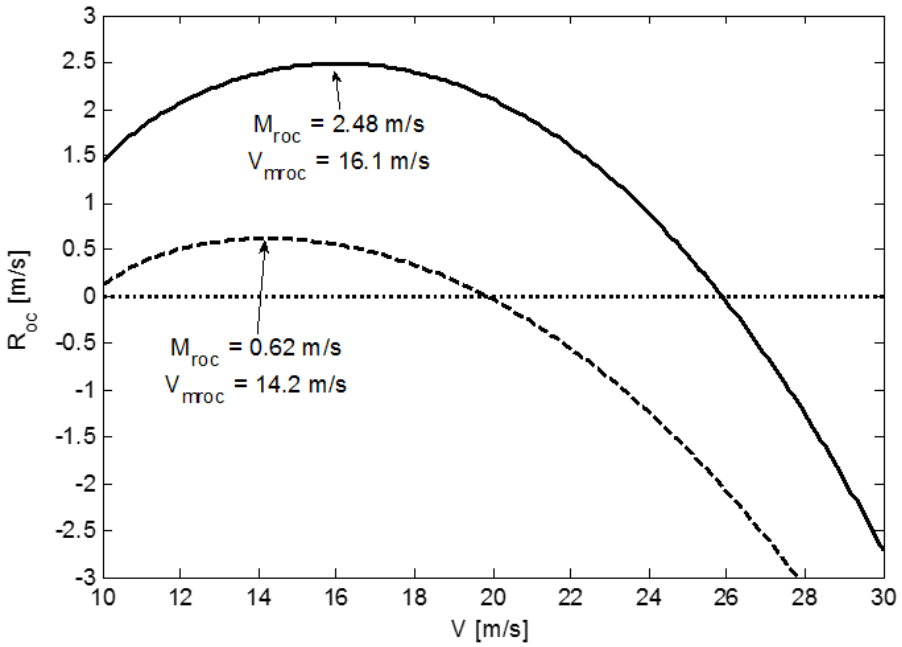

Figure 0.17: *Maximum rate of climb for the 32.8 kg configuration. Solid line: under battery power (rpm = 4150), Dashed line: under fuel cell power (P_e = 875 W).*

The maximum rates of climb are 2.48 m/s, 2.77 m/s, 3.33 m/s, 3.48 m/s, and 3.98 m/s at 16.1 m/s, 15.9 m/s, 15.5 m/s, 15.5 m/s, and 15.3 m/s, for the 32.8 kg, 30.27 kg, 26.25 kg, 25.3 kg, and 22.6 kg masses respectively. The maximum rate of climb under fuel cell power for the 32.8 kg configuration is 0.62 m/s at an airspeed of 14.2 m/s.

For an aircraft optimized for climb, the airspeed at minimum drag power should be matched to the airspeed at maximum propulsive power. Genii however, is not such an airplane. As the values indicate, the airspeed for maximum climb is above the minimum power airspeed for the Genii aircraft.

3.3.5: Glide Ratio

The glide ratio of an aircraft at steady state is an exact measure of an aircraft's lift to drag ratio. As such, it would be a fantastic metric for determining the validity of the mathematical model, were it not for the stopped propeller's drag contribution. This drag component is large and involves much uncertainty. For higher airspeeds, the brake power of Genii's ESC is not sufficient to prevent propeller windmilling. A windmilling propeller typically produces more drag than a stopped one, however this phenomenon is dependent on many factors including the propeller blade's pitch angle.

Despite its inherent uncertainty, Eqn. (2.10) is utilized in an identical manner as for rate of climb except that the drag model is modified to include propeller component given by Eqn. 3.31. Eqn. (2.10) gives sink rate which can be easily converted to glide ratio

$$G_r = \frac{R_{oc}}{V} \tag{3.57}$$

The glide ratio with respect to airspeed is shown for the Genii aircraft in Fig. (3.18). By definition, the maximum glide ratio occurs at the airspeed corresponding to minimum drag.

The maximum glide ratios are all 12.5 at 14.4 m/s, 13.8 m/s, 12.8 m/s, 12.6 m/s, 11.9 m/s, for the 32.8 kg, 30.27 kg, 26.25 kg, 25.3 kg, 22.6 kg configurations respectively. The glide ratio remains nearly constant with respect to mass however the airspeed at maximum glide ratio increases with mass.

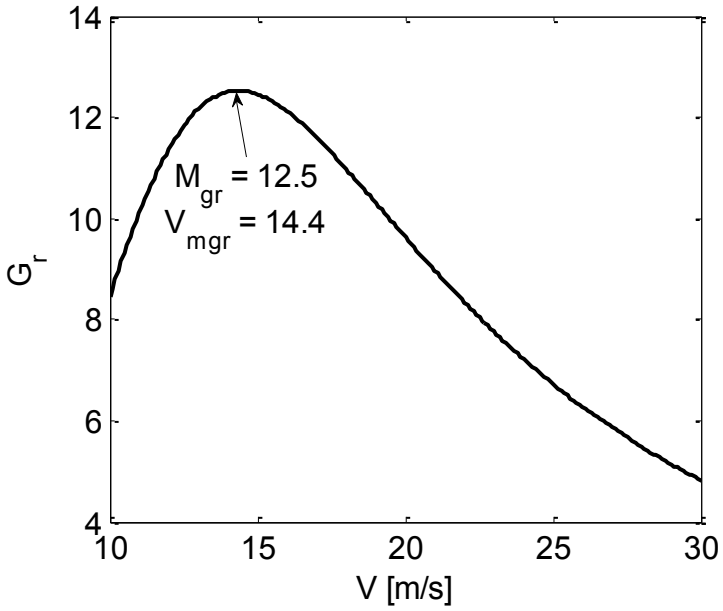

Figure 0.18: *Glide ratio with respect to airspeed for the 32.8 kg configuration.*

3.3.6: Takeoff

The aircraft's performance during the takeoff roll was modeled using numerical integration of the equations of motion.

$$F_i = T_{i-1} - D_{roll_{i-1}} - D_{tot_{i-1}} \tag{3.58}$$

$$V_i = V_{i-1} + \Delta t \left(\frac{F_i}{M}\right) \tag{3.59}$$

$$X_i = X_{i-1} + \Delta t \left(\frac{V_i + V_{i-1}}{2}\right) \tag{3.60}$$

where F is the total longitudinal force, T is the thrust, D_{roll} is rolling friction, and D_{tot} is the total aerodynamic drag, X is the position in meters from the starting point, and Δt is the time step. For

the sake of authenticity of the mathematical model, no feedback to the model i.e. measured rolling friction from the aircraft, was utilized. A generic rolling friction coefficient of 0.05 was used, a value taken from past measurements of a RC plane. The rolling friction was approximated as

$$D_{roll_i} = 0.05(W - L) \tag{3.61}$$

where and L is the aircraft lift. At ground incidence, the root of the wing is at 4.0 degrees angle of attack. This value is used to predict the total wing lift and drag coefficients, as well as induced drag. For low speed operation, the fuselage R_e was set to that experienced at 10 m/s and the dynamic pressure ratio was fixed at 1.5.

The aircraft is modeled to be level with the ground over the duration of the takeoff roll until the stall speed is reached. At stall speed, the aircraft is assumed to perform an instantaneous rotation and lift off. Therefore, the takeoff distance is modeled simply as the distance required to accelerate to V_{stall}. During actual test flights, rotation is performed between 1.1 to 1.2 times V_{stall}. This helps mitigate the risk of stalling during takeoff. Time domain plots of the takeoff roll for the 32.8 kg configuration of Genii are shown in Fig. (3.19).

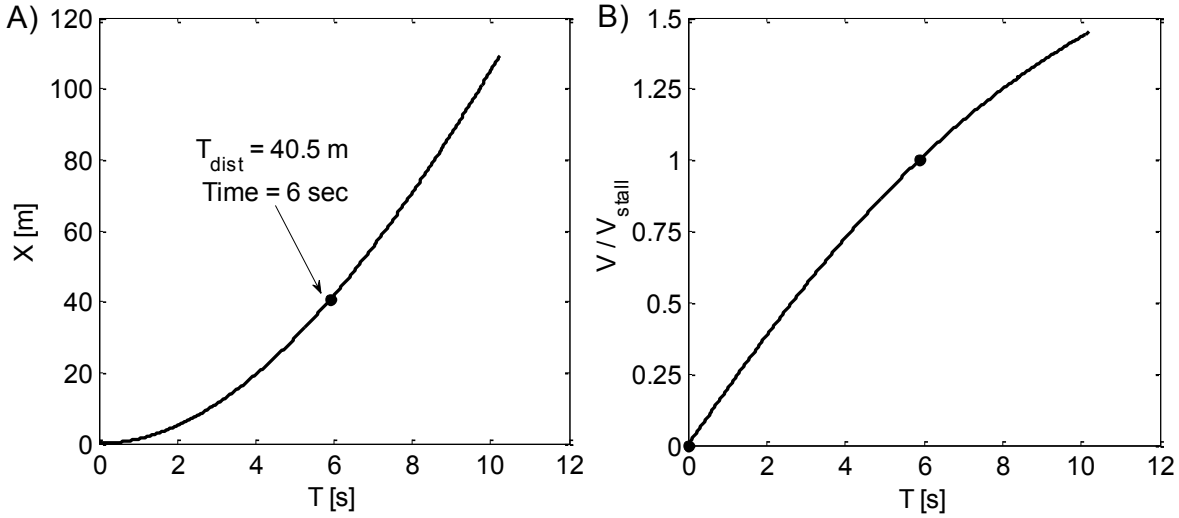

Figure 0.19: *Takeoff roll of the 32.8 kg configuration. A) Position from start of takeoff roll. B) Groundspeed over takeoff roll. Dot: Position and velocity for minimum takeoff distance.*

Eventually, even if held at ground attitude, the aircraft will take off by itself. The simulations plotted in Fig. (3.19) are ran out to this point. The minimum takeoff rolls are 40.5 m, 33.5 m, 23.8 m, 21.8 m, and 16.8 m for the 32.8 kg, 30.3 kg, 26.3 kg, 25.3, and 22.6 kg configurations respectively.

The effect of a pure headwind on the takeoff distance can easily be modeled by adding the windspeed to the airspeed in the aerodynamic lift and drag equations but not to the groundspeed. Figure (3.20) depicts the effect of headwind on minimum takeoff distance for the 32.8 kg configuration. Although not truly linear, the change in takeoff distance with respect to airspeed, $\frac{dT_{dist}}{dV_{wind}}$ is roughly -4.3 seconds over the range of airspeeds shown.

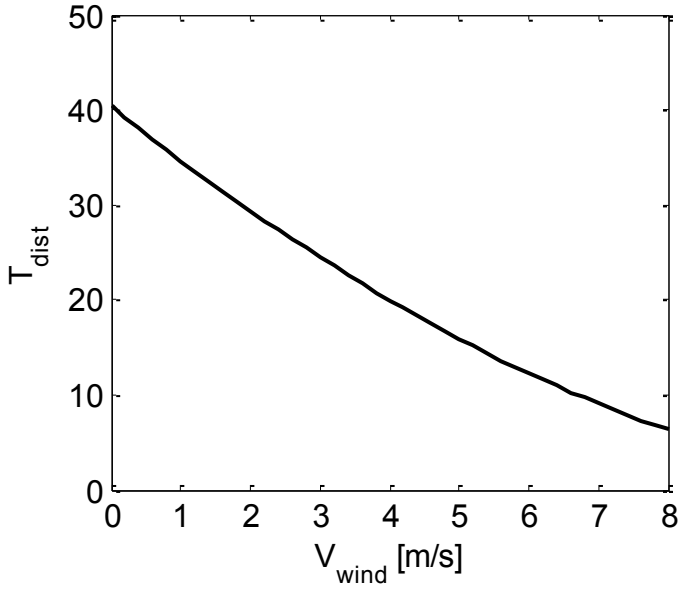

Figure 0.20: *Effect of a pure headwind on minimum takeoff distance for the 32.8 kg configuration.*

Error in the modeled takeoff distance stems largely from inaccuracy in the determination of rolling friction of the aircraft. Large error results from the particular bearings and tires used, as well as the alignment of the tires on the vehicle and dynamic effects such as steering input to correct for crosswind. The mathematical model's prediction of aerodynamic drag (solid line) and rolling friction (dashed line) for the 32.8 kg configuration are shown

below in Fig. (3.21). As would be expected, aerodynamic drag increases with vehicle airspeed and rolling friction decreases as the wing starts lifting. Rolling friction is the dominate drag contributor over the majority of the takeoff. The two curves cross at 4.7 seconds, only 1.3 seconds before reaching V_{stall}.

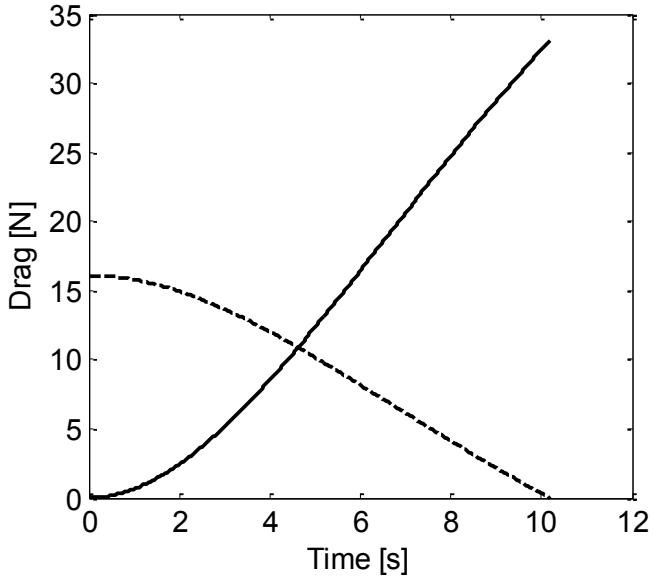

Figure 0.21: *Friction force (dashed line) and aerodynamic drag (solid line) over the takeoff roll of the 32.8 kg configuration.*

3.3.7: Level Turn

Aircraft performance in a sustained, level turn is estimated by rotating the lift vector out of level by adding a centripetal acceleration term, $\frac{V^2}{r}$. To maintain steady flight, the lift force must therefore be increased to develop the corresponding centripetal force. The required lift is

$$L = \sqrt{(Mg)^2 + \left(M\frac{V^2}{r}\right)^2} \tag{3.62}$$

where g is the gravitational acceleration and r is the turn radius.

For low tangential airspeeds, the turn rate will be limited by aircraft stall, i.e. the aircraft is unable to turn faster because no more lift force can be generated. This can be calculated from Eqn. (3.62) by substitution of the lift equation for L with the wing's lift coefficient at stall, $C_l = 1.09$ for the Genii aircraft. At a particular airspeed, the drag required to turn at stall will become more than the

available thrust from the propulsion system and the turn is said to be thrust limited. Turn rate in this regime is determined by running out the mathematical model for decreasing turn radius until the drag of the vehicle equals or just exceeds the thrust at that airspeed.

The maximum level turn rate for the 32.8 kg configuration is depicted as a solid line in Fig. (3.22). Turns made below 20 m/s are stall limited while turns made above 20 m/s are thrust limited. The turn rate approaches zero as the vehicle approaches the stall speed at zero turn rate, (12.79 m/s) or the maximum level airspeed (25.87 m/s). The dashed line is a continuation of the stall limited turn rate and could be realized for situations such as a dive or decelerating turn.

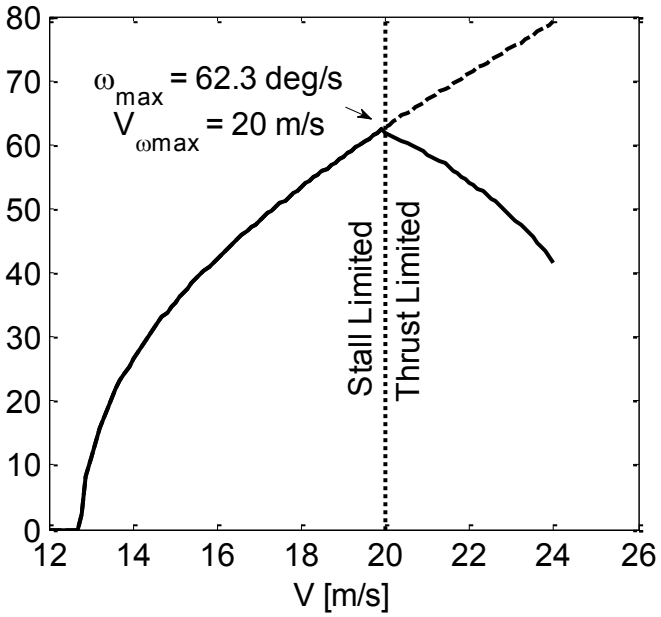

Figure 0.22: *Maximum turn rate of the 32.8 kg aircraft in steady level flight. Left of dotted line, stall limited. Right of dotted line, thrust limited. Solid line: maximum turn rate, Dashed line: continuation of stall limited turn rate.*

The maximum turn rates are 62.4 deg/s, 68.4 deg/s, 80.4 deg/s, 84.0 m/s, and 95.2 m/s for the 32.8 kg, 30.3 kg, 26.3 kg, 25.3 kg, and 22.6 kg configurations. The airspeed at maximum turn rate is 19.9 m/s for all considered configurations. Turn rate, bank angle, and "G" loading have the same physical meaning as turn radius and can be related to each other as

$$\omega = \frac{V}{r} \tag{3.63}$$

$$\beta = \tan^{-1}\left(\frac{gr}{V^2}\right) \tag{3.64}$$

$$G = \sqrt{1 + \frac{1}{g}\left(\frac{V^2}{r}\right)^2} \tag{3.65}$$

3.4: Performance overview

The parameters of interest from Section 3.2 are expressed in Table (3.1) below for convenience.

Table 0.1: *Overview of calculated aircraft performance for several flights of interest.*

Flight	M kg	V_{stall} m/s	M_{roc} m/s	V_{mroc} m/s	$M_{roc,FC}$ m/s	$V_{mroc,FC}$ m/s	M_{gr}	V_{mgr} m/s
14	32.8	12.79	2.48	16.1	0.62	14.2	12.5	14.4
13	30.3	12.29	2.77	15.9	0.77	13.9	12.5	13.8
12	26.3	11.44	3.33	15.5	1.07	13.3	12.5	12.8
11	25.3	11.23	3.48	15.5	1.15	13.2	12.5	12.6
10	22.6	10.61	3.98	15.3	1.4	12.8	12.5	12.5

Flight	M kg	T_{dist} m	ω_{max} deg/s	r_{min} m	β_{max} deg	G_{max}	$V_{\omega max}$ m/s
14	32.8	40.5	62.4	18.3	65.6	2.4	19.9
13	30.3	33.5	68.4	16.7	67.6	2.6	19.9
12	26.3	23.8	80.4	14.2	70.6	3.0	19.9
11	25.3	21.8	84.0	13.6	71.4	3.1	19.9
10	22.6	16.8	95.2	12.0	73.5	3.5	19.9

3.5: Stability

The stability and dynamic motion of the Genii aircraft is not experimentally investigated in this study however UAV's have been used for the analysis of flight dynamics and control system effectiveness (Joradan et al. 2006). Computations of aircraft stability can range from very simplistic approximations using generic lift slopes and small perturbations to complex models accounting for the nonlinearities in lift slopes, turbulence, control surface freedom, and structural

flexure to name just a few variables. In accordance with the theme of this report, the stability analysis for the Genii aircraft was simplified to an appropriate level to assure aircraft safety while not becoming so involved as to warrant its own program of study.

The control system and data acquisition systems of the Genii aircraft do not possess the fidelity required to accurately perturb specific aircraft modes and extract the eigenvalues of the resulting motion. As such, the stability analysis herein is performed simply to assure vehicle safety. The AVL code developed by Drela and Youngren (Athena Vortex Lattice, 2014) which was used for computation of wing performance is also capable of perturbing the aircraft and running a battery of cases to determine both the stability derivatives and eigenvalues of an entire aircraft. The static longitudinal stability is calculated by hand and compared to the results from AVL for validation, however all other values are computed by AVL alone.

For linear analysis, the longitudinal static stability requirement is expressed as

$$\frac{dM_y}{d\alpha} < 0 \tag{3.66}$$

The aircraft's pitching moment, $M_y$was set to zero in the development of Eqn. (3.42). Ignoring the effects of fuselage and propeller on the pitching moment, Eqn. (3.66) can be expressed in coefficient form as.

$$\frac{dC_{my}}{d\alpha} = \frac{dC_{m_w}}{d\alpha} - \left(A_{c_h} - x_{cg}\right)\eta \frac{S_h}{SM_{ac}} k_{2d} \frac{dc_{l_h}}{d\alpha} \tag{3.67}$$

where (for review), C_{m_w} is the pitching moment coefficient of the wing, A_{c_h} is the longitudinal location aerodynamic center of the horizontal tail, x_{cg} is the longitudinal location of the center of gravity, η is the dynamic pressure ratio accounting for the propwash velocity over the tail, S_h is

the horizontal tail area, S is the wing area, M_{ac} is the mean aerodynamic chord, k_{2d} corrects the horizontal's section lift slope to the horizontal's lift slope and c_{l_h} is the lift coefficient of the horizontal tail. k_{2d} can be determined via Eqn. (3.26) using the appropriate geometry for the horizontal tail. Additionally, the lift slope of the horizontal tail must be corrected for the downwash derivative over the horizontal tail from the wing and propeller as per Section 3.1.8.

AVL calculations were ran without the propeller's influence. With η set to unity and the effect of the propeller on the downwash derivative of the tail ignored, Eqn. (3.67) yields $\frac{dCm_y}{d\alpha_r} = -1.64$, a 16% difference from AVL's calculation of -1.95. Accounting for propeller effects, the power-on pitching moment derivative is $\frac{dM_y}{d\alpha_r} = -1.02$. The additional downwash component due to the propeller is partially compensated for by the increase in dynamic pressure. The full complement of static stability derivatives calculated by AVL for the Genii aircraft are shown in Table (3.2).

Table 0.2: *Stability derivatives of the Genii aircraft.*

Derivative of		With Respect to				
		Pitch	Yaw	Pitch Rate	Yaw Rate	Roll Rate
z force	C_l	5.51	0.00	11.10	0.00	0.00
y force	C_y	0.00	-0.24	0.00	0.18	0.00
x mom	C_{mx}	0.00	-0.06	0.00	0.13	-0.55
y mom	C_{my}	-1.95	0.00	-23.23	0.00	0.00
z mom	C_{mz}	0.00	0.08	0.00	-0.06	0.04

Standard aircraft coordinates apply (+X aft, +Y starboard, +Z up). Note that X (roll) and Z (yaw) moment coefficients are expressed with respect to wingspan while the Y (pitch) moment coefficient is expressed with respect to the mean aerodynamic chord.

The aircraft is seen to be statically stable in the most important degrees of freedom. A positive change in pitch results in a negative change in pitching moment about Y. A positive change in

yaw angle results in a positive (restoring) moment about Z and the corresponding negative moment about X as the aircraft rolls out of the slip due to the dihedral effect.

With the stability derivatives calculated, AVL can solve the linearized motion equations to calculate the eigenvalues of the dynamic modes of Genii. This process requires knowledge of the vehicle's moment of inertia in all three axis. These were approximated by uniformly distributing the mass of the fuselage, wing, and ballast over representative shapes.

The eigenvalues for the five motion modes as well as the half-life and the period of the periodic modes are displayed below in Table (3.3) for the 32.8 kg configuration in level flight at 17 m/s.

Table 0.3: *Dynamic motion modes of the 32.8 kg configuration of the Genii UAV, 17 m/s.*

Mode	Eigen Value [rad/s]		Period [s]	Half Life [s]
	Real	Imaginary		
Roll	-8.677			0.08
Short Period	-7.489	±6.038	1.04	0.09
Dutch Roll	-0.552	±2.393	2.63	1.26
Phugoid	-0.051	±0.187	33.5	13.56
Spiral	0.008			82.58

The aircraft is stable and damped in the four significant modes, with half-lives less than the period for the Phugoid, Dutch Roll, and Short Period modes. The Spiral mode is unstable. This is not uncommon in aircraft because the doubling time is sufficiently large that the instability does not have time to develop unless perfectly trimmed flight is desired. Although the damping of the Phugoid mode is small, it too will not adversely affect the flying qualities of the Genii aircraft because, like for the Spiral mode, the pilot will always be actively controlling the aircraft.

CHAPTER 4

4.1 Propeller Performance

Accurate characterization of the propeller's performance is critical for computing the aircraft's capabilities and for comparing flight data to performance calculations. Because Genii is not equipped with a load cell, thrust cannot be measured in-situ, but must be calculated from the motor's speed and the airspeed of the vehicle. Several methods can be utilized to calculate the thrust performance of propellers including CFD and VLM techniques. As with calculating aircraft drag, CFD becomes prohibitively time expensive while VLM cannot account for viscous effects which are especially important for propellers at low advance ratios.

For the sake of time and accuracy, direct tests of propeller performance were utilized. Superior accuracy can be achieved by utilizing a wind tunnel for propeller testing, however this option was out of the budget for the Genii team, as well as most teams seeking to design a low-cost UAV. The cost of renting a university wind tunnel is roughly $500/hr without additional charges for setup or rental equipment (Pricing, Terms and Conditions, Orlan W. Nicks Low Speed Wind Tunnel 2013) and (Services and Rates, University of Washington Aeronautical Laboratory 2012). Due to the high-rental cost of a wind tunnel facility, a car-top testing devise was built to generate propeller performance data. This technique saves time and cost at the expense of accuracy, repeatability, and a more limited rage of operation.

The module developed for this task is called the Propulsive Unloading Performance Indicator (PUPI). The devise measures thrust, torque, rpm, voltage, and current draw. A pitot tube and differential pressure transducer are utilized to log incident airspeed. The temperature of motor and ESC under simulated flight conditions is also recorded by means of thermocouples. Car-top testing

of small or scaled aircraft and propulsion systems has precedent in academia. For example, Tigner et al. (1998) used a semi-constrained car mounting to determine stability derivatives of a small research aircraft and tune the aircraft's controller. The car-top testing technique was also used with good effect by Lundstrom (2012) to quantify the performance of low-Reynolds number propellers for micro UAVs. Wind tunnel tests of propellers suitable for small UAVs are well documented in the literature. Brandt and Selig (2011) and Merchant (2004) document information on thrust coefficient, power coefficient and efficiency of low-Reynolds number propellers, but for operation below the intended power level and with smaller propellers than desired for application on Genii. Similar wind tunnel tests were performed by Ol et al. (2008) and were compared to a hybrid propeller performance algorithm.

4.2 Test Setup

PUPI measures thrust and torque by means of a motor affixed to a rotatable shaft mounted on a translating gantry. The motor is mounted collinear to the shaft by means of an aluminum bracket. Radial bearings are used to affix the shaft to the gantry and a linear ball-bearing slide is used to allow smooth translation of the gantry assembly. The arm of the gantry holds a counterweight that serves to balance the cantilevered motor which would otherwise bind the linear slide. The entire unit is attached to a 0.56 meter tall steel frame that bolts to the roof rack

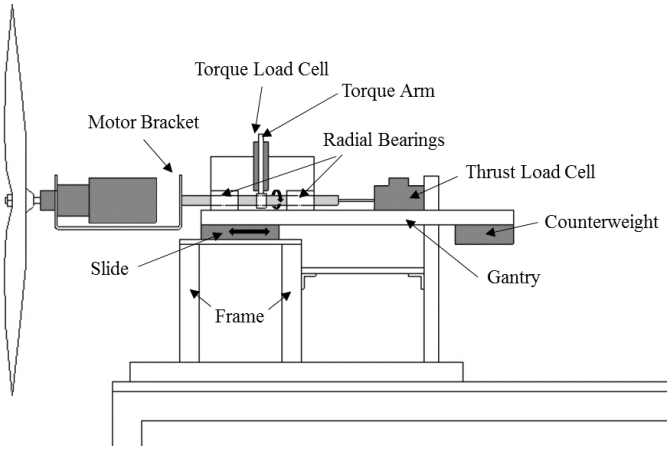

Figure 0.1: *Side view of mechanical components comprising the PUPI test module. Vehicle is not shown below the schematic.*

of a car, placing the propeller out of the boundary layer. The mechanical configuration of PUPI is schematically shown in Fig. (4.1).

To measure thrust, the gantry is constrained longitudinally with an Omegadyne LC105-25 load cell. Torque is measured by attaching an Interface MB-25-170 load cell to a 6.0 cm torque arm secured to the shaft with a set screw collar. The 0-30 mV signals from the load cells are amplified by a factor of 107.4 by two Texas Instruments INA-121P operational amplifier integrated circuits. Vehicle airspeed is recorded using a United Sensor PBB-12-F-9-KL 717 pitot tube and Ashcroft Xldp 1.5" DWC pressure transducer. The load cells and pressure transducer are logged on a PC using a National Instruments cDAQ-9172 chassis with a National Instruments 9211 analog-to-digital converter module and a custom developed LabVIEW® program.

Motor rotational frequency is obtained by measuring the frequency of one of the three AC motor phases. One of the phases is tapped with an opto-isolator and the waveform read via the NI 9211 module. A low-pass filter algorithm is applied in LabVIEW® to remove the noise associated with duty cycle switching present at partial-throttle conditions.

Temperatures are measured with type K thermocouples logged through the same chassis with a National Instruments 9215 thermocouple amplifier module. The thermocouple measuring motor temperature is secured on the outside of the motor can. The thermocouple measuring ESC temperature is secured to the base of the ESC's heat sink with Kapton tape. The instrumentation configuration is given in Fig. (4.2).

The voltage and current of the propulsion system are also measured and recorded. Motor voltage is measured off of a simple voltage divider using a National Instruments 6009 analog-to-digital

converter because no more channels were available on the NI 9211. Motor current is measured by an ACS758LCB-100B hall-effect sensor also tied to the NI 6009.

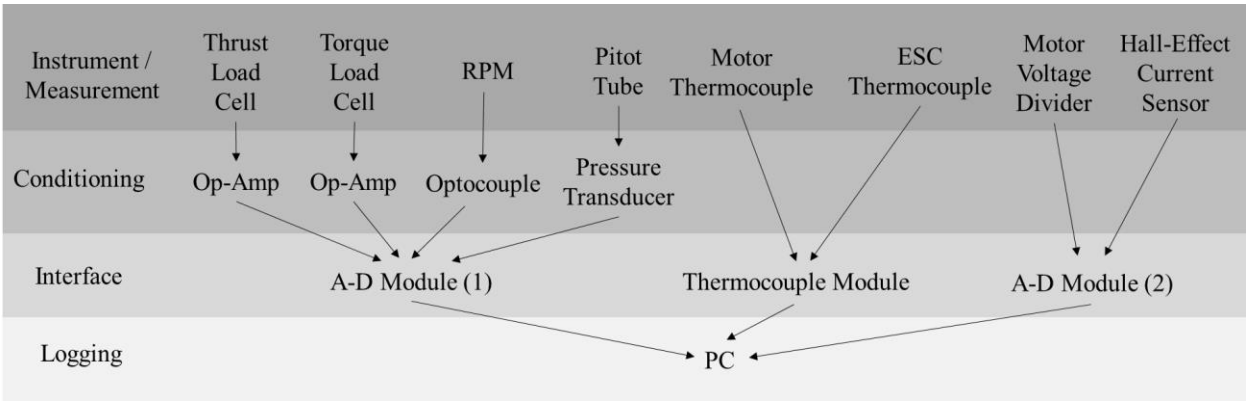

Figure 0.2: *Hierarchy of measurement equipment. From top to bottom: conditioning equipment, interface devices to PC, and data logging devices. A-D Module (1): NI 9211. Thermocouple Module: NI 9215. A-D Module (2): NI 6009.*

Independent variables are vehicle velocity, rotational frequency and propeller/motor hardware selection. A basic proportional feedback loop was implemented in LabVIEW® to hold the motor rotational frequency nearly constant for testing. For this purpose, a National Instruments 9401 digital-in-out module was used to communicate with the motor's electronic speed controller. This rpm hold system was useful for test-stand validation but may not be required for some tests. A simple remote control transmitter and receiver combination could be used instead if the reader does not need precise control of rpm.

4.3 Test Stand Validation

An assessment of the accuracy of PUPI was performed. A series of tests were conducted to compare thrust data taken from the PUPI stand with thrust data for the same model propeller reported by Ananda (2014) using a wind tunnel. Their methodology is reported in Brandt and

Selig (2011). The wind tunnel data is populated for relatively low power operation compared to the range for which Genii is intended to be operated (150 watts vs 2000 watts respectively). As such, comparison with the data from Ananda (2014) represents a worst-case scenario with PUPI operating at the extreme low end of its useful measurement range.

A comparison of thrust coefficient for an APC 19X12E propeller obtained with PUPI is plotted against data from Ananda (2014) in Fig (4.3). Thrust coefficient, C_t, and advance ratio, J, are defined as:

$$C_t = \frac{T}{\rho n^2 D^4} \tag{4.1}$$

$$J = \frac{V}{nD} \tag{4.2}$$

where n the rotational frequency in revolutions per second and D is the propeller diameter.

Data was collected at 3000 rpm ±10 by holding rotational frequency constant and parameterizing vehicle airspeed. Data was taken at 20 hz and downsampled to six points from 2 m/s to 22m/s at 3m/s intervals. Each point represents the average of several hundred samples. The error bars in Fig (4.3) represent the first standard deviation from the mean.

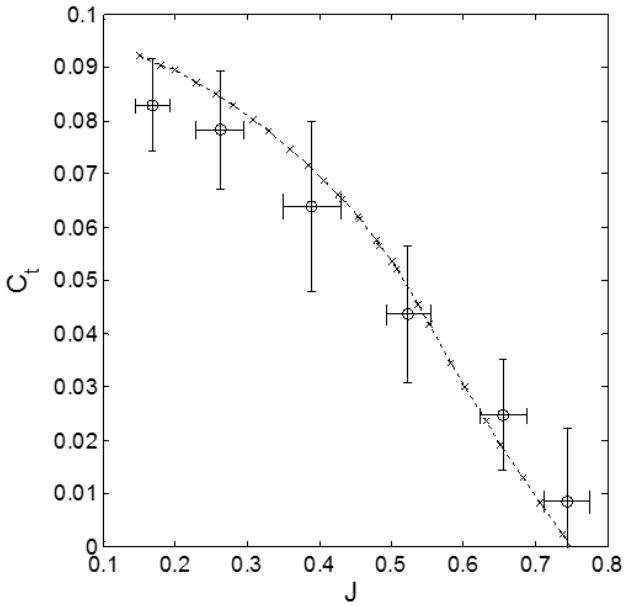

Figure 0.3: *Thrust coefficient of an APC 19X12E propeller with respect to advance ratio. Dashed line with "x's": Ananda (2014). Circles: Experimental data from PUPI test stand. Error bars denote standard deviation.*

Due to the large sample size, the 95% confidence interval for each point is very small. As such, a statistical difference between the experimental data taken and Ananda (2014) is present. Uncertainty in the reported values from Brandt and Selig and Ananda (2014) is unlisted, however due to the quality of their setup, it is assumed to be negligible compared to the experimental uncertainty in PUPI. The combined uncertainty due to calibration drift, thermal effects, and hysteresis was determined to be ± 0.14 Newtons. These effects are small compared to the ± 0.40 Newtons uncertainty due to noise. The combined uncertainty in the reported thrust is ±0.42 Newtons or $C_t = \pm 0.003$. The maximum error off of the data from Ananda (2014) is ± 1.46 Newtons or $C_t = \pm 0.009$. This error is sufficiently appreciable to argue that methods similar to PUPI should not be used for high-accuracy propeller documentation, however for the purpose of characterizing the Genii UAV, this accuracy is acceptable.

One source of error that is difficult to detect is bias error resulting from oblique flow though the propeller due to the influence of the vehicle. To observe if appreciable oblique flow is present, yarn tufts of roughly 3 feet in length were affixed to a vertical post placed along the vehicle's centerline. For velocities below 50 miles per hour, inappreciable obliqueness in flow was observed. The camera and tuft inspection technique was unable to resolve the velocity vector to high accuracy, and it is assumed that some oblique flow due to the vehicle is present but less than five degrees. Additionally, the ability to install PUPI along the vehicle's centerline adds an additional oblique component. These effects, in addition to the drag of the gantry and the placement of test equipment in the propeller wake, are most likely the sources of error resulting in the deviation from wind tunnel tests.

4.4 Representative Data

The motor and propeller combinations utilized on Genii are tested for safety using the PUPI system to simulate a flight environment. Both the Hacker A60 motor and the final Nue 2220-1.5Y motor were validated on the PUPI test stand before flying. Validation consists of several tests. The motor and propeller combination under investigation are run at full throttle to steady state temperature in this shop before finally testing on a vehicle. Additionally, slow ramps in motor rpm are performed to check for harmonics or other problem areas. The flight motor is utilized for propeller testing so its long-term reliably is verified over the duration of several propeller tests. Further information on the PUPI module during motor trail runs is presented by Chaney et al. (2014).

Although motor testing is useful, the primary use of the PUPI system is propeller performance determination. A characterization of an APC 26X15 propeller with a 4.0 inch spinner operating from 2000 rpm to 3500 rpm was performed using PUPI to generate data useful for performance analysis of the Genii UAV. In addition to thrust coefficient C_t, the propeller's power coefficient C_p, and efficiency η are determined with respect to advance ratio J,

$$\eta = \frac{VT}{P} \tag{4.3}$$

$$C_p = \frac{P}{\rho n^3 D^5} \tag{4.4}$$

where P is the shaft power, determined here as the product of torque and angular frequency in radians per second. Data from these tests are presented in Fig (4.4). Propeller performance is determined from rotational speed, thrust, and torque, therefore the effect of motor and battery charge state is irrelevant, however a Neu 2220-1.5Y motor was utilized for these tests.

To generate these data, the PUPI module was held at nearly constant rpm using the rudimentary control system while the vehicle parameterized velocity in 5 mile per hour increments. Each rpm trial was terminated when the airspeed was sufficient for the propeller to stop producing thrust or when the speed limit of 55 miles per hour was reached. For clarity only, the 2000 and 3500 rpm trials are shown in Fig. (4.4). The average wind speed was approximately 7 miles per hour. Uncertainty in efficiency becomes large as thrust and torque significantly degrade with advance ratio. The hollow squares for the 2000 rpm trail efficiency are included to show the data trend but have standard deviations higher than 20%.

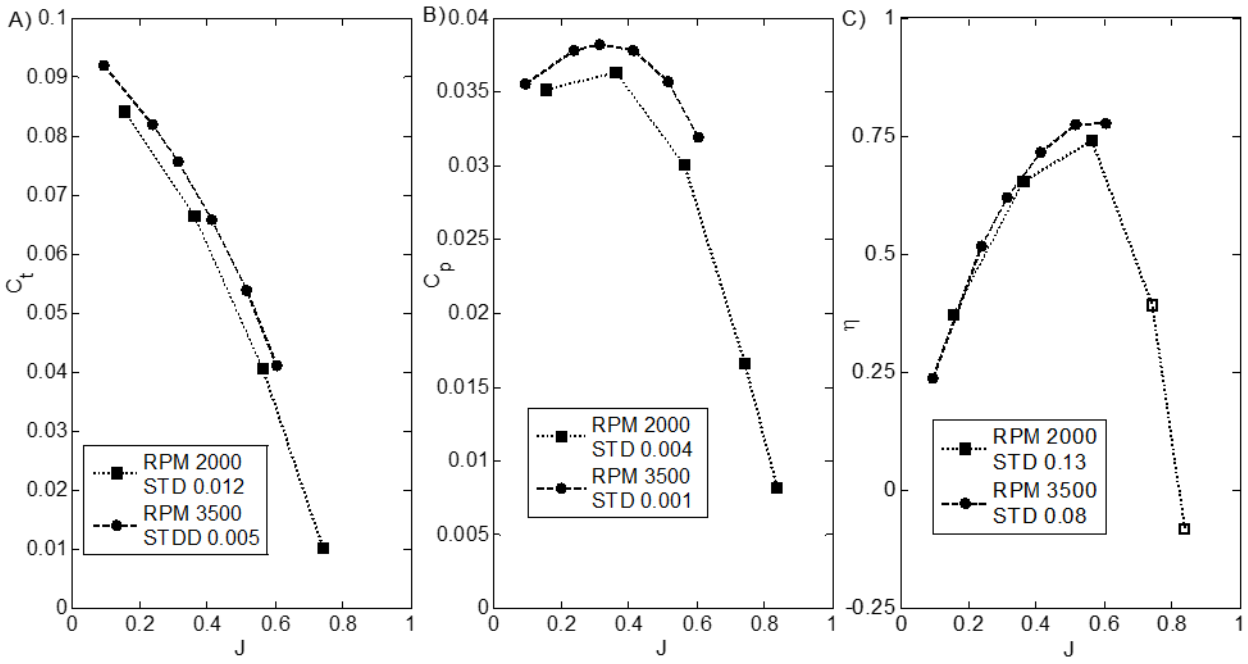

Figure 0.4: *Performance of an APC 26X15E propeller. A) Thrust coefficient vs advance ratio. B) Power coefficient vs advance ratio. C) Efficiency vs advance ratio. Squares and dots: 2000±20 rpm. Circles and dashes: 3500±20 rpm. For all cases, maximum standard deviation in advance ratio is 0.065. Hollow squares in C denote high uncertainty.*

Similar to Fig. (4.3) the galaxy of data taken at 20 Hz for different velocities is down sampled by averaging over velocities from 2 m/s to 26 m/s in 4m/s increments. The maximum standard deviation encountered in advance ratio was 0.065. For constant rpm, thrust decays in an approximately quadratic relationship to advance ratio. The propeller's performance is not Reynolds number independent and over the range of testing, the propeller's performance was seen to improve with rpm. The propeller reaches a maximum efficiency of 78% at an advance ratio of approximately 0.6. For comparison, the Genii aircraft demonstrated its best low-power cruise at an advance ratio of 0.52. This is investigated further in Section (5.6.2).

In keeping with the technique utilized for the calculation of wing profile drag, a quadratic regression was performed on the test data to produce an equation describing the thrust to advance ratio relationship. Rpm in flight was found to fall predominantly between 2000 and 4000 rpm and the regression was performed on the combined data between these values. The result, therefore, approximates the thrust over this range but does not account for the variation in thrust with Reynolds number. The regression was found to be

$$C_t = 0.09572 - 0.04500\mathrm{J} - 0.08375\mathrm{J}^2 \tag{4.5}$$

A plot of Eq. (4.5) along with down-sampled data for three discrete rpm ranges is shown in Fig. (4.5). Scatter in the data within these ranges, especially at high advance ratio, makes it difficult to accurately account for the small performance difference between them. For this reason, the total average approach of Eq. (4.5) is utilized for all thrust calculations.

After performing initial tests with the PUPI module, it was determined to be a suitable indicator of propeller performance for the purposes of the Genii UAV. The preliminary results from PUPI demonstrated that the propulsion system was functioning nominally and was suitable for flight.

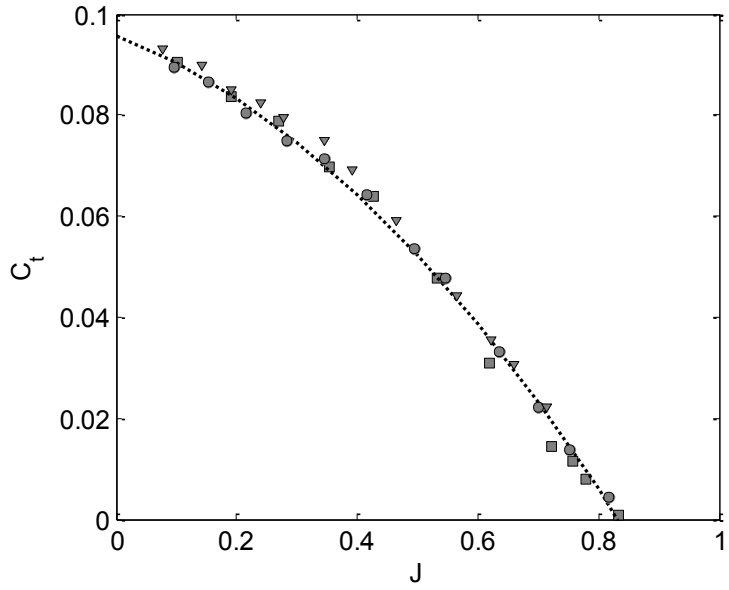

Figure 0.5: *Thrust performance of the APC 26X15E propeller. Dotted line: Eq. (4.5), Squares: rpm = 2000-2500, Circles: rpm = 2500-3000, Squares: rpm = 3000-3500.*

CHAPTER 5

5.1 Analysis of Recorded Data

In this chapter, data obtained from the aircraft during flight testing will be directly compared to calculations made by the mathematical model described in Chapter 3. A description of flight operations of the Genii aircraft, including flying techniques and flight profiles will be detailed first. The data collected by the instrumentation discussed in Chapter 2 is used to produce metrics to compare against the mathematical model. The metrics considered here are thrust required at a given airspeed and rate of climb, takeoff time domain profiles of position and airspeed, power required for level flight, and steady turn radius. For the thrust metric, flight data is down-sampled and filtered to compare against the mathematical model. The filtered results are compared dimensionally to the mathematical model for flight 12 and are compared in nondimensional form against a collection of data from flights 10 through 14.

The takeoff performance of the Genii aircraft for flight 14 is plotted against simulations produced using simple numerical time integration methods. A test of low-power operation during flight 14 is used to prove that Genii can maintain level flight solely under power from the proposed PEM fuel cell. Finally, a comparison is made between the actual turn radius vs a theoretical turn radius given the current power setting and airspeed of Genii during a characteristic turn in flight 14.

5.2 Flight Description

At the time of release of this report, Genii has performed 14 flights with three mishaps for a total flight time of 3.58 hours. The Genii aircraft was in development over the course of these flights, and the aircraft's powerplant, weight, and electronic systems changed substantially from the first flight to the last. Because each flight was a demonstration of the aircraft in either a new configuration or weight, a balance had to be found between collection of repeatable flight data, safe operation, and validation of the aircraft in its new configuration. For the purpose of comparison to the mathematical model, flight data will be used from flights 10 through 14 only, as the DAQ system changed little between these flights.

5.2.1 Flight Dates and Events

A list of aircraft flights along with their date and duration is given in Table 5.1. All flights were performed at the Lewis-Clark RC club's field at Mann Lake near Lewiston, ID. The runway consists of an asphalt strip approximately 8 meters wide by 95 meters long oriented at 30 / 210 degrees and 557 meters above Mean Sea Level (MSL). Temperatures ranged from 40.5 C to -12.0 C from operations in the summer to operations in the winter.

Table 0.1: *List of Genii flights to date.*

Battery Powered Flight Statistics			
	Date	Duration	
Flight 1	05/18/13	16 min	First Flight
Flight 2	05/31/13	28 min	First Autonomous Operation
Flight 3	06/15/13	32 s	Power Failure Mishap
Flight 4	08/10/13	3.5 min	Dead Stick Landing
Flight 5	09/28/13	22 min	Rain and Wind
Flights 6&7	10/05/13	46 min	Good Weather
Flights 8&9	02/23/14	30 min	Test A New Motor
Flights 10&11	03/08/14	38 min	Test at Additional Weight
Flight 12	03/23/14	14 min	Crash, Pilot Error
Flights 13&14	04/05/14	17 min	Flight at Full Weight

Table 5.2 outlines the hardware configuration of the aircraft for each flight. Flights one through three utilized a Hacker A40-10L motor and a 6.7:1 gearbox driving either an APC 27X13 or 26X15 propeller. Flight three resulted in

Table 0.2: *Mass and hardware configuration of Genii for flights to date. Weight and balance data for several early flights are not available.*

Flight	Mass, Kg	Motor	Propeller	ESC
1	--	Hacker A40-10L+6.7:1 GB	APC 27X15E	MGM Compro TMM 7063-3
2	20.71	Hacker A40-10L+6.7:1 GB	APC 27X15E	MGM Compro TMM 7063-3
3	23.70	Hacker A40-10L+6.7:1 GB	APC 26X15E	MGM Compro TMM 7063-3
4	--	Hacker A60-20M	APC 26X15E	Castle Creations Phoenix Edge HV 80
5	22.50	Hacker A60-20M	APC 20X15E	Castle Creations Phoenix Edge HV 80
6	21.70	Hacker A60-20M	APC 20X15E	Castle Creations Phoenix Edge HV 80
7	--	Hacker A60-20M	APC 20X15E	Castle Creations Phoenix Edge HV 80
8	--	Neu 2220-1.5Y+6.7:1 GB	APC 26X15E	Jeti Mezon 75 15S Opto
9	--	Neu 2220-1.5Y+6.7:1 GB	APC 26X15E	Jeti Mezon 75 15S Opto
10	22.58	Neu 2220-1.5Y+6.7:1 GB	APC 26X15E	Jeti Mezon 75 15S Opto
11	25.30	Neu 2220-1.5Y+6.7:1 GB	APC 26X15E	Jeti Mezon 75 15S Opto
12	26.25	Neu 2220-1.5Y+6.7:1 GB	APC 26X15E	Jeti Mezon 75 15S Opto
13	30.27	Neu 2220-1.5Y+6.7:1 GB	APC 26X15E	Jeti Mezon 75 15S Opto
14	32.80	Neu 2220-1.5Y+6.7:1 GB	APC 26X15E	Jeti Mezon 75 15S Opto

a crash after the ESC failed due to a misunderstanding of how to drive the motor. Excessive heating in both motor and ESC was produced by operating the motor at reduced duty cycle pulse width modulation but at its rated power. This motor was not used for subsequent flights because the aircraft's predicted mass and power requirement grew.

Flights four through seven utilized a Hacker A60-20M motor and Castle Creations Phoenix Edge HV ESC. This configuration was not intended to drive the final aircraft but was used for these flights to help develop understanding of motor selection to tailor the final motor configuration. The final motor was a Neu 2220-1.5Y with a 6.7:1 Gearbox. This was controlled by a Jeti Mezon 75 15S Opto ESC which was selected because of the high voltage of the fuel cell.

5.2.2 Vehicle Piloting and Operations

Genii's mechanical configuration allows it to be disassembled at the base of the tail as well as the ±1 meter butt lines of the wing in order to fit it into a pickup truck bed. The landing gear can also

be detached from their junction with the fuselage. This facilitates easy assembly in the field. Typical flight preparations take between 40 minutes to 2 hours and consist of vehicle assembly, vehicle mechanical systems check, Ardupilot and Raspberry Pi startup and data link, and final functionality checks.

The aircraft is primarily flown by the pilot in "Stabilize" mode. This allows the pilot full control of the aircraft, but uses the Ardupilot's inertial measurement unit to return the aircraft to a level flight condition should the control sticks on the transmitter be released. Autonomous flight capability is possible with the Ardupilot, however Genii is rarely operated in this mode.

Successful autonomous course following was demonstrated in flight 2, however for higher power flights, large electromagnetic field interference caused by the more powerful propulsion configurations resulted in difficulty utilizing the onboard magnetic compass. As such, all data gathered in flights 10 through 14 was done under stabilized control only. Good data must be sufficiently un-accelerated to be compared with the steady mathematical model. This relies on the pilot's ability to keep the aircraft in steady flight conditions, a difficult task when faced with varying wind conditions, thermals, and the wake of nearby trees. Additionally, perspective from the ground makes it difficult to maintain precise altitude and heading. Qualitative observations indicate that the Ardupilot was better at maintaining un-accelerated flight than the external pilot. It is unfortunate that in the interest of time, autonomous operation was not available to parameterize flight profiles. The technique used to extract un-accelerated data from bulk flight data taken under manual operation is discussed in section 5.3.

5.2.3 Flight Profiles

For takeoff, the aircraft is aligned with the runway most directly facing the current wind conditions. An assistant holds the aircraft while the throttle is advanced to full and releases the aircraft on command. This allows the relatively slow spool up of the motor (over 3 seconds to full rpm) to be complete without consuming runway. The pilot steers the aircraft down the runway until the airspeed is approximately 1.2 times stall speed, at which point the pilot gently brings back the stick until the aircraft rotates and begins to climb. Because less than 10% of Genii's weight is on the steering nose-wheel, aft stick is not typically applied until it is desirable to rotate. The 1.2 times stall speed is roughly maintained during the initial climb-out. Genii's initial climb typically brings it to an altitude between 80 and 150 meters where most flight operations are conducted. Because Genii must be kept sufficiently close to the pilot for safe control, a crosswind turn must performed before the aircraft reaches the 100 meter altitude. A climbing turn is executed through 180 degrees to face the aircraft downwind.

Once at altitude, the pilot performs maneuvers in an attempt to assess the safety of the current aircraft configuration and to gather flight data. This typically consists of either an oval or elongated figure eight pattern with two crosswind legs and an upwind and downwind leg roughly parallel to the runway. An oval pattern is typical, but a figure eight is used if a cross wind to the runway exists. This allows both crosswind turns to be performed upwind. The pilot typically attempts to gather good data during the longer upwind and downwind legs of the pattern. The throttle is maintained at a desired position and all attempts are made at keeping the aircraft in un-accelerated flight. The aircraft may descend, ascend, or fly level depending on the throttle position and desired airspeed. The throttle position often cannot be maintained during the crosswind turns

at the end of each upwind or downwind leg due to the extra power requirement for these maneuvers. A profile of flight 14 is shown below in Fig. (5.1) as an illustration of the flight pattern.

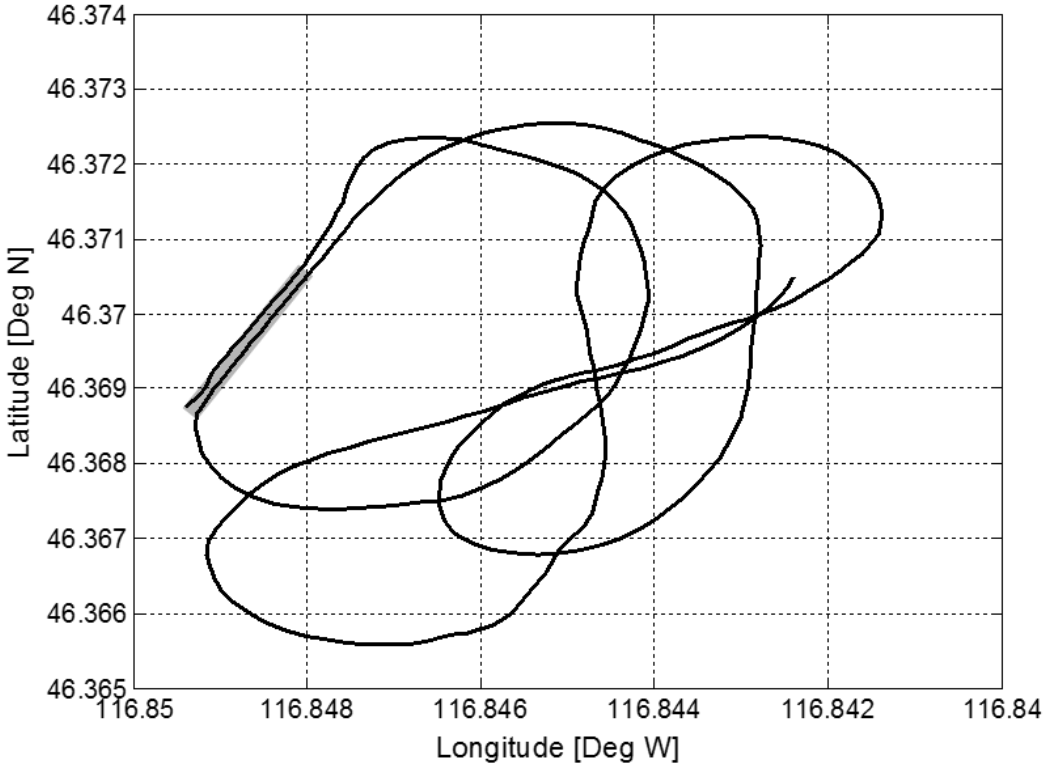

Figure 0.1: *Path of Genii for flight 14. Grey block approximates runway. Note: Start point is in the air. Latitude and Longitude are not in scale.*

Flight 14 is shorter than most of the flights from which data was extracted which makes the figure easier to read. Before takeoff, insufficient satellite reception caused a position error which is resolved midway through the first crosswind turn. As such, the starting point shown in the figure is in the air at 46.705N, 166.843W. A rough approximation of the runway is included for reference.

Before landing, it is standard to perform several low passes over the runway to gauge wind conditions and how the aircraft handles at low speed. Most flights are performed at either a different configuration or weight, so the pilot often needs time to learn the aircraft's landing procedure and airspeed. For a typical landing, the aircraft is brought in under low power, and the

throttle is cut when the landing decision has been made, typically at the threshold of the runway. A soft flare is attempted and any "crab" angle due to crosswind is corrected by rudder input. Genii is not equipped with brakes, and for flights above 25kg it was typical for the aircraft to overrun the 95 meter runway into the grass before stopping.

Time domain plots of four parameters of interest from flight 12 are displayed in Fig. 5.2. Throttle is increased at t = 0.1 minutes and the aircraft is released at t = 0.2. Airspeed increases and the aircraft takes off at approximately t = 0.4 minutes when the airspeed reaches 19m/s. The aircraft performs an initial climb of 80 meters to an altitude of 655 meters MSL reached at t = 1.6 with an airspeed of 17 m/s. The "steps" in rpm shown in Fig. (5.2D) show time periods over which the pilot performed maneuvers at a constant throttle setting to gauge the vehicle's power consumption

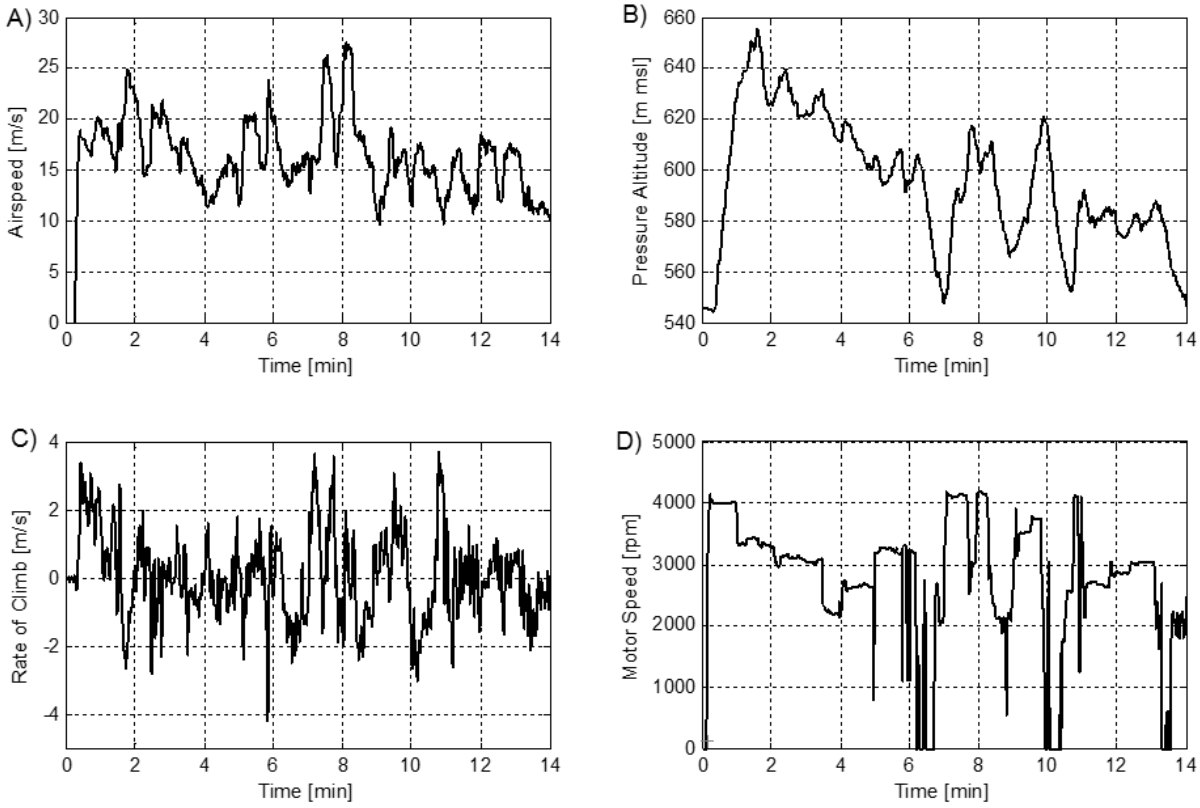

Figure 0.2: *Parameters of interest recorded for flight 12 A) Airspeed B) Pressure Altitude MSL C) Rate of Climb D) Motor Speed vs. Time*

at different airspeeds. A descent to a low pass is performed at t = 6.2 and the low pass is performed at t = 7.0 followed shortly by a climb back to a safe pattern altitude of 600 meters MSL (55 m above ground level). A final landing approach is started at t = 13.1.

5.3 Data Down-Sampling

The analysis of aircraft performance in the next sections relies both on time-averaged data for maneuvers over several seconds, but also bulk data taken at short intervals. As described in detail in Chapter 2, flight data is recorded by both an ArduioPilot module and a custom Raspberry Pi based unit. Within the ArduioPilot, different channels are sampled at different frequencies. Post processing is required to properly synchronize the data in time and down-sample the data to a common frequency. Data is extracted from its native comma separated vector format using MS Excel and then read into Matlab. A script was developed in Matlab to synchronize the data in time and perform down-sampling. To synchronize the data, a common channel was sampled by both the ArduioPilot and RPi. In this case, airspeed worked well. After synchronization, all channels were down-sampled to 1hz by averaging. Because the RPi does not use a real time operating system, slight differences in clock speed between it and the ArduinoPilot were noted to cause a roughly 1.5 second mismatch in the time over the course of a 15 minute flight. This error is not corrected due to the difficulty in resolving both a start and end triggering time to within a 1.5 second accuracy.

5.4 Drag Performance

Direct measurements of drag, such as those available from wind tunnel tests, were not a financial option for the Genii project and for most UAVs of this scale. Therefore, aircraft drag is extracted from the aircraft's flight performance. For the case of un-accelerated flight at angles of attack less than that of stall and when not climbing or descending, the approximation can be made that the vehicle's thrust and drag are equivalent. Under this assumption, comparing the drag calculated by the mathematical model to the thrust of the aircraft is equivalent to comparing the calculated drag to measured drag.

The Genii aircraft is not equipped with a load cell within the aircraft. As such, thrust is determined by measuring the rpm of the motor and airspeed of the aircraft and using these parameters in an experimentally determined performance curve for the propeller. Like the drag-thrust assumption, this is an approximation of the true thrust. Uncertainties in this assumption result from dynamic events, sideslip, fuselage interference, and the accuracy of the performance characterization. The development of the propeller characterization is detailed in Chapter 5. A flowchart of the comparison between calculated and measured metrics is shown in Fig. (5.3). Profiles of thrust vs airspeed for different rpm were developed and condensed into a single relationship of advance

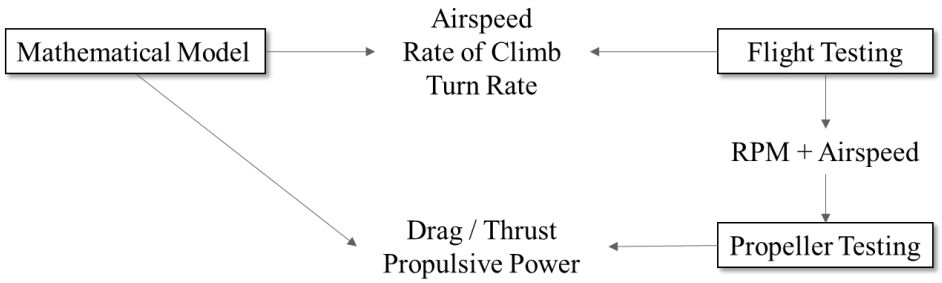

Figure 0.3: *Flow chart of metrics and their origins.*

ratio (J) with respect to Thrust Coefficient (C_t). Reynolds effects are not accounted for and true C_t varies ±4% from the relationship used depending on the rpm of the propeller.

5.4.1 Flight 12 Drag Performance

A description of the drag-thrust performance of Genii for flight 12 is given in Fig. (5.4) before showing the same data over flights 10 through 14 in nondimensional form in Section 5.3.3. Flight 12 occurred on 03/23/2014 with an aircraft mass of 26.25 kg and nearly calm winds. This flight produced more noise-free flight data than any other flight, despite ending in a pilot-induced crash during final landing approach. Figure (5.4) depicts the thrust values as calculated from observed rpm and airspeed during the flight test. For this case, the flight data has been filtered to include only data within $\pm 0.5 \frac{m}{s^2}$ acceleration in the longitudinal direction and $\pm 0.3 \frac{m}{s^2}$ in the vertical direction. Other less restrictive filters are applied such that: $-10º < Pitch < 14º$, $-10º < Bank < 10º$, and $-50 \frac{Rpm}{s} < \frac{dRpm}{dt} < 50 \frac{Rpm}{s}$. Data "strings" or consecutive points in time not broken by filtering can be observed in the figure as clusters of points

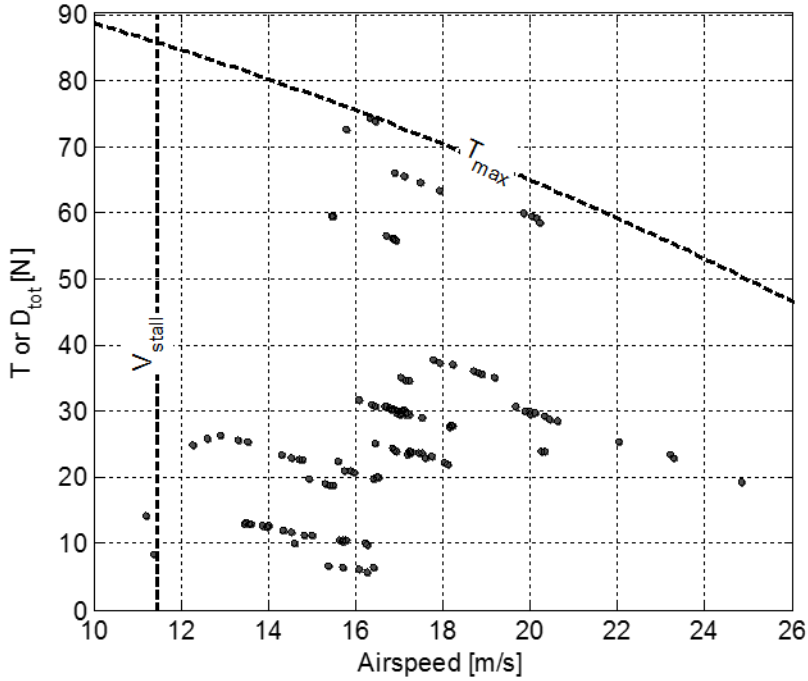

Figure 0.4: *Thrust values as calculated from rpm and airspeed during flight 12. Vertical dashed line, Vstall = 12.6 m/s. Descending dashed line: maximum anticipated thrust.*

descending in thrust and airspeed. These cluster can be as long as twenty points, or twenty seconds given the 1Hz downsampled frequency. These clusters of points exhibit little change in rpm over their interval, and therefore decrease in thrust with increasing airspeed as governed by the propeller model.

The calculated stall speed of Genii at the flight 12 mass of 26.25 kg is shown as a dashed vertical line at 11.44 m/s. It is understandable that un-accelerated flight conditions exist below the stall airspeed because of the inaccuracy of the stall prediction technique. The lack of un-accelerated flight points below a given airspeed is not necessarily an indicator of stall at that airspeed. For flight 12, stall is over predicted by 1% from the left-most stable data point, however the amount of over-prediction from true stall cannot be assessed from the data. A more detailed experimental determination of stall could be performed using techniques such as tufting, but were not utilized in this research. Despite the inaccuracy of the stall prediction technique described in Section 3.3.1, experimental results do not show substantial deviation to invalidate this method for generic prediction of stall.

Figure (5.4) also includes a dashed line representing the maximum predicted thrust for Flight 12. This curve was developed using the propeller model with an rpm of 4150, the maximum rpm measured during the static run-up before flight. The accuracy of this curve is dependent on the accuracy of the propeller model and the assumption that the maximum rpm will not deviate appreciably from 4150 rpm when the motor is unloaded at higher airspeeds. Despite these inaccuracies, experimental data did not exceed this prediction for flight 12. The closest un-accelerated point was 0.25 Newtons (less than 1%) below the maximum thrust curve. Like for stall, the lack of un-accelerated points above this line does not validate its accuracy.

Figure (5.4) also shows the difficulty of obtaining un-accelerated data at high speed, a common problem in each flight test of Genii. Due to increased control effectiveness at high speed, the pilot can experience difficulty flying the aircraft in a steady manner. Additionally, it is easier for the pilot to accidently exceed the load limit envelope of the aircraft when at high speed. As such, high speed and full-throttle operation of Genii was not performed for long durations.

5.4.2 Combined Flights

Flight data such as that in Fig. (5.4) is useful, but analysis of independent data for each flight would be unwieldy. Each flight was conducted at different mass, so performance would not be directly comparable. Efforts were therefore undertaken to present flight data for flights 10 through 14 together in nondimentional form. By normalizing thrust by the weight of the aircraft and the airspeed by the stall speed, the drag curves calculated by the mathematical model for each mass converged to within 2% over the range of interest. This indicates that the results are satisfactorily nondimensionalized and the data is comparable. Nonliniearities due to Reynolds number do cause the small 2% variation.

Figure (5.5) shows the combined flight data in nondimensional form and under the same filtering criteria as discussed for the Flight 12 data. Data spans from T / W of zero to roughly 0.25. Steady data within the filtering criteria above a V / Vstall ratio of 2.04 was not observed and only two points occur above V / Vstall = 2.00.

A dashed vertical line is added at the V / Vstall ratio of 1 for reference and the max thrust curves for each flight are shown as dotted lines descending to the right. Because all flights had approximately the same maximum thrust, they appear distinct when nondimentionalized by the variable weight of the aircraft. Additionally, four divisions of differing rate of climb are shown as

solid black lines: Roc / Vstall = -0.08, Roc / Vstall = 0.00, Roc / Vstall = 0.08, and Roc / Vstall = 0.16. Points corresponding to each Roc within ±0.04 are produced as squares, circles, triangles, and diamonds respectively. Due to the large constellation of data, each Roc range is investigated independently later for ease of viewing.

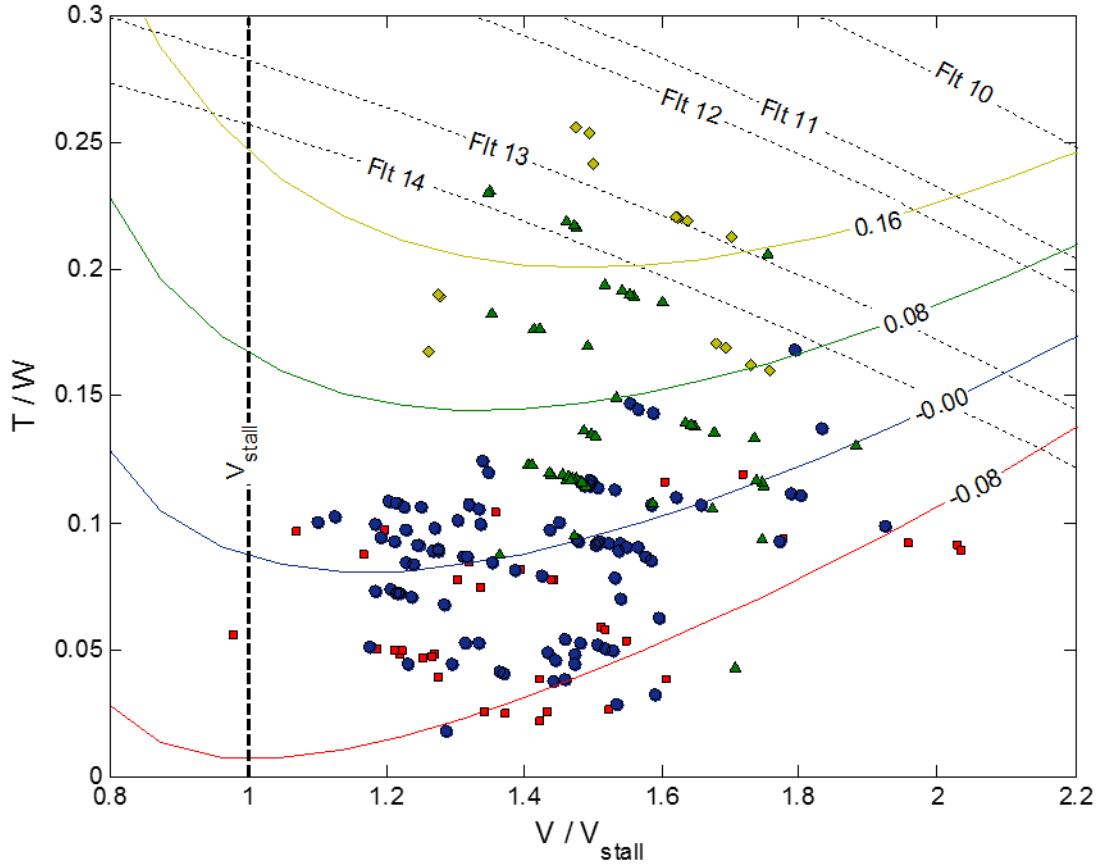

Figure 0.5: *Nondimensional performance of Genii, flights 10 thru 14. Squares: Vstall = -0.08±0.04, Circles: Vstall = 0.00±0.04, Triangles: Vstall = 0.08±0.04, Dimonds: Vstall = 0.16±0.04. Solid lines: mathematical model calculation for Roc / Vstall = -0.08,0.00,0.08, and 0.12, Dotted lines: Maximum T/W ratio predicted, Dashed vertical line: stall.*

Logically, higher rates of climb increase the required thrust to weight ratio at a given airspeed. This phenomena is accounted for using the steady climb approximation such that a fictions drag is added to account for the rate of climb.

$$T_{add}V = P_{spare} = R_{oc}W \tag{5.1}$$

where T_{add} is the additional thrust required, P_{spare} is the spare propulsive power after overcoming drag power. The parameter T_{add} is then added to the drag computed by the mathematical model to predict the thrust required at a given airspeed and rate of climb.

The different rates of climb shown in Fig. (5.5) are examined in detail in Fig (5.6). Each normalized rate of climb of 0.00, -0.08, 0.08, and 0.16 is shown in its own subfigure, A), B), C) and D) respectively. No data point falls exactly on these normalized rates of climb, so data within a normalized rate of climb of ±0.04 off of the mean are taken as a set. The upper and lower 0.04 cutoffs are indicated by the dotted lines in each subfigure. The solid line represents the T / W curve for the nominal value of either Roc / Vstall = 0.00, -0.04, 0.08, or 0.16.

Each datapoint that experimentally falls within the 0.04 limits off the mean are shown in the applicable subfigure. Not all experimental points fall within the dashed lines that show the calculated upper and lower bounds for that set. These points are in disagreement with the mathematical model. All points, however, are to some degree dissimilar to the mathematical model even if within the bounds. This is investigated more in subsection 5.3.4.

Also shown in Fig. (5.6) are down-sampled points of experimental data for each normalized velocity range V / Vstall = 1.1±0.1, 1.3±0.1 to 1.5±0.1, and 1.7±0.1. Each down-sampled point is notated with plus or minus the first standard deviation in both T / W and V / Vstall except for when only one data point exists within that normalized velocity range. Both the 0.08 and 0.16 nominal rates of climb do not have data in the V / Vstall = 1.1±0.1 range.

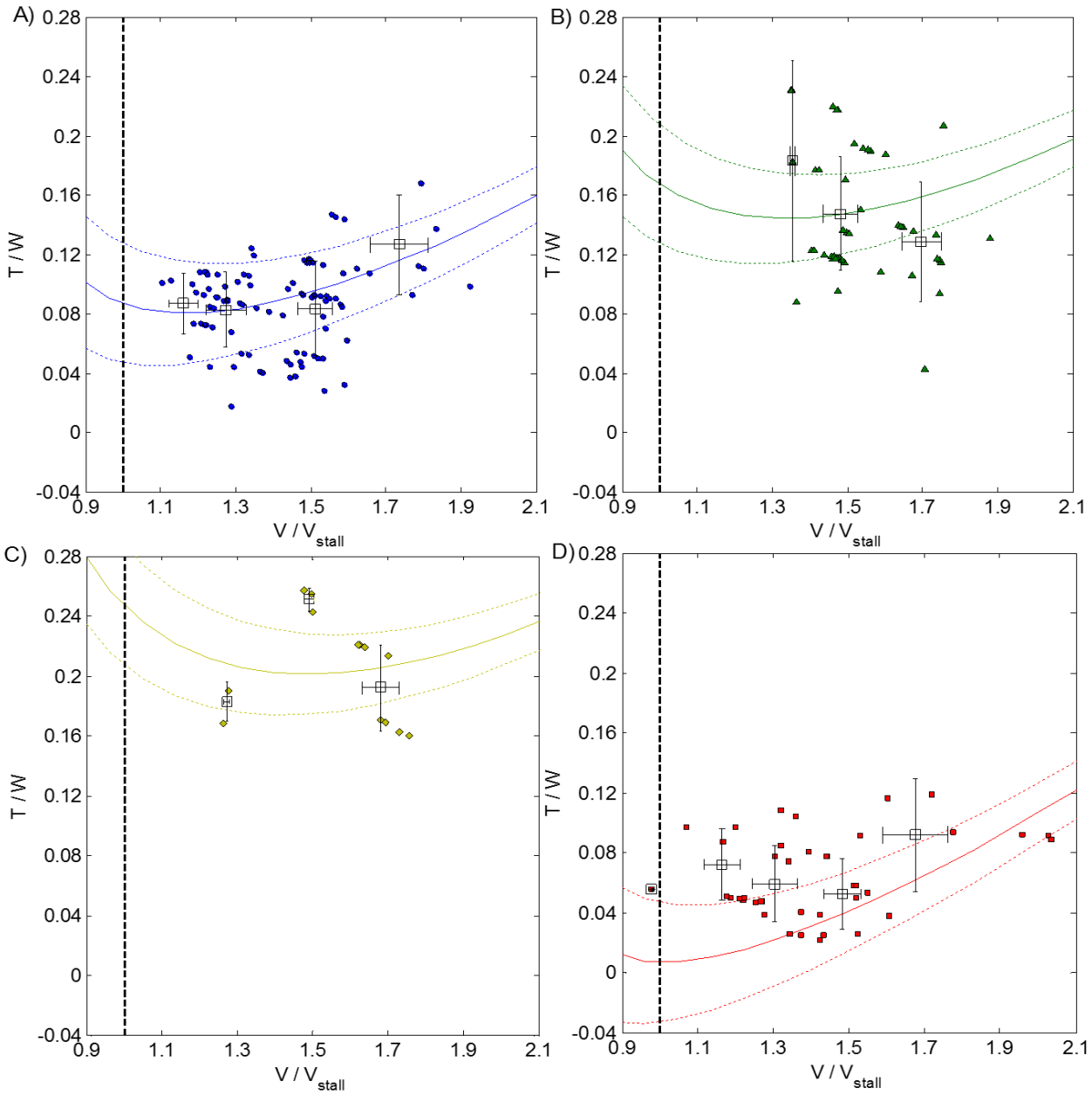

Figure 0.6: *Experimental data compared to mathmatical model for A) Roc / Vstall = 0.00, B) Roc / Vstall = -0.08, C) Roc / Vstall = 0.08, D) Roc / Vstall = 0.16. Solid line: mathmatical model calculation, Dotted lines: mathmatical model calculation ±0.04, Dashed vertical lines: stall. Circles: downsampled data within the normalized velocity ranges 1.1±0.1, 1.3±0.1, 1.5±0.1, and 1.7±0.1. Error bars in "y": Standard deviation in T / W, Error bars in "x": Standard deviation in normalized velocity.*

A general idea of the accuracy of the mathematical model can be drawn from this data. For the case of the sets Roc / Vstall = 0.00 and 0.08, the mathematical prediction falls within the standard deviation of each downsampled experimental point. Each downsampled point in the Roc / Vstall = 0.00 range falls within the ±0.04 Roc / Vstall bounds for that set. This is not the case for the other ranges where not only do points lay outside the set but the standard deviations do not overlap the nominal T / W values predicted by the mathematical model. For the Roc / Vstall set of 0.08±0.04, the downsampled point for the range of V / Vstall = 1.7±0.1 lies outside the 0.04 lower limit. For the Roc / Vstall set of 0.16±0.04, the down-sampled point for the range of V / Vstall = 1.5±0.1 lies more than a standard deviation outside the 0.04 upper limit. For the Roc / Vstall set of -0.08±0.04, the down-sampled point for the range of V / Vstall = 1.1±0.1 lies more than a standard deviation outside the 0.04 upper limit.

5.5 Accuracy of Mathematical Model for Required Thrust

Because each experimental point (solid symbols) in Fig. (5.6) has its own corresponding normalized rate of climb that may fall within ±0.04 the mean value (hollow squares), a quantified assessment of error between experiment and model cannot be determined from the figure. This assessment is performed in this subsection. The mathematical model is ran for the appropriate normalized rate of climb for each point shown in Fig. (5.6), and the resulting calculated T / W is compared the measured T / W to determine the percent error associated with that data point. The percent error between model and measured values and the average percent error are defined respectively

$$E_p = 100\% \left(\frac{f_t - a_t}{a_t} \right) \tag{5.2}$$

$$\overline{E}_p = \frac{100\%}{n}\sum_{t=1}^{n}\frac{f_t - a_t}{a_t} \tag{5.3}$$

where n is the number of samples, f_t is the sample's computed value and a_t is the sample's measured value. Additionally, the absolute percent error and the absolute average percent error are defined respectively,

$$A_p = 100\%\left|\frac{f_t - a_t}{a_t}\right| \tag{5.4}$$

$$\overline{A}_p = \frac{100\%}{n}\sum_{t=1}^{n}\left|\frac{f_t - a_t}{a_t}\right| \tag{5.5}$$

Percent error is a good indicator of the model's accuracy while absolute percent error (when the percent error is low as for this case) is a good indicator of the model's precision. In other words, the average percent error describes a bias between the mathematical model's calculation and experimental measurements. The absolute average percent error, rather, also includes random effects. When no bias exists, average error is zero but absolute average error can still exist due to random distribution of error about the mean. As such, average percent error is a good metric for assessing the accuracy of the model on a whole when applied over large sections of data. Conversely, absolute average percent error is a good metric for assessing the expected accuracy of the model for a single data sample.

The average percent error is computed for the ranges V / Vstall equals 1.1±0.1 , 1.3±0.1 , 1.5±0.1, and 1.7±0.1. These data are depicted in Fig. (5.7) still classified by the nominal rates of climb

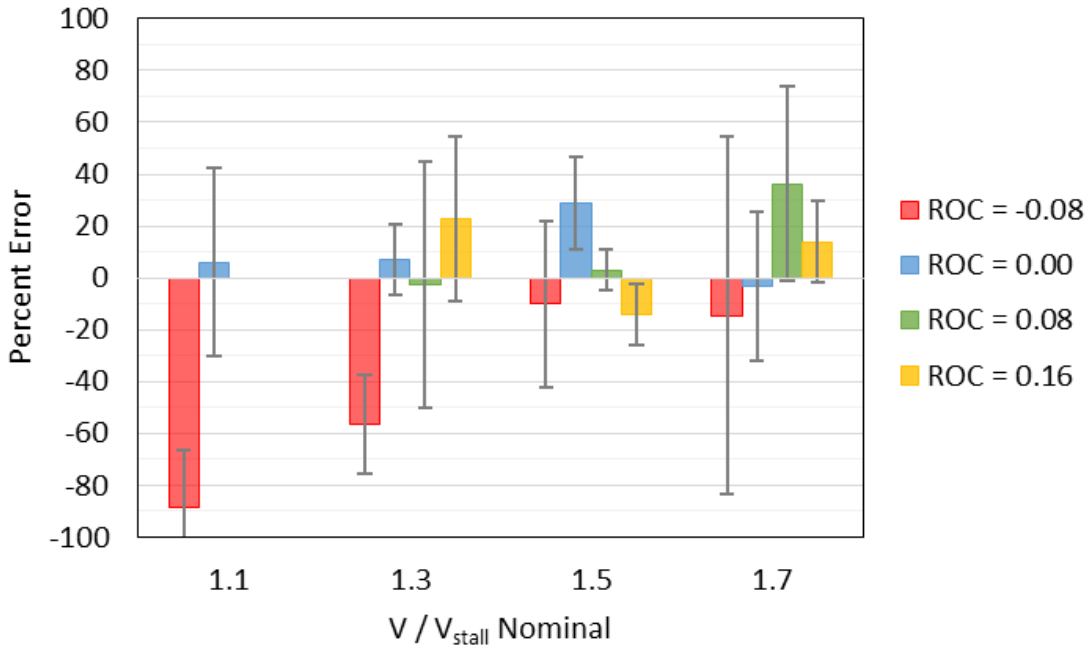

Figure 0.7: *Average percent error between calculation and experimental data for thrust required for level flight . Normalized velocity ranges 1.1±0.1 , 1.3±0.1 , 1.5±0.1 and 1.7±0.1, Normalized rates of climb -0.08±0.04, 0.00±0.04, 0.08±0.04, and 0.16±0.04.*

within each velocity range, either Roc / Vstall equals -0.08±0.04 , 0.00±0.04, 0.08±0.04, or 0.16±0.04. The V / Vstall range of 1.1±0.1 does not have data for the Roc / Vstall sets of 0.08±0.04 and 0.16±0.04. Ranges that have more than one data point include error bars denoting the 95% confidence interval based on the student's t distribution. It can be noted that this interval is large for many sets that have few data points and large variance.

The model's average percent error is seen to range from -88.6% to as low as -2.73% percent depending on the normalized velocity range. Several points deviate more than their confidence interval from zero error, indicating that with a minimum of 95% confidence, the model is in disagreement with these points. The 95% confidence intervals in Fig. (5.7) are large due to the

lack of data in each rate of climb set and velocity range. The model is seen to be most inaccurate for the normalized Roc = -0.08 case at low normalized airspeeds.

The model is flagrantly incorrect for the descending case of normalized Roc = -0.08 case at V / Vstall = 1.1 and 1.3. This is most likely due to a misrepresentation of the true velocity due to the angle of attack of the aircraft with respect to the axis of the pitot tube. Genii rarely descends with the axis of the aircraft (and pitot tube) tube aligned with the velocity vector, but usually keeps the nose at a mostly level attitude and allows the aircraft to sink. As such, by definition of the normalized Roc = -0.08, an additional 8% of the vehicle's velocity vector is orientated perpendicular to the pitot tube at stall. This produces a 4.6 degree increase in angle of attack (at stall) over that formed between the aircraft and the horizontal component of the velocity. This angle of attack is not accounted for in the mathematical model and will create a much higher drag condition than the model would calculate. The effect is more pronounced at low airspeeds as $V \rightarrow V_{stall}$ whereas at higher airspeeds the vertical velocity component becomes negligible. This trend is seen as the accuracy of the normalized Roc = -0.08 improves with airspeed. For all velocity ranges, however, the mathematical model under-calculates drag for the descending case.

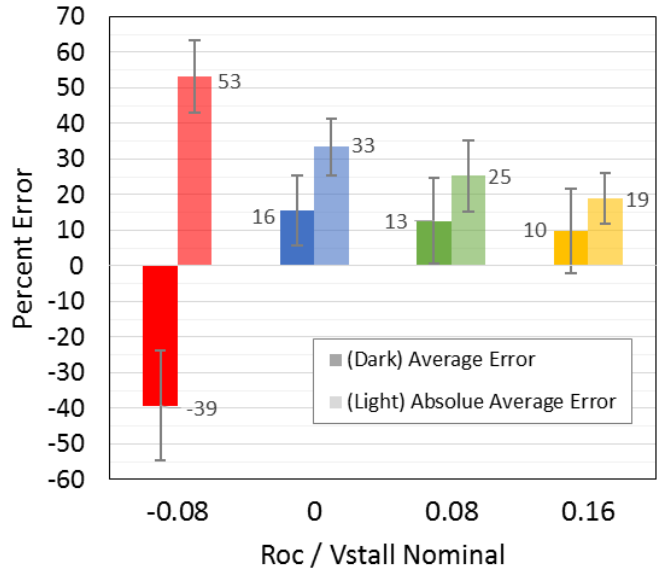

Figure 0.8: *Average percent error and absolute average percent error for required thrust calculation at any velocity within normalized Roc ranges -0.08±0.04, 0.00±0.04, 0.08±0.04 and 0.16±0.04.*

The average percent error and absolute average percent error of each Roc set over all the velocities considered is shown in Fig. (5.8). The absolute percent error decreases with increasing normalized Roc, most likely because the magnitude of the error is similar to other cases but required T / W increases with Roc. Excluding the descending case, the average percent error is below 15% for all other rates of climb.

The data is down-sampled further in Fig. (5.9) to combine each normalized rate of climb set under the same normalized velocity divisions used in Fig. (4.7), V / Vstall equals 1.1±0.1 , 1.3±0.1 , 1.5±0.1 and 1.7±0.1. This depicts the accuracy of the mathematical model over these velocity ranges without regard to rate of climb. Both the average and absolute average percent errors are shown.

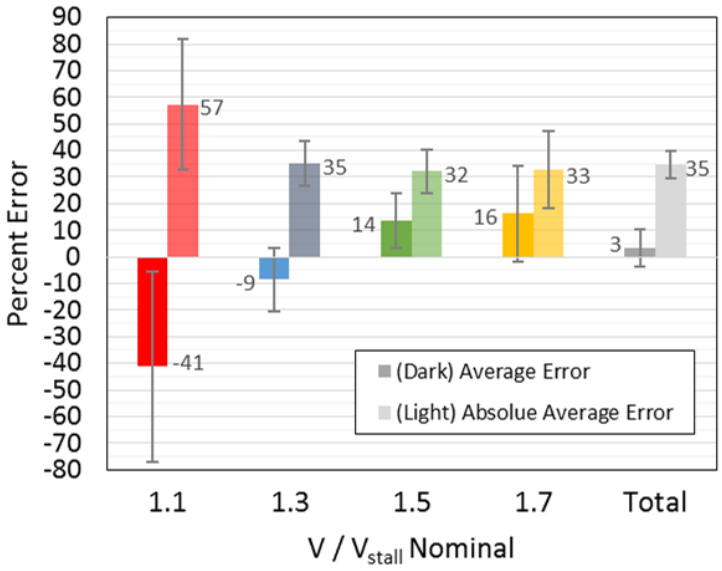

Figure 0.9: *Average percent error and absolute average percent error for the thrust required at any rate of climb within normalized velocity ranges 1.1±0.1, 1.3±0.1, 1.5±0.1 and 1.7±0.1 and total model accuracy over all normalized velocity ranges.*

Again, the 95% confidence interval is included. The collective data show much better agreement to the mathematical model than the individual sets. This is a large part due to the fact that the high-accuracy cases, namely Roc / Vstall = 0.00±0.04 contain a proportionally large amount of data compared to the low accuracy cases. For normalized velocity ranges V / Vstall = 1.3 and 1.7, the average percent error falls within the 95% confidence interval of perfect agreement.

The down-sampling of data is taken to the extreme when all points are considered under one set and is shown as the total percent error and total absolute percent error in Fig. (5.9). These are the errors averaged over the entire range of data sampled. The total average percent error in the calculation of drag if found to be 3.2±7.0%, which indicates a reasonably high degree of accuracy. The mathematical model's absolute average percent error in the calculation of drag over all considered rates of climb and airspeeds is 34.6% with a 95% confidence interval of ±5.14% which indicates low precision.

The model's performance is more easily seen in Fig. (5.10) and (5.11) which depict the probability distribution of the percent error between the mathematical model's calculated drag and flight testing thrust values. Intervals are 5%. Part of the right hand tail in Fig. (5.10) had to be truncated for scaling reasons, thus pulling the mean slightly more positive than would be implied by the visible data points alone.

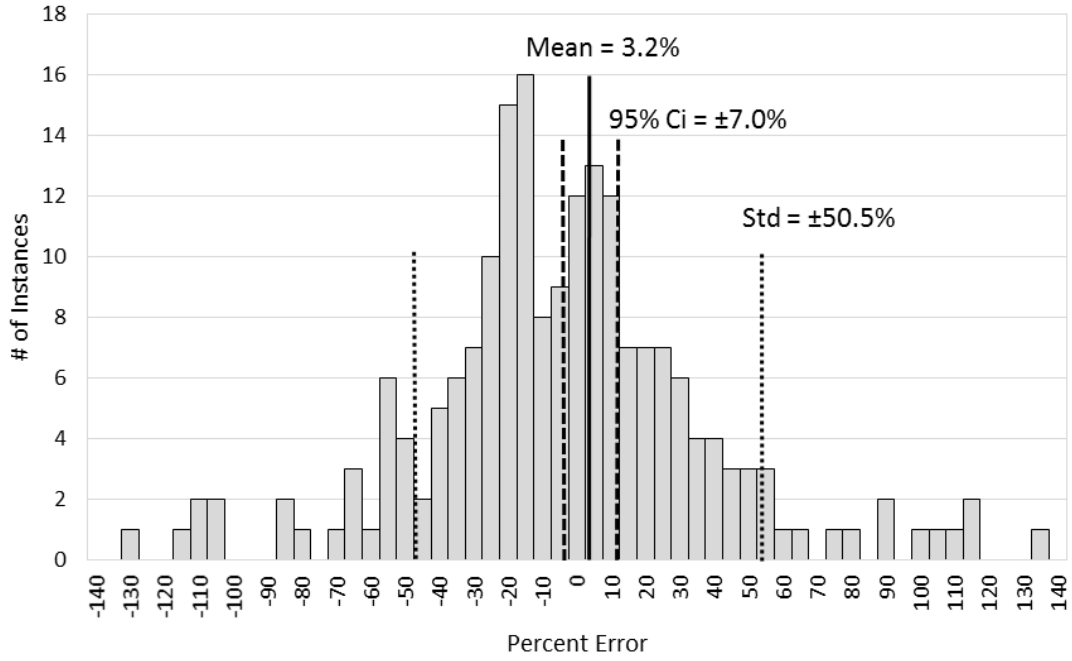

Figure 0.10: *Probability distribution for average percent error between mathematical model and flight testing of drag values.*

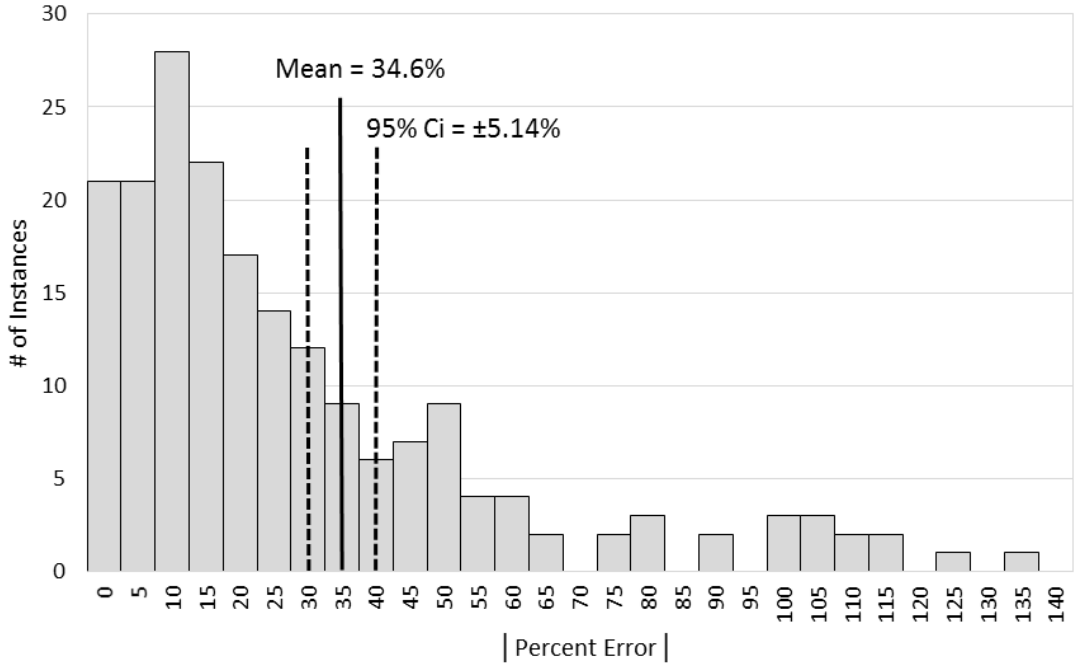

Figure 0.11: *Probability distribution for absolute average percent error between mathematical model and flight test drag values.*

5.6 Additional Performance Metrics

Several other performance metrics will now be examined for the Genii aircraft. In contrast to the previous section, these metrics will focus on time-averaged data taken over the duration of an event.

5.6.1 Takeoff

The numerical method used to predict the takeoff performance of Genii is plotted against data for the takeoff of Flight 14 in Fig. (5.12). Actual takeoff occurs at roughly 7.5 seconds as indicated by the hollow circle. The aircraft decelerates slightly during rotation due to the momentary increase in drag. The plane accelerates to climb airspeed after the 8 second interval shown.

Because the pilot does not rotate at exactly the stall speed, the minimum calculated takeoff distance, shown as a solid circle, cannot be directly compared to the actual takeoff distance. Alternatively, the calculated distance of travel and airspeed can be compared to the measured values at the actual time of takeoff. The mathematical model over predicts acceleration, and therefore the distance traveled and airspeed at any given time. At the time of takeoff, the model over predicts distance travelled by 8.0% and airspeed by 11.3%.

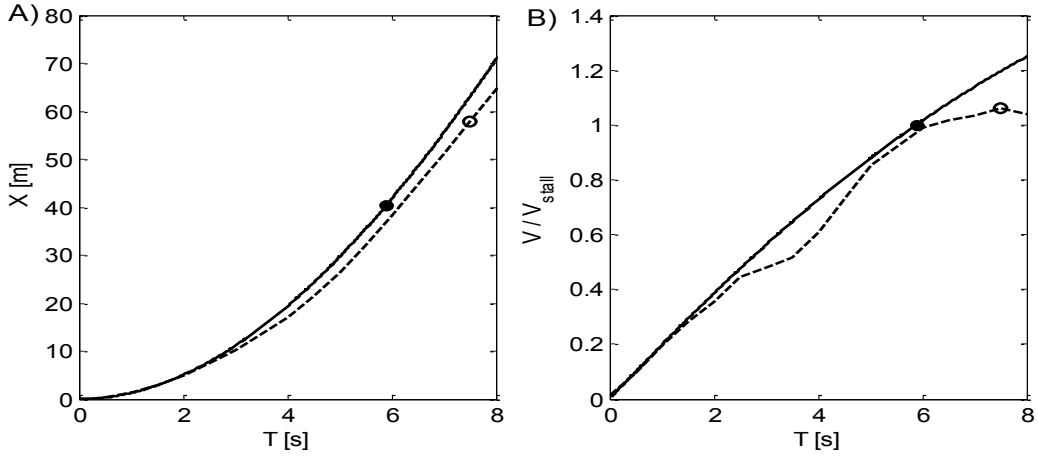

Figure 0.12: *Takeoff performance in flight 14 as A) Distance vs. Time, B) Airspeed vs. Time. Solid lines: mathematical model, Dashed lines: experimental data. Solid Point: Calculated minimum takeoff distance and airspeed. Hollow Point: Actual distance and airspeed at time of takeoff.*

5.6.2 Cruise

Of special interest to the Genii project is the low power cruise performance of the aircraft. To meet the design criteria, the Genii aircraft must be capable of sustained flight under 875 watts electrical power. This is the available power from the fuel cell after ancillary system draw. Additionally, this low power performance is required to be at a safe airspeed of 1.2 times stall, or 17 m/s for full weight flights. The factor 1.2 above stall speed was used as the minimum safe

operating airspeed for Genii. This was also used as the minimum airspeed for climb-out after takeoff and the approach airspeed for landing.

After reaching a safe altitude in flight 14, the throttle was incrementally brought back and the aircraft incrementally slowed. The interval between T = 2.16 minutes and T = 2.72 minutes confirms that Genii met the power and minimum airspeed requirements for level flight. Figure (5.13) shows plots of the aircraft's airspeed A), measured electrical power draw B) solid, propulsive power B) dashed, rate of climb C), and motor rpm D), are shown over this time interval. Throttle was held constant over the interval, however dynamic effects cause the motor speed to vary as well as the other parameters. Propulsive power is less than the electrical power into the drivetrain due to inefficiencies.

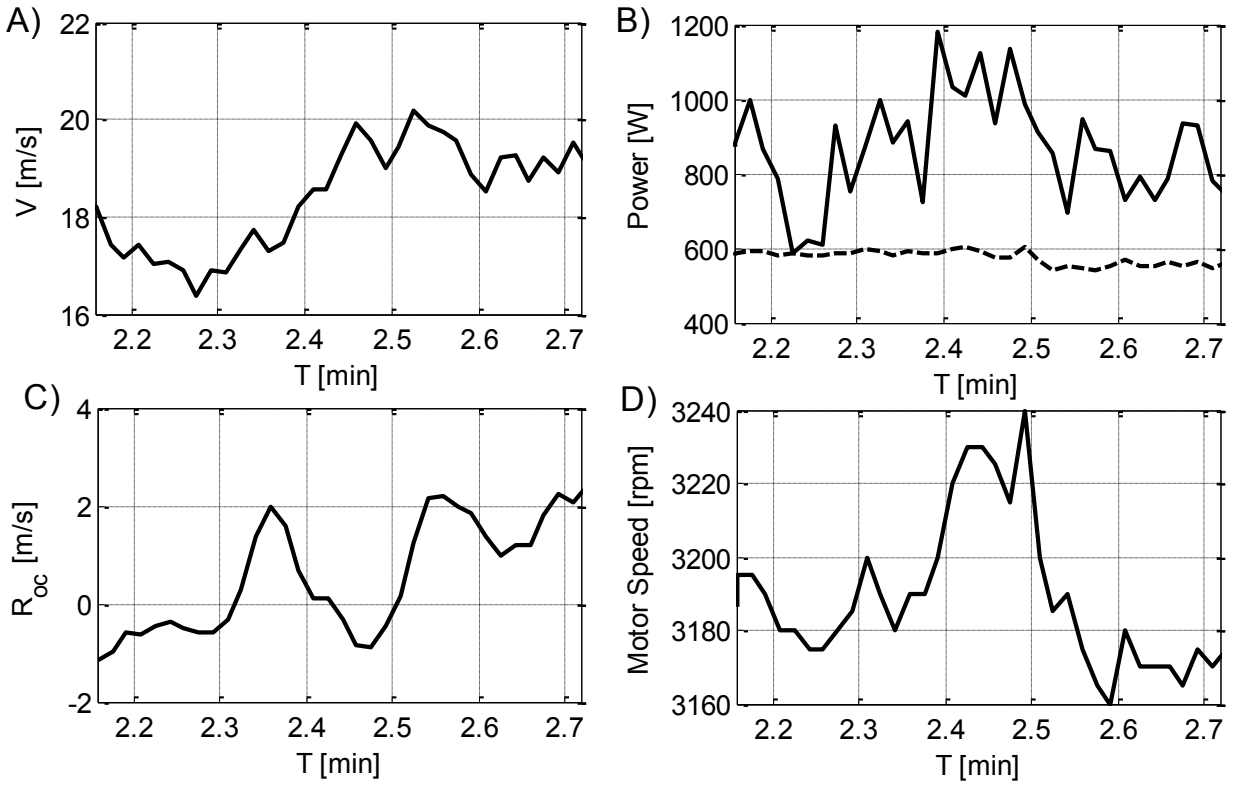

Figure 0.13 *Flight profiles over T = 2.35 to T = 2.92 of flight 14. A) Airspeed, B) Dashed: Propulsive power, Solid: Electrical power, C) Rate of climb, D) Motor Speed*

The time interval under investigation is 34 seconds in length. The average airspeed and 95% confidence interval was 18.40±0.10 m/s. The average electrical power was 871.52±13.67 watts and the average propulsive power was 574±1.74 watts. The average rpm was 3189±1.94 and the average rate of climb was 0.58±0.10 m/s. The average electrical power, airspeed, and slightly positive average rate of climb confirm that Genii meets the design requirements of level flight at less than 875 watts electrical power and greater than 17 m/s airspeed.

For these conditions including the slight positive rate of climb, the mathematical model predicts a propulsive power requirement of 583 watts, a 1.6% error from the measured value of 574 watts.

5.6.3 Turn

An investigation was ran on the mathematical model's ability to predict turn performance for the Genii Aircraft. As described in Chapter 3, a steady turn can be simulated by adding apparent weight to the aircraft proportional to the centrifugal acceleration experienced during the turn. No turns performed by Genii were steady, however an approximation of a steady turn is extracted from Flight 14 and shown as the solid line in Fig. (5.14).

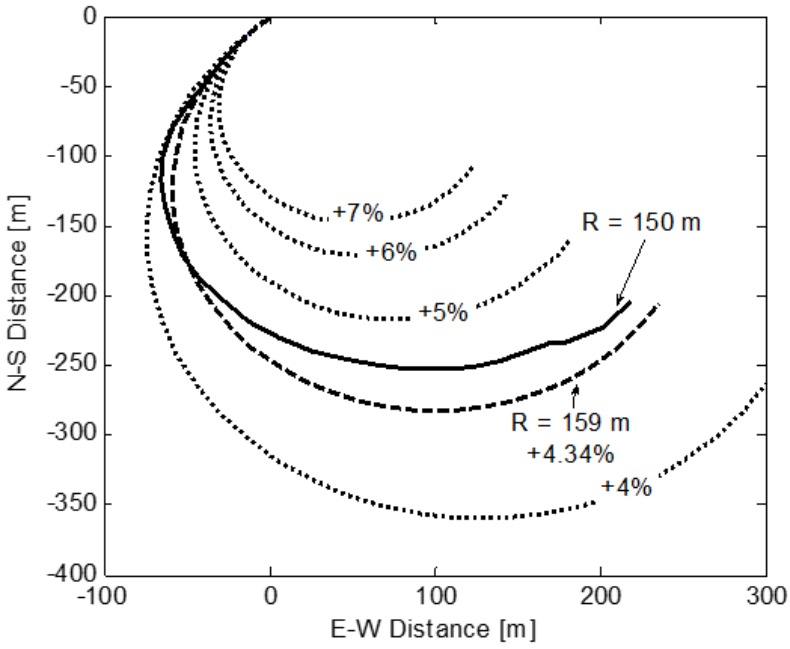

Figure 0.14: *Genii turn profiles. Solid line: Experimental profile. Dashed line: ideal turn under time-averaged values. Dotted lines: mathematical model + additional % thrust.*

The average airspeed over the turn is 19.95 m/s, the average rpm, 3416 rpm, the average turn rate, 0.126 rad/sec, the average rate of climb, 0.28, m/s and the actual radius taking the start and ending points is 150 meters. The dashed line in Fig. (5.14) depicts an ideal turn performed at the average airspeed and average turn rate over the turn interval. The radius of the time-averaged turn is 150 meters.

The mathematical model can be used in two ways: 1) Accept the average rate of climb, average velocity, and average motor rpm and calculate turn rate and radius. 2) Accept the average rate of climb, average airspeed, and turn rate or radius and calculate the required thrust. Both methods are outlined in Fig. (5.15). Average rpm is not actually calculated in method 2 and is shown in grey. Both methods analyze the same phenomenon but develop interesting results.

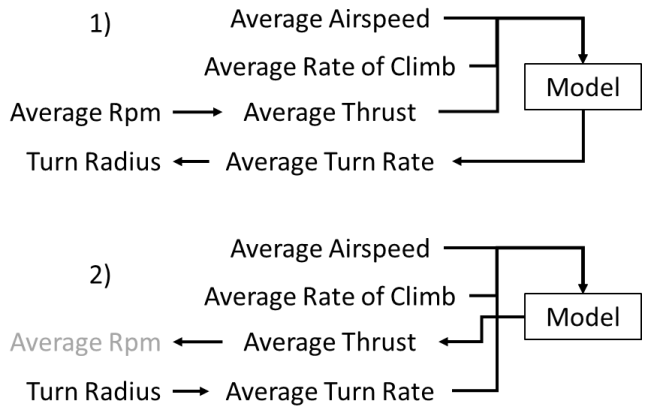

Figure 0.15: *Methods of running the mathematical model for steady turn.*

When method #1 is applied, the calculated drag exceeds the thrust by 4.34 percent, resulting in an infinite turn radius. When method #2 is applied, the calculated thrust required is 36.97 Newtons compared to 35.42 Newtons as measured by the rpm converted through the propeller model. This is an error of 4.2% compared to the infinite error for turn radius.

The mathematical model has clearly failed at determining the turn radius of the aircraft. This problem stems from the sensitivity of turn radius to the thrust of the aircraft. For example, Genii has a lift to drag ratio approximately 10 at 20 m/s. This means that for the 4.2% (1.6 N) discrepancy

in thrust, a roughly 16 Newton discrepancy in lift occurs. This problem compounds through Eq. (3.62) to produce a very large change in turn radius. If the drag as calculated by the mathematical model is reduced by 4.34% (the amount of error calculated in the thrust), the computed turn radius is 159 meters. This is a 5.6% difference from the unsteady turn radius of 150 meters.

CHAPTER 6

6.1 Summary of Approach and Findings

In this report a study was performed to document the design of a 32.8 kg UAV and calculate performance using empirical methods without reliance on CFD codes. The accuracy of these methods is assessed in the form of percent error between model and flight test data for several performance metrics including drag at various rates of climb, takeoff, and steady turns.

A description of the design of the Genii aircraft was provided including justification for most geometric sizing including wing area, taper, twist, empennage sizes, landing gear layout, and propulsion. Several low-fidelity techniques were presented that helped optimize the aircraft's design in the preliminary stage including the equations used to bound the design space for stall speed, maximum rate of climb, maximum level airspeed, and minimum takeoff distance.

To assess the viability of empirical techniques to compute the performance of similar vehicles, a mathematical model was developed from fist principles and empirical relationships previously documented in the literature. Case studies were performed for the calculation of wing profile drag where the computation technique varied between sources. In some cases, VLM was used to validate a particular approach, however the mathematical model does not utilize numerical flow solutions or CFD.

The performance of the APC 26X15E propeller used for the final Genii configuration is not documented in literature and the manufacturer's performance calculations using a NASA TAIR code were found to be unacceptably conservative. A vehicle-mounted test rig was developed to measure the thrust, power, and efficiency of the propeller as well as to validate the motor-propeller

selection. The rig's performance was validated against wind tunnel tests of a previously-documented propeller and maximum discrepancy of 12% was noted.

Computations of both vehicle drag and thrust with respect to airspeed allow the analysis of various performance metrics. Rate of climb of the Genii aircraft as well as the glide ratio were calculated with respect to airspeed and the airspeeds corresponding to their maximums were identified. Turn performance was also approximated by modifying the vehicle's weight to account for centrifugal acceleration. The maximum calculated turn rate and its corresponding airspeed were identified.

Calculations of the stall speed for the Genii aircraft at various masses corresponding to flights 10 through 14 are given. Additionally, a numerical integration technique is employed to calculate the takeoff distance of the vehicle. To assure vehicle safety, AVL was utilized to compute the static stability derivatives of the Genii aircraft and produce the eigenvalues of the dynamic motion modes for the 32.8 kg configuration at 17m/s ignoring propeller effects. Static pitch stability was compared between simplified techniques and AVL computations.

Fourteen flight tests were performed with the Genii aircraft using a combination of an Ardupilot and Rasperry Pi board for data acquisition. Flying to a specific test case (ie a given Roc and airspeed) was found to be difficult without the assistance of an autopilot. While autonomous capability is available for the Genii UAV, manual control was maintained for time and safety. As such, performance points were extracted from bulk flight data using various filtering criteria. A quadratic regression from propeller testing was used to calculate the thrust of the vehicle from rpm and airspeed logged by the aircraft.

The thrust required for various airspeeds and rates of climb can be compared between mathematical model and flight testing. This is a good assessment of the mathematical model's

ability to accurate compute vehicle drag. Flight test data ranging from normalized rates of climb (Roc / Vstall) of -0.12 through 0.20 were assessed for normalized airspeeds (V / Vstall) of 1 through 1.8 for the combined data from flight tests 10 through 14. Over these rates of climb and airspeeds, the mathematical model was observed to have an average percent error of 3.2% with a 95% confidence interval of ±7.0%. The absolute average percent error was 34.6% with a 95% confidence interval of ±5.1%.

The model's average percent error is quite low at 3.2%, but its standard deviation is large at 50.5%. Additionally, the overall accuracy may be satisfactory, however this value is skewed due to the prevalence of flight data in regimes where the mathematical model is most suited. Calculations of drag at slow speeds were found to be less accurate and slow speed decent calculations were completely unrealistic with an average percent error of -89%.

While the validation of the mathematical model focused on the thrust-drag performance of the aircraft during sparsely-steady flight conditions extracted from bulk flight data, a few specific cases of interest were examined. These included a validation that the vehicle in its 32.8 kg fuel cell configuration can sustain level flight at less than 875 W electrical power, a comparison of a characteristic takeoff with the mathematical model, and an analysis of a characteristic turn. For these metrics, a specific time domain of data was analyzed rather than an extraction of filtered data from bulk flight data. The model was found to perform well over the time-averaged flight conditions during these events.

For the specific takeoff analyzed, the mathematical model was found to over predict distance traveled by 8.0 % and airspeed by 11.3% at the actual time of takeoff. For cruise flight at fuel cell mass, the aircraft successfully demonstrated flight at 574±1.74 watts electrical power. The

mathematical model over-predicted the time-averaged propulsive power required in this flight regime by 1.6%. The mathematical model under-predicted the thrust required to perform a 150m radius to 4.2% of the measured value.

In summation the mathematical model developed from empirical techniques is found to be of good accuracy. The upper and lower 95% confidence bounds of the average percent error in the computation of vehicle drag over all rates of climb and airspeeds considered is 10.2% (over-calculation) to -3.8% (under-calculation). There is much scatter in the model's calculations, however, which results in low precision with an average absolute percent error between 39.7% and 29.5% with 95% confidence.

6.2 Applications and Importance

The work presented herein addresses a key need in the applied aerodynamics community, specifically in regards to low-speed research UAV's. The use of empirical techniques for performance calculations and design is common, not only in the development of research UAV's and demonstrators, but also in the fields of controls system development, flight planning and optimization algorithms, design optimization routines, and case studies of different fuels or vehicle configurations. The literature does not investigate the accuracy of standard empirical techniques for the calculation of vehicle performance in steady flight including level, climbing, and turning conditions.

Due to the lack of an investigation of the error associated with the empirical calculation of vehicle drag, designers of low-speed research UAVs must leave excessive margin on their design to accommodate any inaccuracies in their methods. Reporting of any calculated performance metrics is also difficult without an understanding of the error associated with these calculations.

Additionally, if the performance of a control system is being assessed, it is difficult to isolate error associated with any simplifications made to the dynamics equations from the error associated with any empirical approximations use to compute the forces acting on the vehicle.

For example, if a researcher is selecting a propulsion system for UAV to provide sufficient thrust to meet a performance requirement, if similar calculations are performed as those outlined within, the model can be assumed compute drag to within 3.2%±7.0%, where a positive percent error is an over prediction of the vehicle's drag. To maintain 95% confidence, a minimum margin of 3.8% extra thrust must therefore be designed into the system. Knowledge of this value can reduce the cost and weight of the system that might otherwise be designed with excessive capability.

This leads into a discussion of the limitations of the research presented herein and extensions to the research that would further improve the understanding of empirical model error in academia. Table (6.1) shows the applicability of the current research as well as several extension that could be made to fulfill current voids in the literature.

One limitation of the current work is that the thrust of the vehicle is computed from measured rpm and airspeed. If the vehicle itself were equipped with a load cell for in-situ measurements of thrust, this source of error could be eliminated.

In addition, the author developed the mathematical model from the work of several different references using the techniques most suited for the Genii aircraft, thus the error determined in this model is specific to this approach. Insight could be gained by examining the methods of individual authors complete with their inclusion, omission, and modifications to the model components used herein.

Finally, because the aircraft performance was measured as whole, the error contribution in the mathematical model's assessment of each individual component is unknown. While past work has been performed in wind tunnels comparing individual drag components to the total, much insight could be gained by doing so in-situ, perhaps by instrumenting individual components.

Table 0.1: *Extensions to the current work to fulfil research needs.*

		Extension of Current Work			
		Current Work	Improved Thrust	Investigation of Different Methods	Investigation of Individual Components
Current Needs in Academia	Accuracy of an empirical technique for the entire vehicle.	X	X	X	
	Development of test stand and analysis of an APC 25X15E.	X			
	Accuracy with improved data acquisition.		X		
	Assessment of complexity vs accuracy for differing methods.			X	
	Break-down of the source of error.				X

In summation, the work presented herein allows the researcher to quantify the error in the use of empirical techniques for the computation of UAV performance, an ability currently not possible with the information available in the literature. The model was fond to be sufficiently accurate to instill confidence in the author that similar techniques are sufficient for the development of low speed UAVs without the use of CFD or wind tunnel testing.

REFERENCES

Abbott, I. H., and Doenhoff, A. E., *Theory of Wing Sections*, Dover Publications, 1959.

Advanced Precision Composites Propeller Data List, Web, 05,October 2014, http://www.apcprop.com/v/downloads/PERFILES_WEB/datalist.asp

Ananda, Gavin, *APC 19X12 Thin Electric,* UIUC Propeller Database. 2014 Web. 02, March 2014. http://aerospace.illinois.edu/m-selig/props/propDB.htm

Anderson J.D. Jr, *Fundamentals of Aerodynamics*, McGraw-Hill, 2001.

Arduino Pilot Mega Multplatform Autopilot, 3D Robotics, Web. 05, October 2014, http://ardupilot.com/

Athena Vortex Lattice, 2014, Web, 05, October 2014, http://web.mit.edu/drela/Public/web/avl/

Boyer, Mark. "Global Observer Media" *Aerovironment*. Web. 16, January, 2014. *http://www.avinc.com/globalobserver/media/*

Bradley, T. H., Moffitt, B.A., Mavris, D.N., and Parekh, D.E., "Development and Experimental Characterization of a Fuel Cell Powered Aircraft," *Journal of Power Sources*, Vol. 171, 2007, pp. 793-801, 2007

Brandt, J,B and Selig, M,S. "Propeller Performance Data at Low Reynolds Numbers" 49th AIAA Aerospace Sciences Meeting. 4-7 January 2011, Orlando FL. AIAA 2011-

Brewer, D.G., *Hydrogen Aircraft Technology,* CRC Press, 1991.

Chaney, C. S., Bahrami, J., Gavin, P., Shoemake, E., Barrow, E., and Matveev, K. I., "Car-Top Test Module as a Low-Cost Alternative to Wind Tunnel Testing of UAV Propulsion Systems." *Journal of Aerospace Engineering,* 27(6), 06014005, (2014).

Chaney, C. S., Adam, P. M., Leachman, J. W., and Matveev, K. I., "Development of the Genii-UAS Demonstrator: A small-class vehicle with low wing loading for flight testing of alternative energy systems," *31st AIAA Applied Aerodynamics Conference*, 10.2514/6.2013-3045

Collage of the Desert, "Hydrogen Properties, Module 1", Department of Energy, 2001 Web 05, October, 2014 http://energy.gov/sites/prod/files/2014/03/f12/fcm01r0.pdf

Cook, D.E, Strong, P.A., Garrett, S.A, and Marshall, R.E., "A Small Unmanned Arial System (UAS) for Costal Atmospheric Research: Preliminary Results From New Zealand," *Journal of the Royal Society of New Zealand,* Vol. 43, Iss. 2, pp. 108-115, 2013

Drela, M., "Xfoil: An Analysis and Design System for Low Reynolds Number Airfoils," *Conference on Low Reynolds Number Airfoil Aerodynamics,* University of Notre Dame, June 1989.

Drela, M., and Guiles, M.B., "Viscus-Inviscid Analysis of Transonic and Low Reynolds Number Airfoils," *AIAA Journal, 25(10),* pp. 1347-1355, October 1987.

Fürrutter, M.K., and Meyer, J., "Small Fuel Cell Powering an Unmanned Aerial Vehicle," *IEEE Africon*, 2009.

Gundlach, J., *Design of Unmanned Aircraft Systems: a Comprehensive Approach*, AIAA, 2011.

Herrnstein W.H. Jr., and Biermann, D., "The Drag of Airplane Wheels, Wheel Fairings, and Landing Gears – I," *NACA Technical Report No. 485*, 1934.

Heinzen, S.B., "Development of a Passively Varying Pitch Propeller," Doctoral Dissertation, North Carolina State University, 2011.

Hoerner, S.F., *Fluid Dynamic Drag*. Hoerner Fluid Dynamics, 1965

Hoerner, S.F., *Fluid Dynamic Lift.* Hoerner Fluid Dynamics, 1992

Hunt, R.E., Hively, D.W., Daughtry, C.S.T., and McCary, G.W., "Remote Sensing of Crop Leaf Area Index Using Unmanned Airborne Vehicles," *ASPRS Pecora 17 Conference Proceeding, American Society for Photogrammetry and Remote Sensing, Bethesda, MD.* Vol. 12. 2008.

Jackson, Randy. "Phantom Eye Takes Flight" *Boeing.* 4, June 2012. Web. 16, January, 2014. *http://www.boeing.com/Features/2012/06/bds_phantomeye_first_06_04_12.html*

Jacobs, E.N., and Ward, K.E., "Interference of Wing and Fuselage from Test of 209 Combinations in the N.A.C.A. Variable-Density Tunnel," *NACA Technical Report No. 540,* 1935.

Jordan, T.L., Foster, J.V., Bailey, R.M., and Belcastro, C.M., "AirStar: A UAV Platform for Flight Dynamics and Control System Testing," *25th AIAA Aerodynamic Measurement Technology and Ground Testing Conference*. 2006.

Kim, K., Kim, T., Lee, K., and Kwon, S., "Fuel Cell System with Sodium Borohydride as Hydrogen Source for Unmanned Aerial Vehicles," *Journal of Power Sources*, Vol. 196, 2011, pp. 9069-9075.

Lindsey, W.F., "Drag of Cylinders of Simple Shapes," *NACA Technical Report No. 619*, 1937.

Lundström, D "Aircraft Design Automation and Subscale Testing - With Special Reference to Micro Air Vehicles" Doctoral Dissertation, Linköping University, Linköping Sweden, 2012.

Lundström, D., "Testing of Atmospheric Turbulence Effects on the Performance of Micro Air Vehicles," *Journal of Micro Air Vehicles,* Vol. 4, Iss. 2, pp. 133-150, June 2012.

Lyones, K.S., Stroman, R., Rodgers, J., Edwards, D., and Mackrell, J., "Liquid Hydrogen Fuel System for Small Unmanned Air Vehicles*", 51st AIAA Sciences Meeting Including the New Horizons Forum and Aerospace Exposition*, 2013-0467.

Merchant, M,P. "Propeller Performance Measurement for Low Reynolds Number Unmanned Aerial Vehicle Applications" Master's Thesis, Wichita State University, Wichita Kansas, 2004.

Millis, M. G., Tornabene, R. T., Jurns, J. M., Guynn, M. D., Tomsik, T. M., and Van Overbeke, T. J., *Hydrogen Fuel System Design Trades for High-Altitude Long-Endurance Remotely-Operated Aircraft*, NASA TM-2009-215521, 2009.

Moffet, M. A., Bradley, T. H., Parekh, D. E., and Mavris, D., "Design and Performance Validation of a Fuel Cell Unmanned Aerial Vehicle", *44th AIAA Aerospace Sciences Meeting and Exhibit, Reno, Nevada,* 10.2514/6.2006-823.

NRL Public Affairs Office. "NRL Shatters Endurance Record for Small Electric UAV" *Naval Research Lab.* 9, May, 2013. Web. 16, January, 2014. *http://www.nrl.navy.mil/media/news-releases/2013/nrl-shatters-endurance-record-for-small-electric-uav*

Ol, M. Zeune, C. and Logan, M. "Analytical-Experimental Comparison for Small Electric Unmanned Air Vehicle Propellers" 26th AIAA Applied Aerodynamics Conference. 18-21 August 2008, Honolulu HI. AIAA 2008-7345

Prandtl, L., "Applications of Modern Hydrodynamics to Aeronautics," *NACA Technical Report No. 116*, 1923.

Pricing, Terms and Conditions, Orlan W. Nicks Low Speed Wind Tunnel, Texas A&M. 2013 Web. 20,November 2013. http://wind.tamu.edu/price.htm

Raymer, D. P., *Aircraft Design, a Conceptual Approach*, AIAA, 2006.

Selig, M. S., and Gopalarathnam, A., *New Airfoils for R/C Sailplanes,* UIUC Applied Aerodynamics Group, http://www.ae.illinois.edu

Selig, M. S., Donovan, J. F., and Fraser, D.B, *Airfoils at Low Speeds,* H.A. Stokely, Virginia Beach, Virginia, 1989.

Services and Rates, University of Washington Aeronautical Laboratory. 2012 Web. 20, November 2013. http://www.uwal.org/customer/rateguide.htm

Strojnik, A., *Low Power Laminar Aircraft Design*, 1983.

Tigner, B. Meyer, M,J. Holden, M,E. Rawdon, B,K. Page, M,A. Watson, W. and Kroo, I. " Test Techniques for Small-Scale Research Aircraft" 16th AIAA Applied Aerodynamics Conference. 15-18 June 1998, Albuquerque, NM. AIAA 98-2726.

Torenbeek, E., *Synthesis of subsonic airplane design.* Delft University Press, 1976.

Unmanned Air Vehicle (UAV)," *ECS Transactions*, Vol. 26, No. 1, 2010, pp. 433-444.

Wallace, Lance. "Flying on Hydrogen: Georgia Tech Researchers Use Fuel Cells to Power Unmanned Aerial Vehicle" *Georgia Tech.* Web. 16, January, 2014. *http://gtri.gatech.edu/casestudy/flying-hydrogen*

Ward, T.A., and Jenal, B.N., "Design and Initial Flight Tests of a Hydrogen Fuel Cell Powered

Wesetenberger A. *Liquid Hydrogen Fuelled Aircraft-System Analysis*. Final technical report (publishable version), Cryoplane project; 2003

Xfoil Subsonic Airfoil Development System, 2013, Web, 05, October 2014, http://web.mit.edu/drela/Public/web/xfoil/